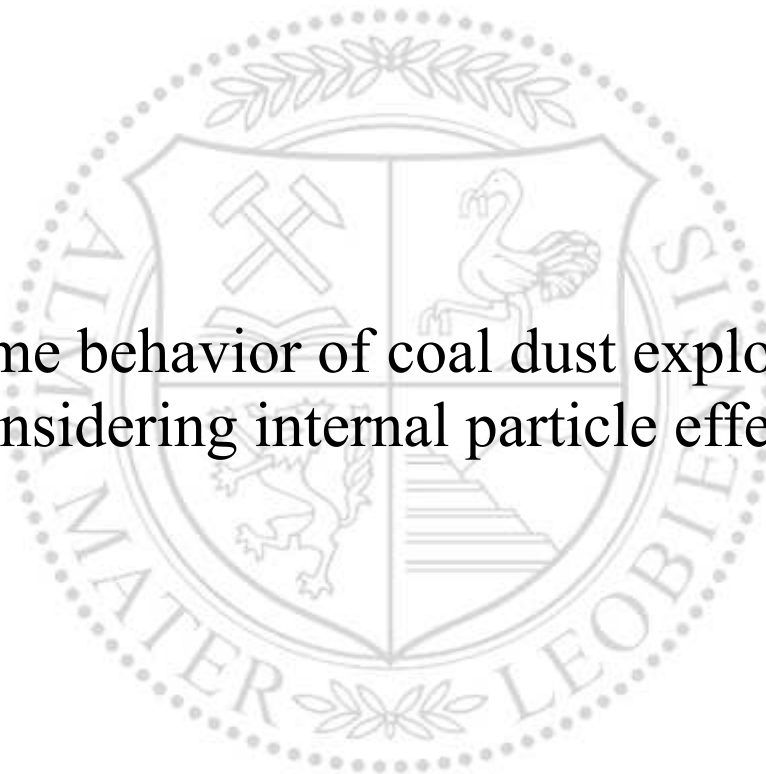Chair of Thermal Processing Technology

Doctoral Thesis

Flame behavior of coal dust explosion considering internal particle effects

Yangyue Pan

February 2023

MONTANUNIVERSITÄT LEOBEN
www.unileoben.ac.at

AFFIDAVIT

I declare on oath that I wrote this thesis independently, did not use other than the specified sources and aids, and did not otherwise use any unauthorized aids.

I declare that I have read, understood, and complied with the guidelines of the senate of the Montanuniversität Leoben for "Good Scientific Practice".

Furthermore, I declare that the electronic and printed version of the submitted thesis are identical, both, formally and with regard to content.

Date 09.02.2023

Signature Author
Yangyue Pan

Contents

Acknowledgment

Much to know and much to sow. Such challengeable life is yet to go. With pains and gains, some truth about the world is shown. Mentor, teacher, lover and friend, support as I pushing forward or falling hard. Stand here and look backward, time flies and I am here to shine.

Abstract

The dust explosion process is characterized by rapid and intricate multiphase flow, fast physical and chemical conversions, and high temperature. To advance the current understanding of the behavior of solid/air explosions, investigations of dust explosion were conducted using the MIKE 3 apparatus, coupled with Computational Fluid Dynamics (CFD) modeling. However, existing models for dust explosions in simulations are often limited and oversimplified, potentially leading to overestimations of explosion characteristics. The objective of this study is to expand current knowledge of particle behavior in solid/air explosions through the utilization of CFD modeling to analyze flame structure, burning velocity, and particle decomposition.

The impact of particle size on the dispersion and combustion processes was explored through a combination of experimental and simulation methods. The results revealed that particle size plays a crucial role in the dispersion process, with larger particles tending to accumulate at the lower position of the explosion tube. This non-uniform particle concentration distribution along the tube can significantly affect the explosion characteristics and lead to a faster flame speed compared to a uniform dust cloud distribution. Additionally, further investigations were conducted on various factors such as the pneumatic system, turbulence level, particle velocity, and particle decomposition behavior.

The explosion database was expanded through the introduction of a new devolatilization model for coal dust. This model involved the creation of a single-particle model based on sample characteristics, with the kinetics of coal pyrolysis gas derived from TGA-FTIR experiments. The single-particle model was then introduced with the porosity of the particle to investigate the influence of pore expansion during dust expansion. Results showed that the coal dust inner particle effects could be ignored up to a diameter of 250 μm.

Furthermore, a new devolatilization model based on gas evolve kinetics was implemented into OpenFOAM. The model introduced more evolved gases from coal devolatilization as well as a temperature-dependent profile. The model was tested in

a one-cell geometry and a 2D dust explosion simulation, with results demonstrating its ability to predict and differentiate the volatile gas mass fractions when particle size changes. This new model can be used to further explore the minimum ignition energy of combustible dust.

The findings of this study offer a comprehensive analysis of the dust explosion mechanism in the MIKE 3 setup and present a new model for coal devolatilization in OpenFOAM. These outcomes can aid in the design of experimental tests for research initiatives or hazard evaluations. Additionally, the CFD models provide an accessible framework to investigate and expand the fundamental understanding of organic solid dust explosions.

Kurzfassung

Der Staubexplosionsprozess ist aufgrund der Mehrphasenströmung, der schnellen physikalischen und chemischen Umwandlungen und der hohen Temperatur schnell und komplex. Aktuell verfügbare Simulationsmodelle dieses Vorgangs unterliegen Begrenzungen und Vereinfachungen, was zu einer Überschätzung der Explosionseigenschaften führen kann. Aus diesem Grund wurden im Rahmen der vorliegenden Doktorarbeit eingehende Studien zur Staubexplosion in der MIKE 3 Apparatur durchgeführt und mit Hilfe der numerischen Strömungsmechanik modelliert. Dabei wurde das derzeitige Wissen über das Partikelverhalten bei Feststoff-/Luftexplosionen erweitert, indem die Flammenstruktur, die Verbrennungsgeschwindigkeit und die Partikelzersetzung mithilfe von CFD-Modellen analysiert wurden.

Im Detail wurde der Einfluss der Partikelgröße mit genannten Ansatz aus experimentellen und simulationstechnischen Methoden untersucht. Dabei konnte festgestellt werden, dass die Partikelgröße den Dispersions- und Verbrennungsprozess beeinflusst. Bei erstgenanntem Prozess neigen die größeren Partikel dazu, sich in der unteren Position des Explosionsrohrs zu sammeln. Da die Konzentration bei sich verändernden Partikelgrößen nicht konstant ist, hat dies einen weiteren Einfluss auf die Explosionsmerkmale. Darüber hinaus führt die Konzentrationsverteilung über die Rohrhöhe zu einer schnelleren Flammengeschwindigkeit im Vergleich zu einer gleichmäßigen Staubwolkenverteilung. Im Zuge dessen wurden weitere Studien über das pneumatische System, das Turbulenzniveau, die Partikelgeschwindigkeit und das Partikelzersetzungsverhalten durchgeführt.

Ein weiteres Resultat aus den hier angestellten Forschungstätigkeiten war die Erweiterung der Explosionsdatenbank um ein neues Entgasungsmodell für Kohlenstaub. Zunächst wurde ein Einzelpartikelmodell auf Basis der Probenmerkmale erstellt. Die dafür notwendigen Kinetikdaten des Kohlepyrolysegases wurden aus eigens durchgeführten TGA/FTIR Analysen gewonnen. Zur Darstellung des Einflusses der Porenexpansion im Inneren des Partikels auf die Staubausbreitung wurde das

Einzelpartikelmodell um die Porosität des Partikels erweitert. Die Ergebnisse der Simulationen mit verschiedenen Partikelgrößen zeigen, dass die Auswirkungen des Kohlenstaubs im Inneren der Partikel bis zu einem Durchmesser von 250 μm vernachlässigt werden können.

Die gewonnenen Daten der Gasentwicklungskinetik aus der TGA/FTIR dienten zusätzlich für die Erstellung eines neuen Entgasungsmodells, welches folglich in OpenFOAM implementiert wurde. In das Modell wurden weitere bei der Kohleentgasung entstehende Gase sowie ein temperaturabhängiges Profil aufgenommen. Mit Hilfe einer einzelligen Geometrie und einer 2D-Staubexplosionssimulation konnte gezeigt werden, dass mit dem entwickelten Modell eine Vorhersage und Differenzierung der Massenanteile der flüchtigen Gase bei sich verändernden Partikelgrößen möglich ist. Das neue Modell kann zukünftig auch dazu verwendet werden, um die Mindestzündenergie von brennbarem Staub zu untersuchen.

Die Ergebnisse dieser Arbeit bieten einen detaillierten Einblick in die physikalischen Abläufe einer Kohlestaubexplosion in der MIKE 3 Apparatur. Um dies zu ermöglichen, wurde ein neues Pyrolysemodell entwickelt und in die CFD Software OpenFOAM implementiert. Dieses Modell ermöglicht zukünftig auch die Erweiterung des grundlegenden Verständnisses über das Explosionsverhalten anderer organischer Stäube, welches einen wesentlichen Beitrag in der Sicherheitsforschung beziehungsweise bei Gefahrenbewertungen liefern kann.

Nomenclature

Acronyms

$(dP/dt)_{max}$ Maximum rate of pressure rise

P_{max} Maximum explosion pressure

CFD   Computational Fluid Dynamics

CFL   Courant-Friedrichs-Lewy number

DPM   Discrete Parcel Method

DTG   Derivative Thermogravimetric analysis

E-E   Eulerian-Eulerian method

E-L   Eulerian-Lagrangian method

EDC   Eddy Dissipation Concept

FTIR   Fourier Transformed Infrared

FVM   Finite volume method

KSt   Maximum rate of pressure rise

MEC   Minimum Explosible dust Concentration

MIE   Minimum Ignition Energy

MIT   Minimum Ignition Temperature

PaSR   Partially Stirred Reactor turbulence model

PDF   Probability Density Function

PIMPLE   Pressure Implicit Method for Pressure Linked Equations

PISO Pressure Implicit with Split Operator

SEM Scanning Electron Microscopy

SIMPLE Semi-Implicit Method for Pressure Linked Equations

TGA Thermogravimetric Analysis

Greek Symbols

η_t	turbulent viscosity	Pa/s
τ	viscous stress tensor	N/m^2
ε	dissipation rate of turbulent kinetic energy	Pa/s
$\triangle t$	simulation timestep	s
β	heating rate	K/min
ϵ	molar absorption coefficient	L/(mol $\cdot$ cm)
λ_s	solid thermal conductivity	W/(m $\cdot$ K)
ν	dynamic viscosity	Pa $\cdot$ s
ϕ	coefficient of viscosity	Pa $\cdot$ s
ϕ	mass flux	kg/(m^2 $\cdot$ s)
ρ	denstiy	kg/m^3
Σ	viscous stress tensor	kg/(m^2 $\cdot$ s)
τ_{chem}	chemical reaction time scale	s
τ_{mix}	mixing time scale	s
$\triangle x$	simulation cell size	m
ξ	particle porosity, gas volume fraction	−
g	gravity vector	m/s^2
x	space dimension,position	m

Roman Symbols

α	thermal diffusivity	m^2/s
$\dot{H}$	heat exchange rate	J/s
$\dot{Q}$	energy transfer rate	J/s
$\mathbf{u}$	velocity vector	m/s
A	Arrhenius pre-exponential factor	$-$
A	absorbance	$-$
c	molar concentration	mol/m^3
C_D	drag coefficient	$-$
C_p	specific heat capacity	J/(kg $\cdot$ K)
Co	Courant number	$-$
D	characteristic length	m
D	mass diffusivity coefficient	m^2/s
d	diameter	m
E, E_a	Arrhenius activation energy	J/kg
f, F	force	N
H	diffusive heat flux, heat of reaction	W/m^2
h	heat transfer coefficient	W/m^2
h	specific enthalpy	J/kg
k	thermal conductivity	W/(m $\cdot$ K)
k	turbulent kinetic energy	J/kg
l	optical path length	cm
m	mass	kg
n	Arrhenius reaction order	$-$
p	pressure	Pa

p_t	turbulent pressure	Pa
q	conductive heat flux	W/m^2
r	reaction rate	$kg/(m^3 \cdot s)$
S_i	transport equation source term	various
T	temperature	K
t	time dimension	s
u, v, w	velocity component	m/s
V	mass concentration	kg/m^3
V	volume	m^3
X	mole fraction	$-$
Y	mass fraction	$-$

Superscripts

eff	effective
mix	mixed parameters,mixed species model
$pore$	particle pore
$pyro$	pyrolysis

Subscripts

0	initial
g	gas
i, j	specie indices
inf	boundary
p	particle
s	solid

Other Symbols

C_1, C_2 empirical coefficients for standard $k - \varepsilon$ model $-$

Nu Nusselt number $-$

Pr Prandlt number $-$

R universal gas constant $-$

Re Reynolds Number $-$

Sc Schmidt number $-$

Sh Sherwood number $-$

Chapter 1

Introduction

1.1 Background

An explosion is a chemical process that releases a significant amount of energy in a short period of time, resulting in a sudden and substantial increase in pressure. The resulting shock wave or high turbulence can cause significant harm to human beings. Additionally, secondary explosions, fires, and other disasters resulting from explosions can lead to serious casualties and economic losses. Dust explosions have been a concern since the pre-industrial era, but they became more prevalent after the industrial revolution brought about technological changes [1]. The dangers of these explosions are illustrated by a catastrophic incident that occurred on August 2nd, 2014, at Zhongrong Metal Production Company, an automotive parts factory located in Kunshan, Jiangsu, China. The explosion killed 146 workers, injured 114 others, and caused a direct economic loss of approximately 47 million Euros [2]. The destruction was so severe that the process lines were almost completely destroyed, as shown in Figure 1.1. From 1930 to 2012, the statistics of dust explosion hazards are shown in Figure 1.2, indicating an increasing trend since 1980. Therefore, the prevention of dust explosions has become an important issue for health and safety regulations in most industrialized countries.

The dangers of dust explosions have been known for hundreds of years, but they became more prevalent with the technological changes brought about by the industrial revolution between 1750 and 1850. The first documented scientific investigation of a dust explosion occurred in 1785 at a bakery in Turin where wheat flour was involved [1]. In the 18th century, research into dust explosions extended to colliery and flour dust explosions in mills [3, 4]. The mining industry was also affected by these explosions, leading to the improvement of regulations such as the Federal Coal Mine Health and Safety Act of 1969, which prioritized the safety of miners [5]. The importance of studying dust explosions is

evident from the significant increase in academic papers on this topic since the late 20th century, as shown in Figure 1.3.

Figure 1.1: Destroyed polishing production lines after an aluminum-alloy dust explosion catastrophes in Kunshan, China, 2014 [2].
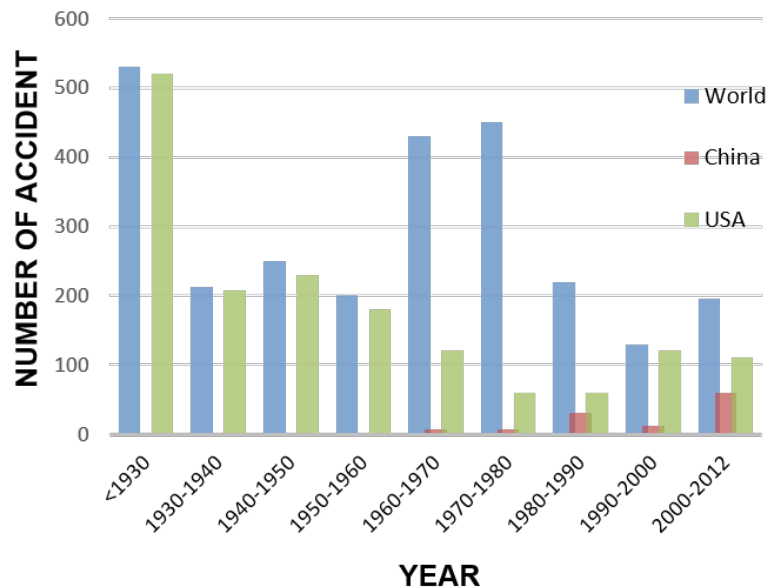
Figure 1.2: The accidents distribution along with different time periods over the world and especially in China and USA [6].

Dust explosions can occur in various locations, such as ships, elevators, processing

plants, mills, and silos [1]. For example, Figure 1.4 shows the moment when a silo filled with corn toppled over and exploded, highlighting that dust explosions can occur not only in the mining industry but also in other factory buildings with facilities that have confined spaces. During the production process, various substances such as organic solids like coal and wheat, and metallic solids such as aluminum and zinc, can produce dust that can be oxidized, leading to a dust explosion. Organic particles burn with the volatilization of the solid part, which allows the fuel vapor to diffuse toward the flame, resulting in combustion. On the other hand, metal oxidation reactions occur on the surface of particles, leading to rapid heat release due to the high reaction enthalpy. Since different particles and locations can lead to varying hazards, research on dust explosions must consider these factors to prevent and mitigate similar accidents through a thorough understanding.
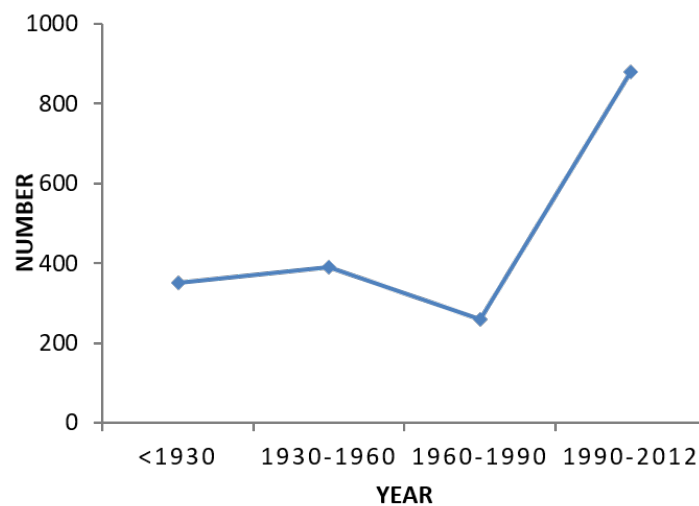
Figure 1.3: Collected number of published academic papers (journal papers in English only) relating to dust explosions in various periods [6].

In order to prevent dust explosion hazards, industries continue to conduct research on this topic as it remains a significant safety concern. Early research primarily focused on eliminating ignition sources, but Hexmer proposed the concept of inherent safety, which involves isolating mills and venting inside to prevent explosions in breweries [7]. However, with the emergence of new materials and production processes, dust explosion hazards have been found in areas previously unaffected.

To address these hazards, modern safety systems are designed with multiple layers of protection and consideration for human factors. Digital technologies are increasingly utilized to support safety management in industries [8, 9]. Understanding the quantified data of dust explosions, such as the minimum explosion concentration, minimum ignition energy, and maximum pressure rise, is crucial in designing effective safety measures.

Knowledge-based systems can aid in identifying potential problems in process plant design for various manufacturing operations, including pharmaceuticals and power production. This approach can significantly reduce the time needed to evaluate changes and ensure safety goals are met. A summary of typical dust explosibility parameters and determination standards is presented in Table 1.1.

Figure 1.4: An instant of the grain silo explosion in Indiana, USA, 2017 [10].

Studies on dust explosions have mostly focused on examining the characteristics or indices of dust explosions in a closed vessel. These results have been utilized to design explosion protection systems in the industry. The most commonly used apparatus for measuring multiple parameters in such studies are the Hartmann tube and the $20L$ SIWEK spherical vessel. The Hartmann tube is a vertical glass tube with a volume of $1.2L$, as shown in Figure 1.5a. Scientists have conducted numerous experiments to investigate how particles spread through the environment, settle, collide, agglomerate, and affect the carrier-phase. However, due to the complex behavior of dust/air mixtures, measuring and simulating local dust concentrations over time can only be done with some uncertainty. For instance, flame speed measurements in a Hartmann tube can only be reliable for powders with a high flame speed, as reported by Hosseinzadeh [11].

New technologies are becoming ever more sophisticated and less transparent, driving an increase in complexity for tests designed to evaluate them. However, the initial and boundary conditions and explosion pressure developments in industrial equipment

and processes are very complicated and different from standard laboratory tests. One solution is using large-scale experiments to evaluate the explosion severity in real industrial conditions. Another approach is modeling dust explosions using CFD. It is a useful assistant and reference for dust explosion hazard evaluation and explosion prevention design. A well-developed code can predict explosion behaviors in industrial installations if proper initial and boundary conditions are provided.

Table 1.1: Important dust explosibility parameters and their determination and application [10, 12].

Parameter	Symbol	Typical units	Description	Example test methodology
Maximum explosion pressure	P_{max}	MPa	Maximum explosion pressure in constant-volume explosion	ASTM E1226-12 [13]
Maximum pressure rise	$(dP/dt)_{max}$	bar/s	Maximum rate of pressure rise in constant-volume explosion	EN 14034-2 [14]
Maximum pressure rise rate	KSt	bar m/s	Volume-normalized (or standardized) maximum rate of pressure rise in constant-volume explosion	EN 14034-2 [14]
Minimum explosion concentration	MEC	g/m^3	Minimum explosible (or explosive) dust concentration	ASTM E1515-14 [15]
Minimum ignition energy	MIE	mJ	Minimum ignition energy of dust cloud (electric spark)	ASTM E2019-03 [16]
Minimum ignition temperature	MIT	°C	Minimum ignition temperature of dust cloud	ASTM E1491-06 [17]

Although significant efforts have been made to obtain information on the explosibility of dust, the fundamental mechanisms of flame propagation in dust suspension remain inadequately studied [18]. The field of dust explosion research still encounters fundamental challenges in explaining and evaluating basic parameters of dust explosions, such as minimum ignition energy and temperature, as well as those that define flame propagation, such as flame velocities. To enhance safety in industrial processes, new methods for experimental characterization and mathematical modeling are required.
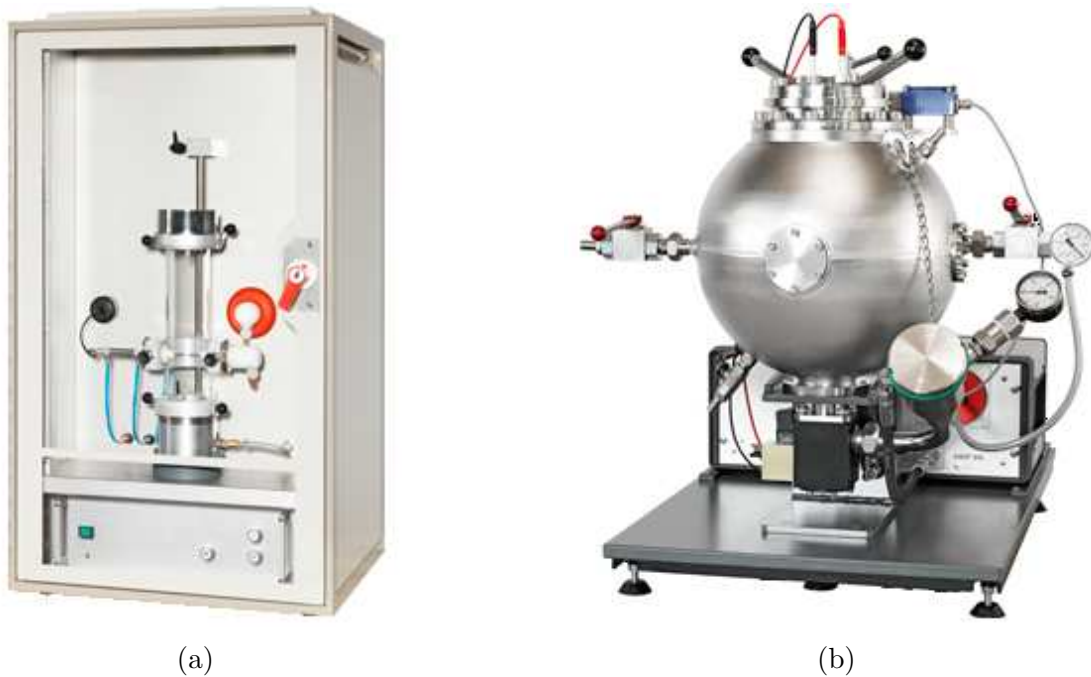
Figure 1.5: Laboratory dust explosion experimental apparatuses: (a) MIKE 3 apparatus for determining of the minimum ignition energy of dust/air-mixtures. (b) $20L$ SIWEK for determination of explosion indices of dust, gas and hybrid mixtures. [19]

1.2 Present work

The characterization of solid fuel in dust explosions still requires more experimental testing, especially when more sophisticated or smaller power is generated by new technologies in the process line. Given the ongoing need to maintain system safety, dust explosion prevention and protection remain a constant topic of discussion. Comprehensive models, such as CFD, are suggested as valuable tools to aid in research due to the difficulty and high expense of conducting experiments.

In the present study, we focused on how particle size influences dust explosion flame propagation. Specifically, we conducted experiments in the MIKE 3 apparatus to investigate the effect of particle size on each stage of the experiment, from dust dispersion before ignition to flame propagation after ignition.

The influence of different particle sizes was studied through CFD simulations, utilizing a new model developed with the open-source software OpenFOAM. This model was designed to investigate the inner heat and mass transfer of particles.

The main contributions of this work are as follows:

- The dust dispersion and explosion characteristics are studied and compared within different sizes of coal dust samples.

- The coal dust sample is characterized by TGA-FTIR tests and a new CFD model is created considering the pore expansion during pyrolysis.

- The impact of the coal size is examined with shock tests. And a new devolatilization model for coal particles is implemented into the OpenFOAM database and is verified to explore the volatile release of coal particles.

1.3 Thesis outline

The first two chapters of this thesis outline background information on flame propagation, particle size effect, and the CFD simulation models on particles. The following three chapters analyze the particle size effects on dust dispersion and explosion, the inner particle effects of different particle sizes. The final model is implemented and the results are discussed. This is followed by conclusions and recommendations from the thesis.

This thesis is structured as follows:

Chapter 1 introduce the background of dust explosion researches, the motivation of the work, the scope of the current research, and contributions of the work.

Chapter 2 presents a review of the literature on dust explosion studies, including the flame propagation, particle reactions, CFD modeling of multiphase fluid and dust explosion.

Chapter 3 analyzes particle size effect on dust dispersion characters in MIKE 3 apparatus.

Chapter 4 investigates the coal dust devolatilization characteristics by TGA-FTIR experiments. A single-particle model is built up and validated with experimental data.

Chapter 5 explores the inner particle effects in dust deflagration by using the single-particle model.

Chapter 6 builds up a new devolatilization model for dust explosion simulation in OpenFOAM and shows the dust explosion simulation results with the new model.

Chapter 7 presents the conclusion and recommendations of the further studies.

Chapter 2

State of the art

2.1 Dust explosion

2.1.1 Explosion pentagon

Explosion pentagon (Figure 2.1) states that fuel, oxidant, an ignition source, a fine mixture of the dust cloud, and confinement must be present simultaneously for fuel-air explosions to occur. Confinement is the final element making up the dust explosion pentagon. With confinement of the propagating flame front, pressure will rise, which may cause a rupture of the enclosure. The five elements are used in safety system design. By removing one element, the dust explosion is prevented. From the studies of vent systems, it is approved that the closer the vent is to the ignition source, the better pressure relief is [20, 21].
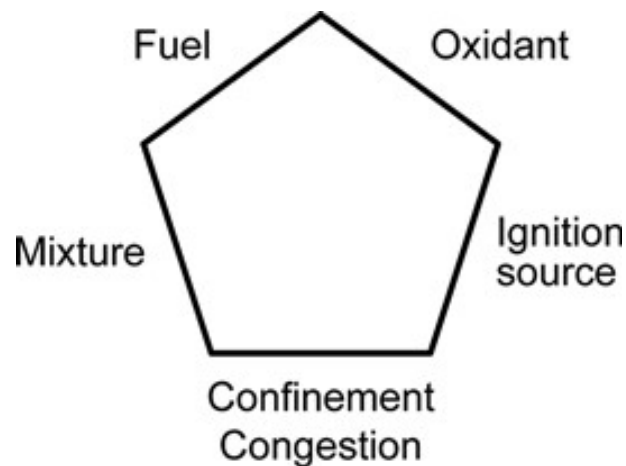
Figure 2.1: The explosion pentagon for fuel-air explosions [22].

2.1.2 Pressure-time history

Dust explosion features a rapid pressure and temperature rise due to the fast chemical reaction. The pressure development during an explosion in a closed vessel is depicted in Figure 2.2. The severity of the explosion can be characterized by two values in the picture. One is the highest gradient value during the pressure rise, $(dP/dt)_{max}$. And the other one is the highest pressure that the explosion can cause, P_{max}. Those values are not fundamental parameters for a dust explosion. They significantly depend on the characteristics of the dust sample (such as dust size, shape, and porosity) and the experimental conditions (such as vessel size and applied ignition energy).
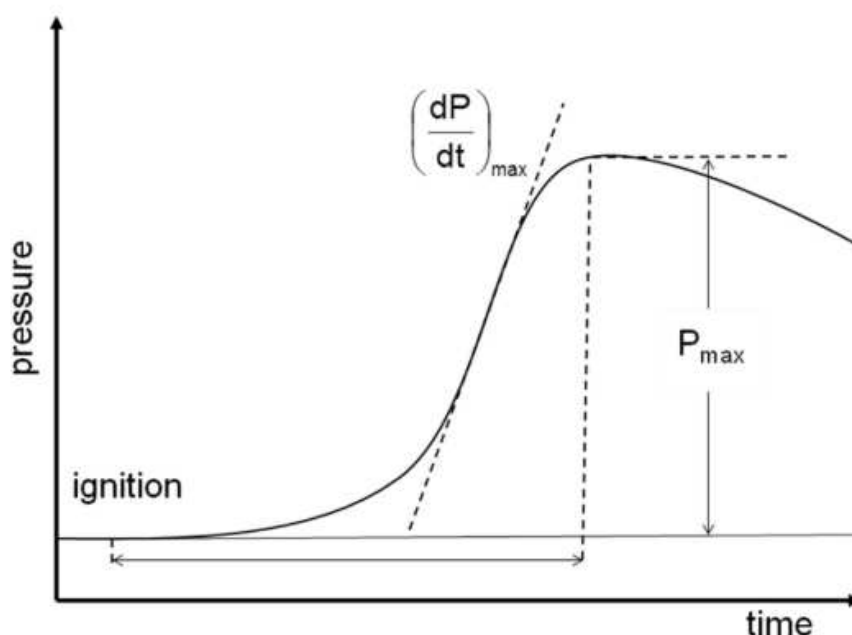
Figure 2.2: Pressure development during an explosion in a closed vessel [5].

Laboratory experimental sizes are not the same and are limited. Parameter $(dP/dt)_{max}$ and P_{max} are dependent on the volume of the explosion chamber. For scaling the size to larger volumes, the maximum rates of pressure rise are normalized by multiplying by the cube root of the explosion chamber volume, V:

$$K_{st} = (\frac{dP}{dt})_{max} \cdot V^{(1/3)}$$ (2.1)

Equation 2.1 is called cube root law. K_{st} is the dust constant or explosibility index. It describes the explosion severity of the explosion.

Various researchers have investigated the dispersion-induced flow and transient combustion phenomena in $20L$ SIWEK vessels and explored elaborate techniques for

extracting combustion parameters from pressure-time histories measured in constant volume explosion vessels [23–30]. Dahoe [24] carried out experiments with methane-air and cornstarch-air mixtures of a fixed fuel-to-air ratio at varying turbulence levels to compare the explosion pressures. The effect of turbulence on the maximum explosion pressure of dust-air mixtures was investigated by igniting turbulent cornstarch-air mixtures to deflagration at different turbulence levels in the standard $20L$ SIWEK sphere. The transient flow field in the standard $20L$ SIWEK explosion sphere was investigated by means of laser Doppler anemometry [24]. It is found that no formal cube-root-law agreement exists between the $20L$ SIWEK explosion sphere and the $1m^3$ vessel. The results of this investigation implied that the turbulence level in the $20L$ SIWEK explosion sphere at the prescribed ignition delay time was not equal to the turbulence level in the $1m^3$ vessel.

In a study by Sarli [25], a three-dimensional CFD model was employed to simulate the dispersion of dust within the $20L$ SIWEK sphere at varying nominal concentrations (with a fixed dust diameter). The results indicate that, as the nominal concentration of dust increases, sedimentation becomes dominant, resulting in a concentration of dust primarily along the walls of the vessel when ignition occurs. Simulations on the $20L$ SIWEK sphere were also carried out by Pollhammer [31]. The studies aimed to design a novel dispersion nozzle that is able to produce a homogeneous distribution of particles in the $20L$ SIWEK sphere.

Three different stages of solids dispersions can be classified according to variations in particle size distributions: fragmentation phase, stabilization of the dust cloud, and sedimentation phase [28]. The dispersion process may modify the particle size distribution from the original sample to the dispersed dust cloud [32], and the chemical igniter used in standardized tests may overdrive the explosions in the $20L$ SIWEK vessel [33].

2.1.3 Flame propagation

Dust explosions entail rapid flame propagation through clouds of combustible dust particles, or "premixed combustion with non-premixed substructures" [34]. Unlike a premixed gas flame, a mixture of dust and oxidizer involves a multiphase flow which causes difficulty in both experiments and modeling [35–39]. Horton [36] designed a burner that included a flow buffer in order to maintain a laminar coal-dust suspension. The flame produced in the burner is a standing flat flame. Atmospheric flame velocities thus could be studied, and other profiles, such as temperature, can be used to infer the relative rates of phenomena occurring in the flame front. Proust [38] proved that the classical "tube

method" is adequate for measuring laminar burning velocities of two-phase mixtures. The mixture of combustible vapors produced during the pyrolysis of particles with air cannot proceed to completion at the onset of the combustion; the oxidation in the reaction zone of the flame is not complete.

Flame propagation fuelled by dust lifting from layers represents an often-underestimated hazard in the mining and process industry. Several researchers have investigated this phenomenon, both experimentally [40, 41], and numerically [42–46]. Klemens conducted a study on the response of coal dust and silica dust to a shock wave, monitoring critical parameters such as the delay time and the gradient of dust concentration behind the shock wave [41]. The problem of dust lifting in relation to combustion and detonation, commonly referred to as a "layered explosion/detonation", has been the focus of numerous studies [47].

Previous studies have indicated that dust flames may be subject to similar instabilities as those observed in gaseous flames [48], and that the impact of radiative heat transfer can significantly affect the burning velocity of dust clouds [49]. The mechanisms of dust lifting ahead of the flame front and pressure piling in complex, confined geometries can facilitate the escalation of dust explosions. In industrial settings, combustible dust clouds typically exhibit polydisperse particle size distributions, and these distributions can significantly impact the severity of explosion events [50].

2.1.4 Chemical combustion

The chemical composition of the vapor is not necessarily the same as the overall composition of the fuel, and the flame structure can vary significantly, depending on processes such as pyrolysis, evaporation, heat, mass transfer, chemical reactions, etc., [51]. The propagation of a flame through an organic dust/air mixture typically involves three sequential processes, as illustrated in Figure 2.3: (1) heating and devolatilization of dust particles, (2) mixing of the resulting volatiles with air, and (3) combustion of the premixed volatiles in the gas phase.

As for features controlling the dust burning, vaporization is significant for fuel-limiting conditions but does not play a major role in oxygen-limiting cases [52].

As shown in Figure 2.4, the combustion behaviors of three different kinds of materials [53]. The flame of liquid droplets is smooth and continues. In the combustion, the liquid droplets evaporate into combustible gas, and then a homogeneous reaction happens on the molecular level. As for organic (stearic acid) and metallic (iron) dust clouds, the heterogeneous reactions make the flame front a discrete structure. Furthermore,

the combustion of stearic acid particles undergoes a more complicated procedure than metal particles because of their molecular structure. Two different flame propagation mechanism: kinetics-controlled regime and devolatilization-controlled regime was found out in an approach combining high-speed photography and a band-pass filter [54].
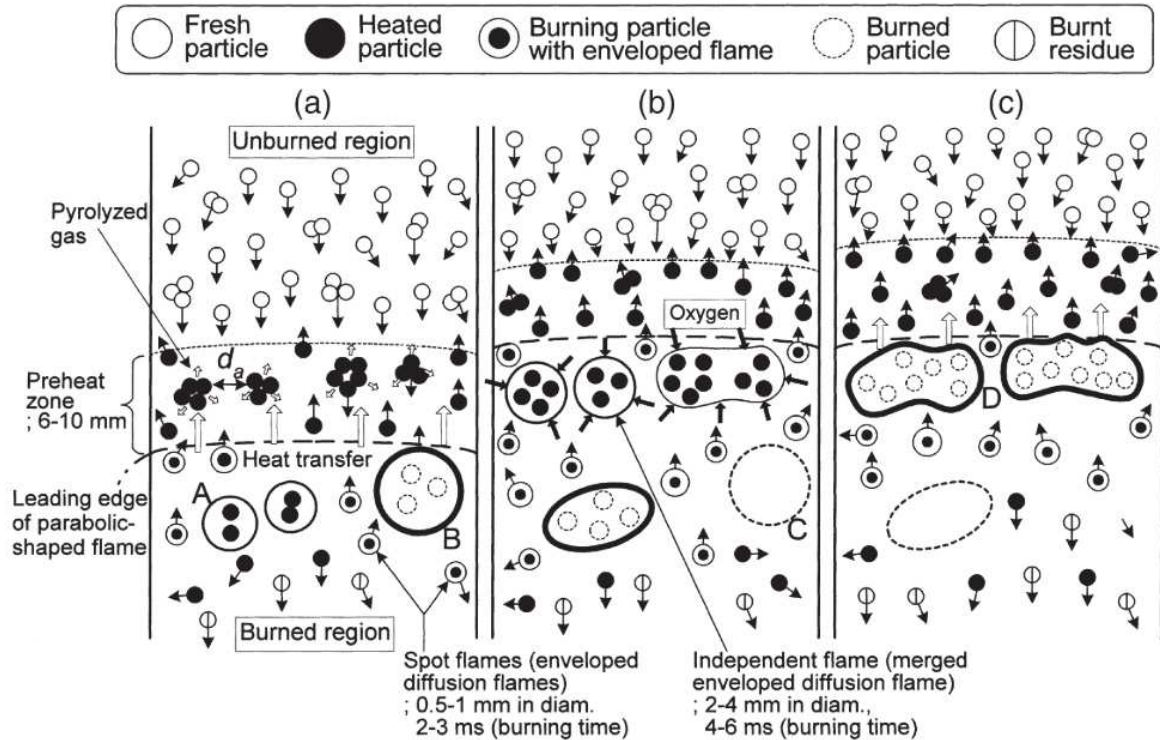
Figure 2.3: Schematic explanation of the mechanisms of flame propagation in lycopodium dust clouds. d_a = distance between the agglomerates of dust particles [53].

Flammability and explosion parameters for combustible dusts are typically provided in material safety sheets and databases based on measurements taken at a pressure of 1 atm. However, many systems handling flammable dust operate at pressures that differ from this standard [55]. Although limited data is available on this topic, research has shown that the minimum explosive concentration (MEC) of dust clouds tends to increase with pressure [56–58]. Studies by these authors, which measured MEC values for coal and polyethylene dust clouds at varying pressures within the range of 0.4-2.5 atm, suggest that the observed linear increase in MEC with pressure can be attributed to a decrease in the production of volatiles and a reduction in mixing efficiency between volatiles and air inside the combustion vessel. More recently, Pilao measured the MEC values of cork/air mixtures in the pressure range of 0.9-2.2 atm, and also found a linear increase in MEC values [57]. They attributed this trend to the decrease in O_2 content that occurs with increasing initial pressure.

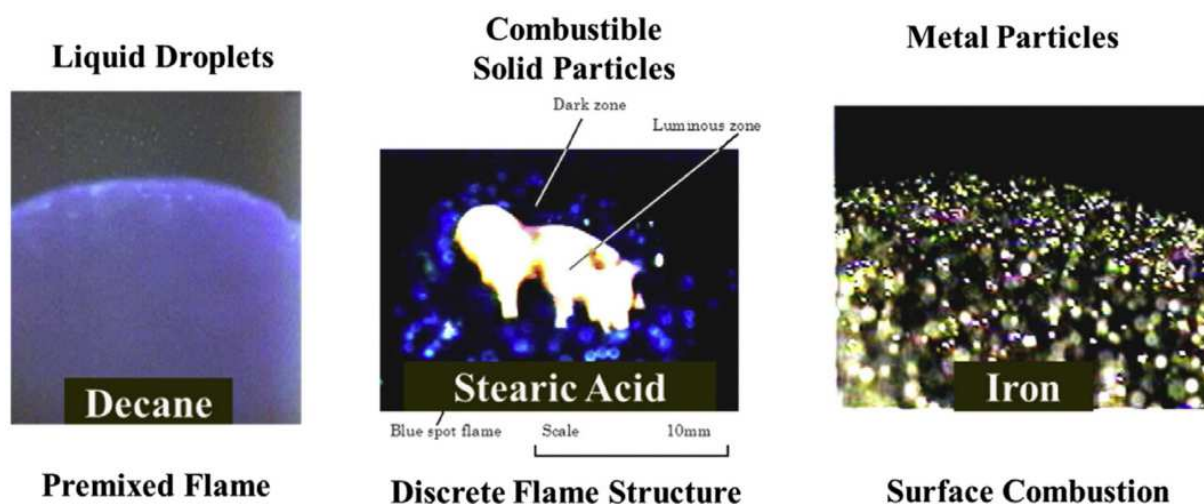Figure 2.4: Combustion behaviors of different materials [54].

Samples, the phenomenon of dust explosion in lab size, and particle chemical combustion properties are the most studied aspects of dust explosion research. To conduct experiments in lab size, dust samples, ignition source, dispersion geometry, and measure system should be considered. The most common combustible dust like coal, lycopodium, and corn starch existing in process lines are analyzed widely with lab equipment. Values of standard parameters like MEC and MIE can be found in the literature. Taking the agglomeration of dust into consideration, mixing samples with different sizes or chemical compositions were tested. Based on standard lab equipment, scientists modified their research apparatus according to their interests. With the advance of technology, better observation of the particle combustion and flame characters can be achieved. At the same time, new materials should also be taken into consideration in future studies. Those research, as a result, can provide references for mathematical models. Then the simulation of dust explosion can be possible, and visualized results are a vital tool for explaining the phenomenon that researchers cannot observe in experiments.

2.1.5 Effect of particle size

The description of the behavior of dust/air mixtures in turbulent flow is very complex. This implies that the flow is inherently turbulent for most systems encountered in practice. Results from both laboratory- and large-scale experiments suggested that the dispersibility of the dust has a significant influence on the explosion hazard [59, 60]. Therefore, knowledge about the actual dust concentration in silos or other process vessels during filling is important for risk assessments [61, 62]. They tried to create homogeneous and

reproducible dust clouds in the experiments to control dispersion effects. Klippel [61] did repeat measurements of dust concentration in two different filling methods (pneumatic filling and injection via nozzles with pressurized air) in a $50m^3$ vessel. Results showed that even for injection with eight nozzles, which should lead to a more or less homogeneous dust/air mixture, the deviation can be more than 30% compared to the average of the tests.

Equations are brought up to predict gas-particle flows, such as the discrete parcel method (DPM), two-fluid model, and probability density function (PDF) models. Dust dispersion depends very much on the actual conditions of each test, such as air humidity and every dust sample. Collecting dust samples from an industrial facility is an integral part of the overall risk assessment. Therefore, it is essential to test samples that are representative of the actual explosion hazard in the specific facility.

Furthermore, statistical records indicate that dust explosions are less likely to occur for normal operating conditions, compared to shut-down or start-up of production, after long periods of warm and dry weather, etc., [35]. To ensure accuracy in testing, it is advisable to incorporate a level of caution when preparing samples. When testing the actual powder produced, it may be necessary to take samples while the dust is in motion rather than from heaps or bulk. To cover the entire stream of powder in short intervals rather than a part of the stream for longer periods can be more relevant [63]. Before conducting explosion testing, it is recommended to follow best practices by sieving and drying the samples.

The characteristic size of the fuel particles is usually in the range of $1 - 100\mu m$ [64]. The high reactivity and specific surface area of nano-metallic particles makes them highly susceptible to combustion, resulting in lower ignition temperatures, fast-burning rates, and shorter burning times when compared to micro- or larger-sized particles and particle clusters. For example, for micron- and larger-sized aluminum particles, such a temperature usually corresponds to the melting point of aluminum oxide (i.e., $2350K$). For nano-sized aluminum bulk, the melting point can be as low as $930K$ [37], and even lower when considering a single particle of $1nm$ according to a study based on molecular dynamics [65]. In the experiments of dust explosion, different flame micro-structures of two kinds of particles were also observed. The luminous intensity of micro-particle flame was much brighter than that of microparticles because more oxidization reactions occurred on the surface of larger particles. On the other hand, the flame front propagation velocity for nanoparticles was much higher because of the larger upward thermophoresis force [66].

The sensitivity and severity of dust explosions are related to the particle size of the dust. The total area in contact with the oxidizer increased due to the particle size

decrease. Figure 2.5 shows the curve of the maximum rate of pressure rise when organic and metallic particle size change. When the size decreases, the severity of the explosion increase. Nanoparticles have smaller MEC, MIE, and remarkably higher explosion severity [67, 68]. Thus, in general, the smaller the particle size is, the stronger the flammability, the chemical activity, and the explosive sensitivity and severity are [69]. The flammability and chemical activity of dust are related to the particle size because the increase in particle size leads to a decrease in the specific surface area of the particles [70].

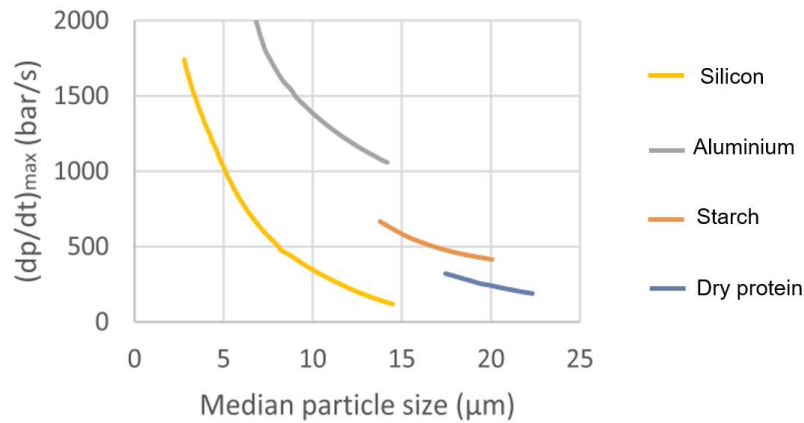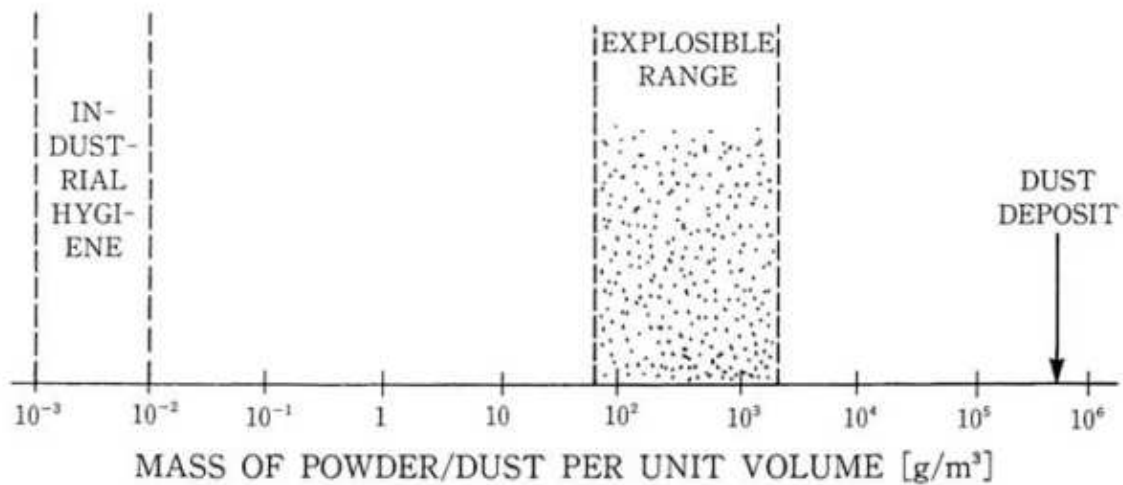Figure 2.5: Influence of particle size on maximum rate of pressure rise [35].

Figure 2.6: Range of explosive dust concentrations [35].

The fine fraction of the particle size distribution represents the primary hazard, and various processes may lead to the accumulation and drying of fine dust in certain areas [71]. Most dust samples have a broad particle size distribution, and particles of

15

different sizes react differently to variations in the flow field. Furthermore, the dynamics of the turbulent structures create local concentration gradients. According to Eckhoff [72], the most important properties of dust dispersion are: the particle shape; the particle size distribution; the degree of agglomeration; the dust concentration within the cloud; the degree of turbulence of the suspension. For example, Figure 2.6 shows the range of explosive dust concentrations in air at room temperature and pressure for natural organic dust, e.g., maize starch, compared with the typical range of maximum permissible dust concentrations that are relevant in the context of industrial hygiene, and with a typical density of deposits/layers of natural organic dust [35]. The concentration of dust is highly connected with dust explosions.
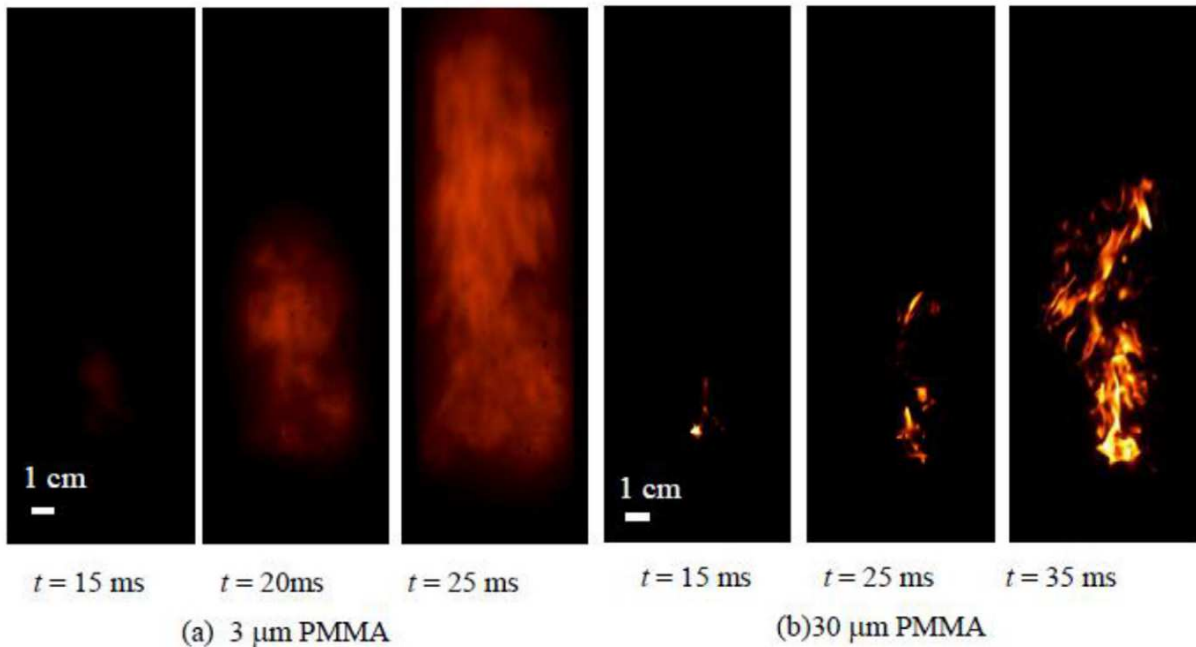

Figure 2.7: Flame structures of monodispersed particles [73].

In the research of polymethyl methacrylate (PMMA) dust explosion [73], the flame structure of $3\mu m$ and $30\mu m$ particles were compared (Figure 2.7). The flame of smaller particles has a smooth and faster flame speed due to less time consumption in the heating and devolatilization period. The flame of $30\mu m$ particles shows a brighter and disconnected flame structure. The assumed model to illustrate the flame structure is in Figure 2.8. The flame front of smaller particles is much smoother than larger particles because burnable volatiles form immediately after heating. In contrast, the larger particles need more time to vaporize, resulting in a thicker preheating zone and slower propagating speed. The unburned particles behind the flame front exhibited a strong luminous part. In the study of Zhang [74], he confirmed that the larger particles have a thicker preheating

16

zone for corn starch. He used the iron current peak and temperature curve of the flame to locate the preheating zones of $30\mu m$, $45\mu m$, and $65\mu m$ samples. The flame of smaller particles tends to show homogeneous combustion because of the higher pyrolysis rate.

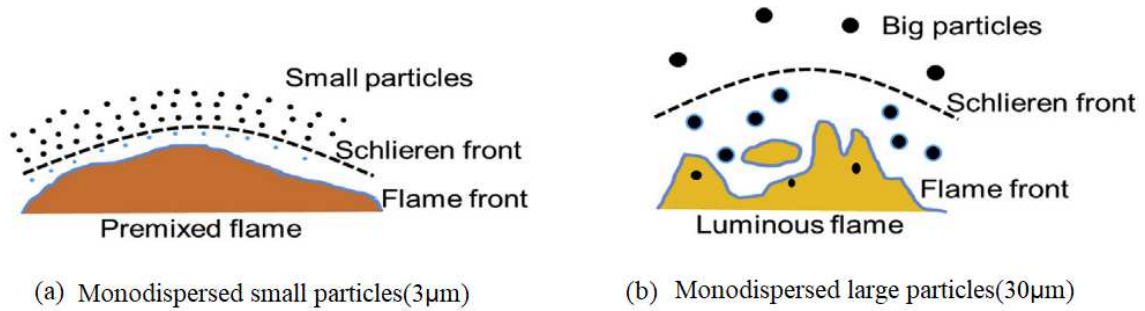(a) Monodispersed small particles(3μm)   (b) Monodispersed large particles(30μm)

Figure 2.8: Assumed flame structures with different particle sizes [73].

2.2 Research state of CFD on dust explosion

2.2.1 OpenFOAM

OpenFOAM, short for Open-source Field Operation And Manipulation, is a free and open-source database used for calculating a wide range of variables of interest, from complex fluid flows with chemical reactions, turbulence, and heat transfer to acoustics, solid mechanics, and electromagnetics [75]. In solving fluid flows, the finite volume method (FVM) is commonly used in OpenFOAM. This approach divides the calculation domain into a specified number of fixed-volume cells, or control volumes, and applies the conservation equations between each control volume to solve the partial differential equations. Temporal discretization is applied first to compute the partial differential equations, followed by spatial discretization which uses various interpolation schemes to calculate the face value from the cell value. For example, cell values include temperature and density, while face values include velocity and flux.

2.2.2 Governing equations and models

CFD uses the numerical method to calculate the governing equations of a fluid field. Any fluid flow is related to flow and heat transfer. They are governed by a set of partial differential equations. In the computation, those equations are treated specially to obtain discrete solutions. The difference of two flows may come from their initial and boundary conditions. The governing equations follow three fundamental physical laws: the conservation of mass, momentum, and energy. Considering a flow with heat transfer in a 3D Cartesian coordinate system, the velocity vector is $\mathbf{u}$ and the components on three coordinates are u, v, w. The governing equations of a 3D transient compressible flow are the Navier-Stokes equations, which describe the conservation of mass, momentum, and energy in a fluid. In the compressible form, the Navier-Stokes equations are expressed as [76]: .

Conservation of mass (also called continuity equation):

$$\frac{\partial \rho}{\partial t} + \nabla \cdot (\rho \mathbf{u}) = 0 \tag{2.2}$$

Conservation of momentum:

$$\frac{\partial}{\partial t}(\rho \mathbf{u}) + \nabla \cdot (\rho \mathbf{u} \mathbf{u}) = -\nabla p + \nabla \cdot \boldsymbol{\tau} \tag{2.3}$$

Conservation of energy:

18

$$\frac{\partial}{\partial t}(\rho E) + \nabla \cdot (\rho E \mathbf{u}) = -\nabla \cdot \mathbf{q} + \nabla \cdot (\boldsymbol{\tau} \cdot \mathbf{u}) + S_E \qquad (2.4)$$

where ρ is the density, $\mathbf{u}$ is the velocity vector, p is the pressure, $\boldsymbol{\tau}$ is the stress tensor, E is the total energy per unit volume, $\mathbf{q}$ is the heat flux, and S_E is the energy source term.

Turbulent modelling

Turbulence is a highly complex, 3D, unsteady, and vortex flow. It consists of varying sizes of vortexes. The bigger vortex is generated by boundary effects and velocity gradient. Their energy is transferred to smaller vortices when they interact. Smaller vortices vanish in the end because of the viscosity of the fluid.

The numerical simulation methods of turbulence include DNS (Direct Numerical Simulation), LES (Large Eddy Simulation), and Reynolds-averaging-equation. DNS directly calculates the 3D unsteady Navier-Stokes equation, which consumes a lot of time and computer capacity. The LES method considers the vertices in turbulence into different scales. The Kolmogorov scale is a key parameter in LES that is used to model the subgrid-scale eddies and set the grid resolution [77]. The bigger scale vertices are calculated using the Navier-Stokes equation. While the small-scale vertices are not calculated. The effect of small-scale vortices on bigger-scale vortices, called sub-grid Reynolds stress, is considered using approximate models.

Reynolds-averaging-equation consists of two methods: the Reynolds stress model and the turbulent viscosity model. In the Reynolds stress equation method, more partial differential equations are added to the time-averaged turbulent terms to close the equation. The widely used method currently for numerical calculation is the second method, the turbulent viscosity model, such as $k - \varepsilon$ and $k - \omega$ model simplified by Boussinesq assumption.

The Reynolds-averaged equation includes the continuity and momentum equations in the Cartesian coordinate system. They can be described by the sum of time-averaged value and turbulent value. The equations are then derived as follows [76].

Continuity equation:

$$\nabla \cdot \boldsymbol{u} = 0 \qquad (2.5)$$

$$\overline{u_i} = u_i' + U_i \qquad (2.6)$$

Momentum equation:

$$\frac{\partial(\rho \overline{u_i})}{\partial t} + \frac{\partial(\rho \overline{u_i u_j})}{\partial x_j} = -\frac{\partial \overline{p}}{\partial x_i} + \frac{\partial(\eta \frac{\partial \overline{u_i}}{\partial x_j} - \rho \overline{u_i' u_j'})}{\partial x_j} \tag{2.7}$$

As for other parameter (ϕ) in the flow, they can be derived similarly.

$$\frac{\partial(\rho \overline{\phi})}{\partial t} + \frac{\partial(\rho \overline{u_j} \overline{\phi})}{\partial x_j} = \frac{\partial(\Gamma \frac{\partial \overline{\phi}}{\partial x_j} - \rho \overline{u_j' \phi'})}{\partial x_j} + S \tag{2.8}$$

Equation 2.5-2.6 proof that the time-averaged value of turbulent velocity fulfills the continuity equation, where $\boldsymbol{u}$ is the velocity vector, u_i' is the fluctuating velocity component, U_i is the mean velocity component, and the overline denotes a time average. The time average is typically taken over a long enough period of time so that the effects of the turbulent fluctuations are averaged out, leaving only the mean flow properties. Equation 2.7 is the time-averaged Navier-Stokes equation, i.e., Reynolds equation. $\rho \overline{u_i' u_j'}$ is called Reynolds stress or turbulent stress.

According to the Boussinesq approximation, the additional stress generated by a turbulent pulse can be related to a strain rate similar to laminar flow stress. Write the Reynolds stress according to the structure of the laminar constitution equation:

$$-\rho \overline{u_i' u_j'} = (\tau_{i,j})_t = -p_t \delta_{i,j} + \eta_t \left(\frac{\partial u_i}{\partial x_j} + \frac{\partial u_j}{\partial x_i}\right) - \frac{2}{3} \eta_t \delta_{i,j} div V \tag{2.9}$$

η_t is turbulent viscosity, which is decided by flow condition but not physical parameter. $\delta_{i,j}$ is shear thickness. p_t is turbulent pressure. It is defined as,

$$p_t = \frac{1}{3} \rho(\overline{u'^2} + \overline{v'^2} + \overline{w'^2}) = \frac{2}{3} \rho k \tag{2.10}$$

where k is turbulent kinetic energy per unit mass:

$$k = \frac{1}{2}(\overline{u'^2} + \overline{v'^2} + \overline{w'^2}) \tag{2.11}$$

In the turbulent viscosity model, the Reynolds stress is a function of turbulent viscosity. To define turbulent viscosity η_t is the key of this method. Turbulent models express relations between η_t and time-averaged turbulent parameters. There are three types of turbulent models: *zero-equation model, one-equation model* and *two-equation model.*

The turbulent model used in this study is the $k - \varepsilon$ model. It is a two-equation turbulent model which calculates the turbulent length l using the ε equation [78].

ε is the dissipation rate of turbulent kinetic energy per unit.

$$\varepsilon = \nu \overline{(\frac{\partial u_i'}{\partial x_k})(\frac{\partial u_i'}{\partial x_k})} \tag{2.12}$$

where the ν is molecular viscosity.

The turbulent kinetic energy equation is (k-equation):

$$\rho \frac{\partial k}{\partial t} + \rho u_j \frac{\partial k}{\partial x_j} = \frac{\partial[(\eta + \frac{\eta_t}{\sigma_k})\frac{\partial k}{\partial x_j}]}{\partial x_j} + \eta_t \frac{\partial u_i}{\partial x_j}(\frac{\partial u_j}{\partial x_i} + \frac{\partial u_i}{\partial x_j}) - \rho \varepsilon \tag{2.13}$$

The dissipation equation is (ε-equation)

$$\rho \frac{\partial \varepsilon}{\partial t} + \rho u_k \frac{\partial \varepsilon}{\partial x_k} = \frac{\partial[(\eta + \frac{\eta_t}{\sigma_\varepsilon})\frac{\partial \varepsilon}{\partial x_k}]}{\partial x_k} + \frac{c_1 \varepsilon}{k} \eta_t \frac{\partial u_i}{\partial x_j}(\frac{\partial u_i}{\partial x_j} + \frac{\partial u_j}{\partial x_i}) - c_2 \rho \frac{\varepsilon^2}{k} \tag{2.14}$$

Lagrangian and Eulerian approaches

Eulerian-Eulerian (E-E) and Eulerian-Lagrangian (E-L) are two approaches used in computational fluid dynamics to model fluid-particle flows. The E-E model considers both the fluid and particle phases as separate continua, with each phase being treated as a fluid. The particles are grouped based on their size, and each group is considered a separate fluid species. The E-E model can be computationally expensive as the number of particle size groups increases, and it may also suffer from an excess of diffusion in the particle phase.

The Eulerian-Lagrangian (E-L) model is a versatile approach that can handle problems involving a wide range of particle size distributions. The E-L model characterizes the particle phase using a Lagrangian framework, whereby the trajectories, compositions, and combustion of particles within the calculation domain are traced using Lagrangian coordinates. The governing equations of the particle phase consist of ordinary differential equations, describing the position, mass, composition, velocity, and temperature of the particles.

Given the potentially vast number of particles involved in the simulation, the E-L model often employs a technique where several million particles are represented by a single computational particle, also known as a model particle or parcel [79]. By grouping multiple particles in this manner, the computational cost of the simulation can be significantly reduced. However, it is important to note that such a simplification can also result in a loss of accuracy, especially when it comes to capturing the fine-scale dynamics of individual particles. As such, careful consideration must be given to the appropriate level of detail required for a given application.

2.2.3 Single-particle models

There are models to describe the explosion stages of single particles. Figure 2.9 shows the model of one polymethyl methacrylate (PMMA) particle. Zhang [74] considered the combustion into two steps: pyrolysis/devolatilization and combustion. Firstly, the particle is heated to the liquid phase due to the heat flux between the two phases and radiation from the combustion area. The internal heat conduction also accelerates the melting of the solid phase. When the temperature reaches the ignition temperature, the volatile/air mixture is ignited, and the flame is generated. In his research, the effect of particle size distribution was also studied. By comparing the characteristic times of two steps of four diameters ($100nm$, $5\mu m$, and $30\mu m$) dust mixtures that have the same Sauter mean diameter, they found out that a higher fraction of $5\mu m$ PMMA dust particles made the pyrolysis/devolatilization and combustion processed faster.
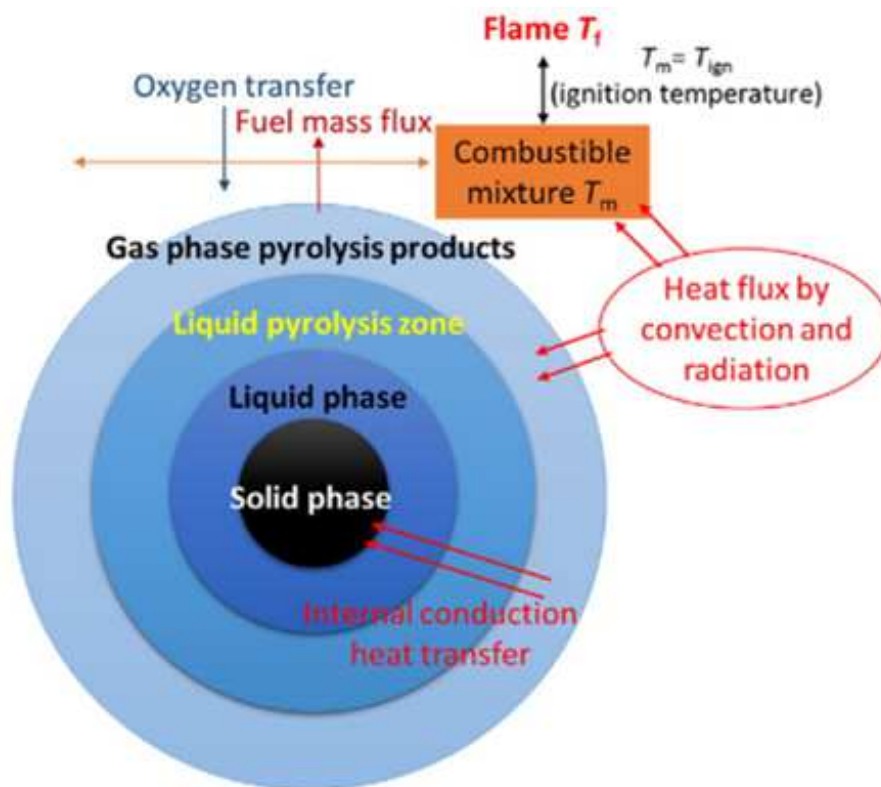

Figure 2.9: Pyrolysis/devolatilization and combustion model of single PMMA dust particle [74].

The composition of particles is basically moisture, volatile matter, fixed carbon, and ash. The stages of coal combustion are divided into four stages:

1. Preheat and dry.

In this stage, the coal is heated and the water is vaporized. Coal particles absorb heat.

2. Devolatilization and volatile release.

   The hydrocarbon components in coal are pyrolysed after absorption of heat. The volatile is a mixed combustible gas which burns at the moment of release.

3. Combustion.

   It consists of the combustion of volatile and char. The heat release from volatile combustion provide the temperature condition for char. And the reaction of char needs a large amount of oxygen to release heat and then results in rapid temperature increase. This will in return ensure the combustion reaction of the fuel.

4. Burn out stage

   Char becomes ash after it is burnt out. While, the rest of char is hard to contact with air when it is surrounded by ash and smoke. As a result, the burn out stage is very slow.

The general model to describe heat transfer inside coal particle and transient diffusive chemically reacting flow around the particle are a set of conservation equations together with initial and boundary conditions [80].

$$\frac{\partial \phi_i \varphi_i}{\partial t} + \frac{1}{r^f} \frac{\partial (r^f \Psi_i u \varphi_i)}{\partial r} = \frac{1}{r^f} \frac{\partial (r^f \Gamma_i \frac{\partial \varphi_i}{\partial r})}{\partial r} + S_i \tag{2.15}$$

where, i varies from 1 to 6 and represents conservation equations of different parameter.$i = 1, 2$ are the conservation of total mass and energy inside the particle (solid phase). $i = 3, 4, 5, 6$ are corresponding to the total mass, species, energy, and momentum conservation equation for the gas phase around the particles. The other terms are chosen according to the equation and can be found in literature [80].

Suitable boundary conditions and initial conditions should be decided for solving the equations. Spijker [81] considered the porous structure of lycopodium particles in the single-particle model. The pore diameter changes when evaporation and pyrolysis happen on the particles. The diameter of unburned particle pore (d_{pore}^0) is estimated by microscopy and the burnt particle pore diameter (d_{pore}) is calculated by Equation 2.16 by assuming pores are round and do not change in length.

$$(d_{pore})^2 = (d_{pore}^0)^2 \frac{\xi}{\xi^0} \tag{2.16}$$

where ξ, ξ^0 are the gas volume fraction of the burnt and unburned particles respectively. When considering the porous structure, the flow inside of the particles will generate drag force. He applied the Kozeny-Carman equation which calculates the pressure drop of a fluid flowing through a packed bed of solids in the gas phase equation [82].

$$\frac{\partial p}{\partial r} = -\mu_{mix} u_r \frac{(1 - \xi_{eff})}{\overrightarrow{F} \xi_{eff} d_{pore}^2} \tag{2.17}$$

the momentum equation of the flow is:

$$\frac{\partial \xi \rho \overrightarrow{u}}{\partial t} + div(\xi \rho \overrightarrow{u} \overrightarrow{u}) + \mu_{mix} \frac{(1 - \xi)^2}{\overrightarrow{F} \xi^2 d_{pore}^2} \overrightarrow{u} = -\xi grad(p) \tag{2.18}$$

2.2.4 Studies in dust explosion using OpenFOAM

The already existing and open-source code makes OpenFOAM a very useful and flexible tool for studying dust explosions. The results seem very promising when simulating the particle dispersion and deflagration and the extinguishing of flames. The following work with newly implemented models should carry on.
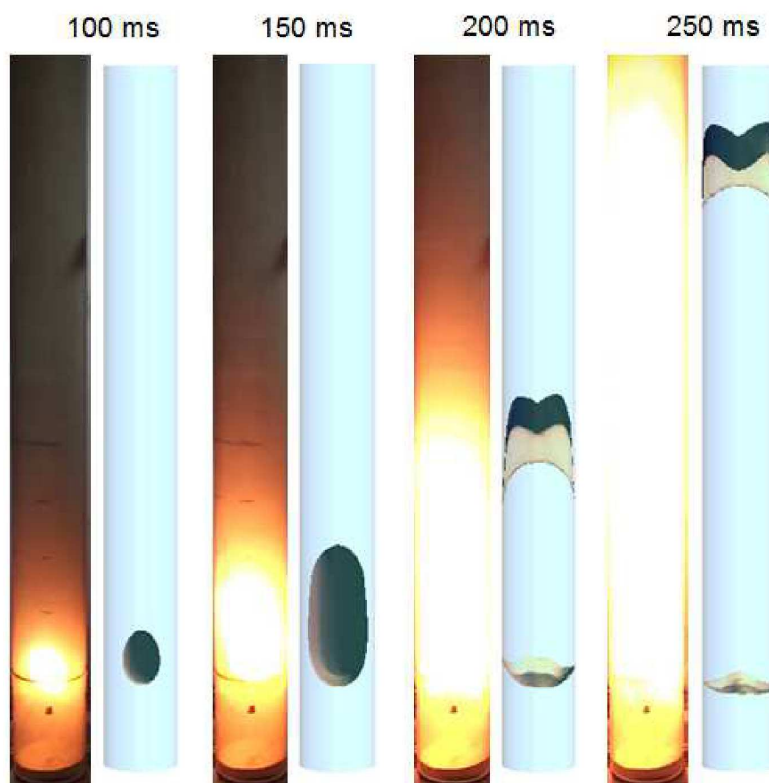

Figure 2.10: Comparison of flame propagation between experiment and simulation [81].

Some of the recent academic work in this area is based on OpenFOAM [31, 81, 83–86]. Spijker [84] developed a CFD code to model dust explosions, which is based on a flame speed approach. In describing the movement of the dust particles, a Eulerian approach was chosen because of the high particle count. The simulation result is shown in Figure 2.10 and compared with the experimental data. They fit well within the first 200 ms after ignition. After $200ms$, the momentum outside of the experimental tube causes the higher speed of the flame.

Focusing on the fundamental of particle ignition, he proposed a single-particle model for Lycopodium particles. The combustion of one Lycopodium particle was assumed with a sequence of evaporation, primary pyrolysis, secondary pyrolysis, homogeneous reactions, and tar reactions. The result of the model showed good agreement with thermal gravimetric analysis (TGA) data [81]. Later, he simplified the model based on the single-particle model. It reduced the pyrolysis and heterogeneous reaction equations to one pyrolysis equation [87].

$$\frac{\partial X_{Lignin,akt}}{\partial t} = rr = \frac{A}{X^n_{Lignin,start}} \cdot e^{-\frac{Ea}{RT}} (V_{max,i} - V_{i,akt})^n \tag{2.19}$$

Tomasch [85] investigated the interaction between particulate, inert additives, and lycopodium/air mixtures based on coalChemistryFoam solver in OpenFOAM, where the experiments of addictives were carried out by Huettenbrenner [88]. The study examined a wide range of extinguishing materials with varying responses to heat input, including water-laden particles that are capable of evaporating, as well as solid particles that undergo a simplified melting process. In water-laden particles, she introduced a second particle cloud which has multiphase composition and evaporation abilities. Models of this new cloud that are used in the simulation are listed in the third column of Figure 2.11. The second extinguishing material she introduced is melting particles, which is a completely new function. She adapted an existing model for surface reaction so that the phase can translate from solid to liquid. Simulation results indicate that water-laden particles do not significantly deviate thermal energy from the combustion zone, but rather serve to cool the mixture after the flame front has passed. Two more safety indices (One already tested in experiments): ignition energy and the flame propagation velocity.

Pollhammer [83] simulated the lycopodium injection into the $20L$ SIWEK sphere vessel (Figure 2.12). The simulation showed that ambient pressure conditions and the rebound nozzle dispersion system induced very inhomogeneous dust concentrations. To improve the homogeneity of the system, a new dispersion system using a rotating disc was designed and validated using OpenFOAM.

Model	Specifications for a *ThermoCloud*	Specifications for a *MultiphaseReactingCloud*
Dispersion model	stochasticDispersionRAS	-//-
Patch interaction model	standardWallInteraction	-//-
Heat transfer model	Ranz-Marshall	-//-
Composition model	not available	singleMixtureFraction
Phase change model	not available	liquidEvaporation
Devolatilisation model	not available	constantRateDevolatilisation
Stochastic collision model	none	none
Surface reaction model	not available	COxidationKinetic-DiffusionLimitedRate
Surface film model	none	none
Radiation	on	on

Figure 2.11: Comparison of information cotained in *properties-files for *Thermo-* and *coalCloud* in OpenFOAM 2.4.0. [85].

Particle cloud using the rebound nozzle   Particle cloud using the rotating disc
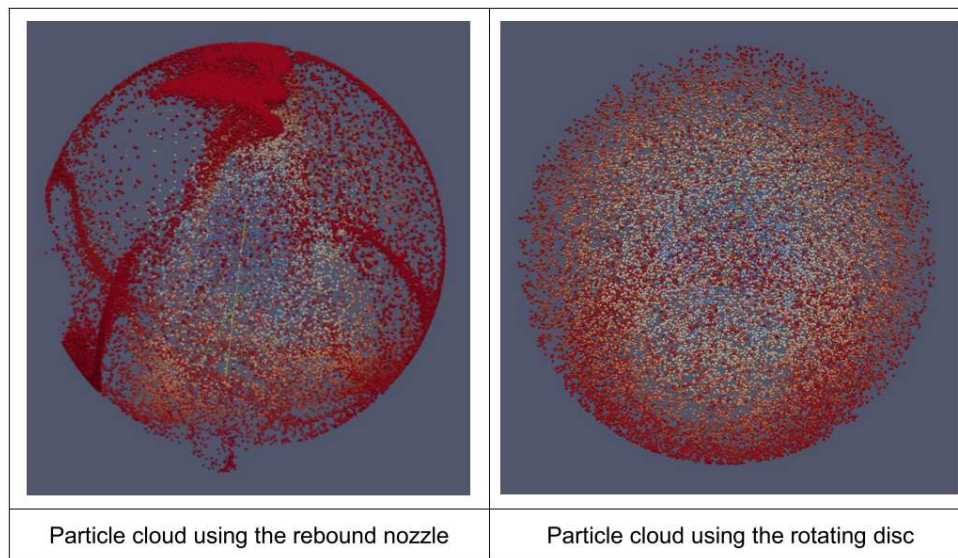
Figure 2.12: Comparison of the particle clouds using the rebound nozzle and the disc disperser [83].

Cloney [86] made modifications to the coalChemistryFoam solver in OpenFOAM to simulate coal dust explosions. The Schmidt number assumption was replaced with the Lewis number assumption to improve burning velocity predictions.

This model, which simplified mass transfer, surface reaction and devolatilization, was proved to be able to simulate the propagation processes in the dust cloud but would overpredict the intermediate species.

2.2.5 Studies in dust explosion using DESC code

The Dust Explosion Simulation Code (DESC) project started in 2002 and ended in 2004. It was supported by the Europe commission, and the principal is Travgy Skjold from the University of Bergen. Their goal is to develop a CFD code to simulate dust explosions in complex scenarios such as process plants. The code was developed based on FLame ACceleration Simulator (FLACS) when dealing with gas explosion modeling. The specialized CFD tool FLACS was developed in 1980 for process safety applications. Its solver is a three-dimensional CFD code that solves transport equations using a finite volume method on a structured Cartesian grid. Ideal gas equation of state and the standard $k - \varepsilon$ model for turbulence was used [89].

The combustion modeling of dust explosion in DESC code is similar to that in FLACS, where the character parameters, turbulent burning velocity S_T, laminar burning velocity (S_L), velocity fluctuation (u'_{rms}) and integral turbulent length scale (l_I) were used to derive models.

In the FLACS combustion model, the default empirical expression for turbulent burning velocity for premixed gaseous mixtures is:

$$S_T = 15.1 S_L^{0.784} u_{rms}'^{0.412} l_I^{0.196} \tag{2.20}$$
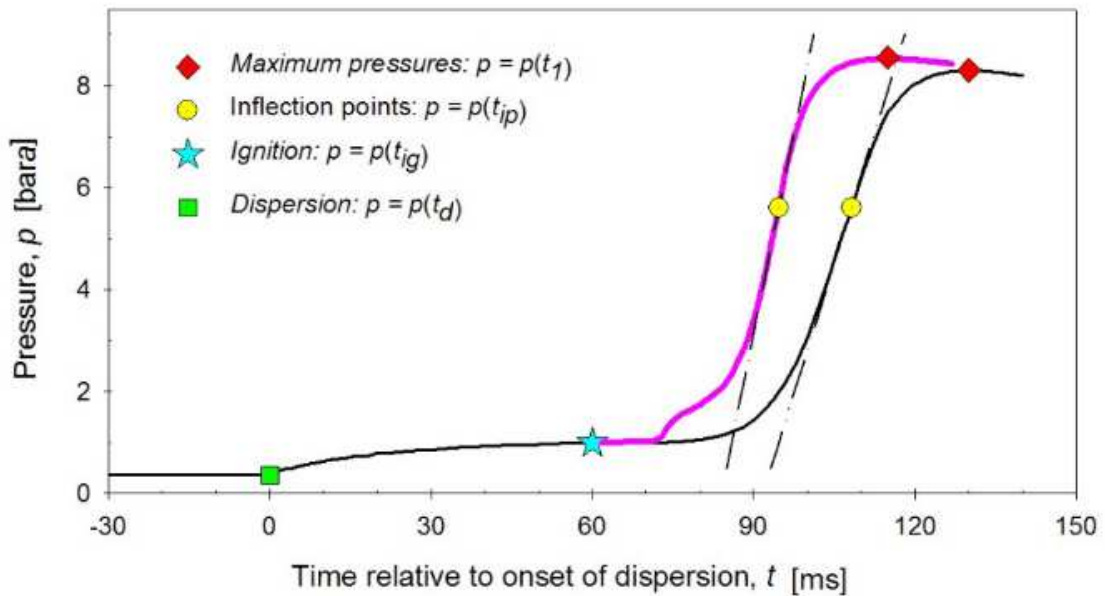
Figure 2.13: Typical pressure-time curves from a $20L$ SIWEK explosion vessel [89].

In DESC code, they introduced a empirical equation from pressure-time curve of $20L$

SIWEK vessel (as shown in Figure 2.13) experiments on the decay of u'_{rms}:

$$u'_{rms}(t_{ip}) = u'_{rms}(t_d)(\frac{t_{ip}}{t_d})^n \tag{2.21}$$

From Figure 2.13, the t_{ip} is time of the inflection point of the curve, where the maximum rate of pressure rise ($(dp/dt)_{max}$) locates. And t_d is the start time of dust dispersion.

Similar approaches were used, and the models were introduced into the code. Their simulation object aims at big plant processes lines such as pipes and connected vessels. Figure 2.14 is one example of the DESC simulation result. Both experiments and simulations were conducted on geometry. However, the results were lack of repeatability, and the value of pressure-time from experiments and simulations is not within reasonable agreements.
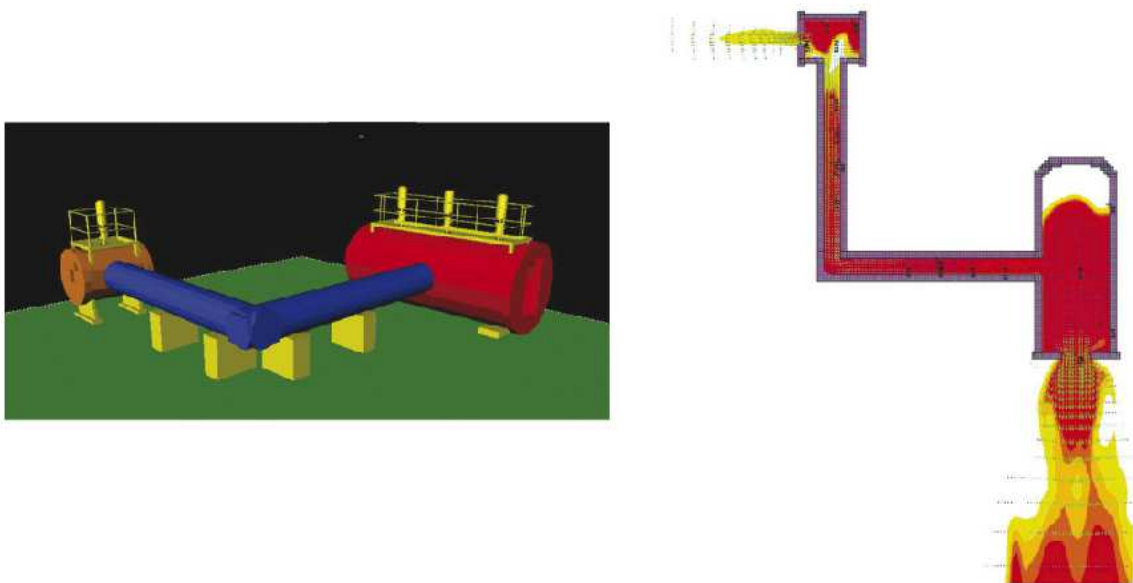
Figure 2.14: DESC representation of a interconnected vessel system geometry and a cross section illustrating simulated flame development in the system [90].

Simulation of dust explosions requires consideration of gas flow, particle motion, and chemical reactions during the explosion. Describing two-phase or multiphase flows complicates the modeling process. Usually, the model is built based on some assumptions, and it becomes especially important to choose the model correctly and validate the simulation results with the experiment. It is clear that this comprehensive numerical simulation tool is an indispensable tool for predicting dust explosion scenarios and consequences in the process industry, especially in transportation processes and in

equipment such as pipelines. Therefore, when developing a predictive simulation code for dust explosion, the results need to be based on extensive experimental verification, and the characteristics of the dust itself, its initial state, and environmental characteristics should be taken into account.

Chapter 3

Dust dispersion code

Chapter 2 discussed the utility of conventional laboratory experiments, including the modified Hartmann tube and the $20L$ SIWEK spherical vessel, in evaluating distinct properties of combustible dust clouds within process industries. These experiments involve three key stages, namely dust cloud suspension, dust ignition, and flame propagation, of which the first stage is highly significant in ascertaining the ignitability and explosibility of a given dust type. Numerous factors, such as particle size distribution, dust type, and turbulence, can significantly impact the suspended state of dust.

It is imperative to note that laboratory experiments, such as those conducted using MIKE 3 (a modified Hartmann tube), are prone to generating severe turbulence during dust injection, which can lead to difficulties in replicating experiments and ultimately result in a lower combustion rate than anticipated in explosions hazards [91]. Therefore, meticulous attention to the design and implementation of laboratory experiments is crucial to guarantee their accuracy in reflecting in-situ conditions.

In the pursuit of designing new experimental systems and achieving intrinsic safety, it is crucial to acquire a comprehensive understanding of the dust dispersion, ignition, and explosion processes. The focus of this chapter is on conducting experiments that involve the dispersion of coal dust particles of various sizes utilizing the MIKE 3 apparatus. The experimental process is meticulously recorded using a high-speed camera, and the resulting dust propagation videos are processed using MATLAB code. The analysis gives special attention to particle size, shedding light on the characteristics of the dust front.

To gain a deeper understanding of the flow field phenomenon, a three-dimensional geometry of the MIKE 3 apparatus is constructed to simulate the dust dispersion process that precedes ignition. OpenFOAM 2.4x software is then utilized to solve the two-phase flow and analyze the behavior of both particles and airflow. The findings of this study are expected to broaden our knowledge of the fundamental physics of dust explosion,

providing a platform for the development of more sophisticated experimental designs in the future. This chapter has been published in the paper [92].

3.1 Experiment studies
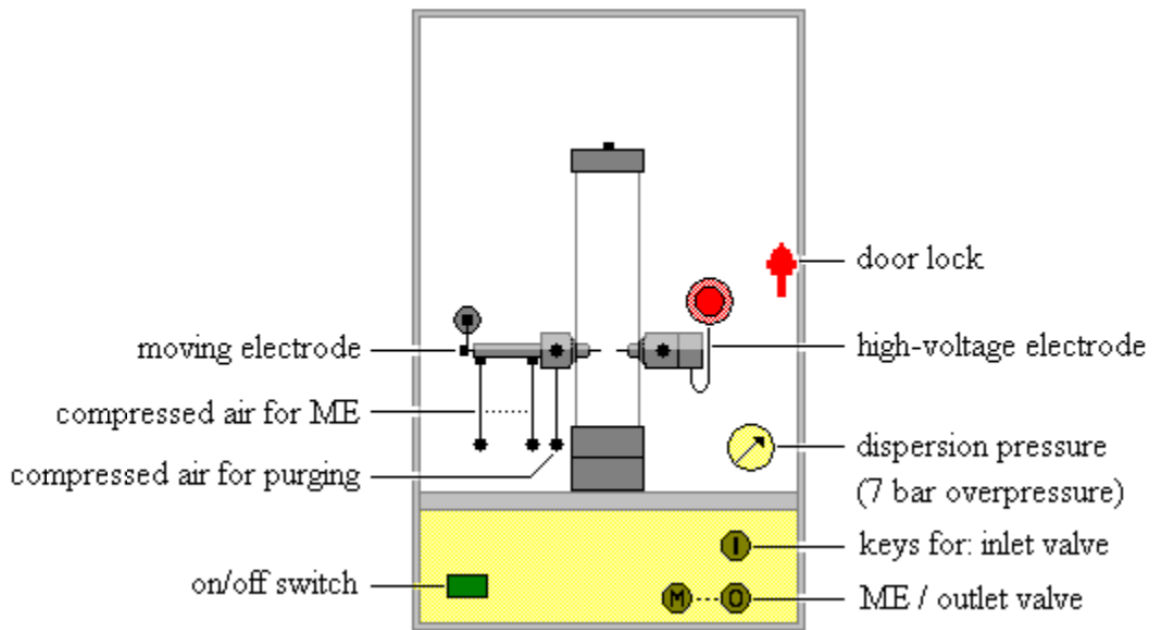
3.1.1 Experimental setup

Figure 3.1: MIKE 3 apparatus from Kühner AG [93].

This chapter presents an investigation of coal dust dispersion in the MIKE 3 apparatus, which was specifically designed for the minimum ignition energy testing of dust samples. The apparatus, illustrated in Figure 3.1, comprises an explosion tube, electrodes, and control systems. The explosion tube is a cylindrical vertical glass tube with a height of $300mm$ and a diameter of $68mm$, as shown in Figure 3.2. This tube is a modified Hartmann tube with a volume of $1.2L$.

The experimental procedure involved evenly placing the dust sample of varying masses, ranging from 300 to 3000 mg, at the bottom of the explosion tube. A dispersion system equipped with a 7 bar overpressure air tank was employed. Upon the start of the experiment, the air was released from the tank and directed to an air reservoir, where it was compressed to 7 bar. The air then flowed through a mushroom-shaped nozzle with eight evenly distributed holes, resulting in the dispersion of the dust sample and
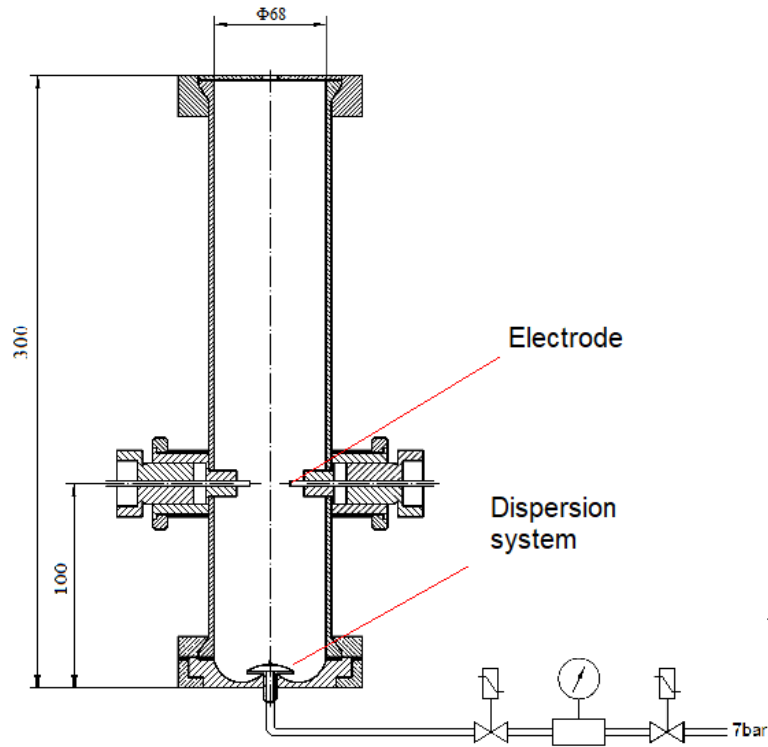
Figure 3.2: Explosion tube from MIKE 3 apparatus [93].

the formation of a dust cloud in the tube. After a defined ignition delay time, a spark discharge ignited the dust cloud.

The nozzle used in the MIKE 3 apparatus has eight holes evenly distributed around its mushroom-shaped head, which facilitates the dispersion of the dust sample and the formation of a dust cloud in the explosion tube. The spark discharge energy is capacitive, without inductance, and can be adjusted to different levels, including $1000mJ$, $300mJ$, $100mJ$, $30mJ$, $10mJ$, $3mJ$, and $1mJ$. The ignition delay time, t_v, is defined as the time between the initiation of the dust sample dispersion and the spark discharge. The MIKE 3 control system allows for the adjustment of t_v to $60ms$, $90ms$, $120ms$, $150ms$, and $180ms$. To determine the minimum ignition energy (MIE) of a given sample, a set of values for the dust sample mass, spark energy, and ignition delay is determined in the initial tests, with subsequent tests varying one parameter at a time to restrict the MIE to a specific range. The MIE is defined as the minimum energy value (E2) at which ignition occurs, and the maximum energy value (E1) at which ignition is not observed in at least ten successive experiments [94].

In order to investigate the effect of particle size on dust explosion, it is necessary to conduct dispersion tests with dust of different sizes. Dust dispersion is a critical aspect

32

of dust explosion and, thus, was studied in the MIKE 3 apparatus to explore the impact of particle size on dust cloud formation. The experiments were performed under ambient pressure and temperature conditions, with a dust sample mass of $900mg$. To ensure the consistency of the results, each size range of the dust was tested five times. The aim of the study was to investigate the influence of particle size on dust dispersion, and, to prevent the ignition of dust, the spark of the electrodes was turned off. Additionally, a high-speed video camera with a frame rate of 400 fps was used to record the experiment.

For the purpose of investigating the size effect on coal dust explosion, a single type of raw coal sample was employed in this study. Firstly, the raw coal was subjected to crushing and grinding using a crusher. Subsequently, the coal dust was dried in an oven at a temperature of 120 °C for 12 hours. The dried coal dust was then sieved using a sieve shaker to obtain particles with sizes within seven different ranges, namely $20 - 32\mu m$, $32 - 45\mu m$, $45 - 63\mu m$, $63 - 71\mu m$, $71 - 125\mu m$, $125 - 250\mu m$, and $250 - 500\mu m$.

3.1.2   Dust front position capture based on grey scale filter
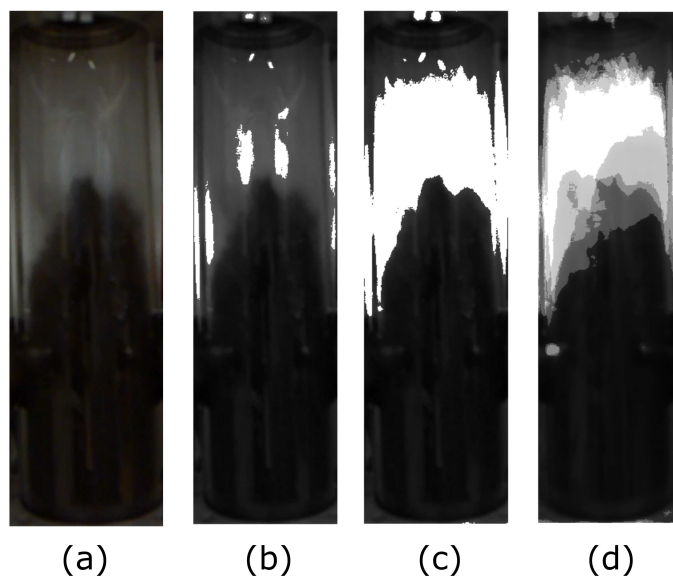
Figure 3.3: Coal cloud image filtered by grey level: (a) original image; (b) filter range (0 90); (c) filter range (5 60); (d) ensemble average of five repeated cases.

The most intuitive manifestation of dust movement is the position and shape of the dust front. The capture of the dust front shape is helpful in understanding the motion state of air in the flow field. In image processing, there is a common method using the grey scale to represent the weight of darkness in the pictures. Unlike dust explosion, coal dust does

not have RGB (the three primary colors: Red, Green, and Blue) values. The dispersion tube has a white background in the coal dust dispersion, which contrasts with the black coal dust. Therefore, in the post-processing of the dust dispersion video, we used the greyscale filter to define the dust front grey weight. Based on the weight value, the dust front movement characteristics are extracted. According to the dust front positions and shapes in each frame of the high-speed video, the dust propagation speed is investigated.

Figure 3.3 is the process of dust front extraction, where Figure 3.3(a) is the original image from one frame of the high-speed video. The Figure 3.3(b)-(c) are filtered by different thresholds concerning the grey level. The coal dust front is hard to be determined by eyes due to the blurring effect in the dust front. When converted to the grey image, the grey level of Figure 3.3a varies from 1 to 255; the higher number represents a brighter pixel. The filter range of (0 90) does not exclude the blank region. Finally, a range of (5 60) is used after multiple tests on different frames. The range is adjusted in different tests in case of changes in room brightness. Figure 3.3(d) is the ensemble average of the five repeated tests. It averages the grey values in five different filtered images. The overlapped region is darker and shows the place coal cloud exists in all five tests. Another less dark dust front is the variation in each test. In the example, the dust front tends to the right wall. The shape of the dust front end is less like a parabola but more similar to a trapezoid. Except for one case, the positions of the dust in front of other cases are basically the same.

3.1.3 Experimental results

Two example pictures from the recorded video are shown in Figure 3.4. They illustrate the development of dust dispersion in MIKE 3. As the study focuses on the filling-up process, the dust was not ignited as it was designed. The filling-up process is very rapid and forms a dust cloud inside quickly. When the dust moves inside of the tube, the wall effect from the tube slows down the velocity of near-wall particles and thus distorts the dust front shape. The shape of the dust cloud font starts to form a parabolic shape after it passes the electrodes. The dust front is not a clear curve but blurring because of part of the high-velocity particles.

The dust front position data over time is shown in Figure 3.5. The movement of each cloud class has a similar pattern for all sizes of particles. Except for the $250 - 500\mu m$ particles, the other dust samples which are under the critical size of $250\mu m$, have very close time history curves. This could be the reason for particle agglomeration. Especially, the smallest sample does not have the highest velocity and the velocity of $71 - 125\mu m$ sample prevails a little in the later time of dispersion.

(a) 0.015 s   (b) 0.043 s
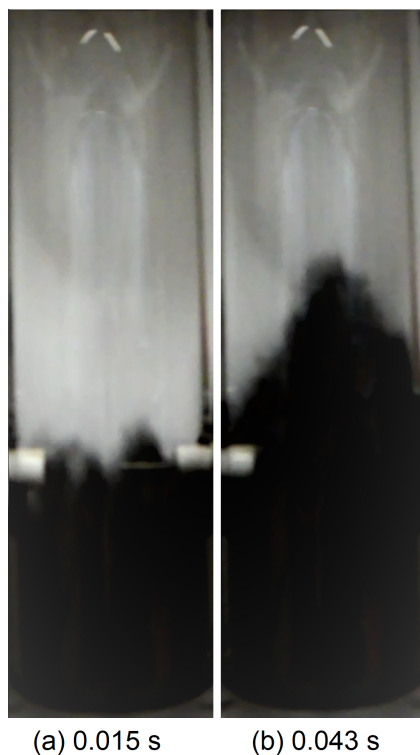
Figure 3.4: Instants of coal dust dispersion in MIKE 3 apparatus.
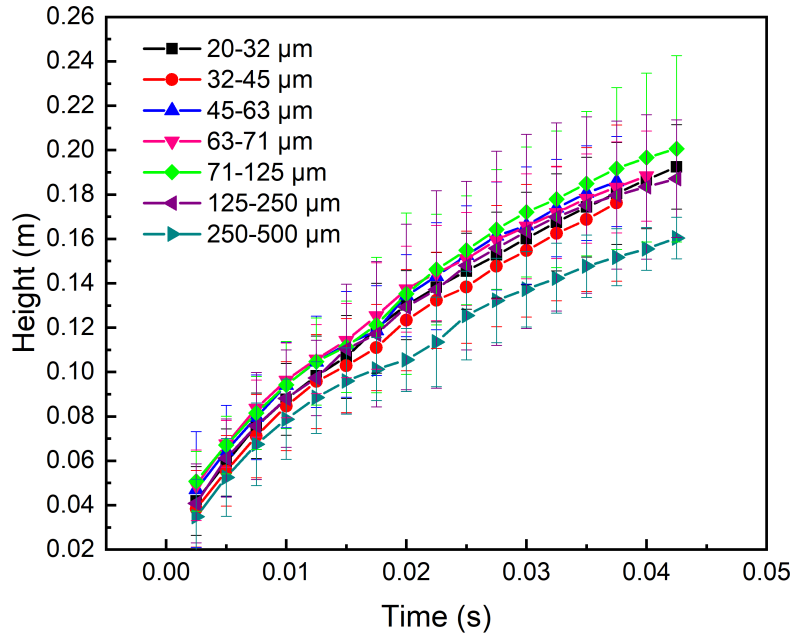
Figure 3.5: Coal dust front positions over time in different size classes.

3.2 Simulation studies

3.2.1 Lagrangian approach for dust particles tracking

This section describes the models used in this work. To investigate the particle size effect, the Lagrangian approach must be used to discrete the coal particles. The computational methods are based on the compressible transient solver rhoPimpleFoam solver from the OpenFOAM toolkit version 5. The air blast is compressible and the biphasic flow is with high turbulence. The default solvers involve additional models that can impose significant computational demands, such as particle chemical reactions and particle volume fractions. However, the emphasis here is on understanding the impact of particle size on dust dispersion, sedimentation, and biphasic flow turbulence. Consequently, the solver has been adjusted to accommodate the evolution of the biphasic flow, rather than relying on the default Lagrangian solvers. Core solver adjustments entail introducing a solid phase and coupling momentum and energy between the two phases.

36

Gas phase equation

In the two-fluid model, the gas phase is considered as a continuous phase and described using the Navier-Stokes equations. On the other hand, the particles are treated as mass points without any volume and experience momentum exchanges with the gas phase. The transport of the gas phase is accomplished by solving the transient, three-dimensional equations for mass, momentum, and enthalpy. To model the turbulence effects, the widely accepted $k - \varepsilon$ model is employed. Additionally, the coupling transport equation incorporates the source term from Lagrangian particles.

The continuity equation governing the conservation of mass in the gas phase can be expressed as:

$$\frac{\partial \rho}{\partial t} + \nabla \cdot \phi = S_{\rho}^{p} \tag{3.1}$$

where ρ is the fluid density (kg/m^3), ϕ is mass flux ($kg/m^2 \cdot$s).

The coupling between the particle and gas phases is achieved in the momentum equation by introducing a solid momentum source term that influences the gas phase.

$$\frac{\partial \rho \vec{U}}{\partial t} + \nabla \cdot (\phi \vec{U}) - \nabla \cdot \Sigma + \nabla \cdot p = S_{\rho \vec{U}}^{p} \tag{3.2}$$

where $\vec{U}$ is the fluid velocity (m/s), Σ is the viscous stress tensor ($kg/m^2 \cdot s$). p is fluid pressure (Pa). S_{ρ}^{p} is the particle momentum.

The enthalpy equation is:

$$\frac{\rho h}{\partial t} + \nabla \cdot (\phi h) + \nabla^2 (\alpha_{eff} h) = S_{\rho h}^{p} \tag{3.3}$$

where h is fluid enthalpy (J/kg), α_{eff} is effective thermal diffusivity (m^2/s), $S_{\rho h}^{P}$ is the source term of heat transfer between two phases.

Lagrangian approach for dust particle tracking

The default single-phase solver rhoPimpleFoam was modified to include the gas-particle interaction due to the drag force (Figure 3.6-3.7). To couple discrete and continuous phase equations, the SLGThermo model was implemented. It is a thermo package for single-phase or multiphase flows that provides thermodynamic values for the elements in each phase. Due to the interaction of two phases, a two-way coupling was considered in the scheme to solve the equations until the solutions in both phases reach convergence.

By considering all the forces acting on particles during dispersion, a force balance

$$\iiint_\Omega div\boldsymbol{A}\, dv = \oiint_\Sigma \boldsymbol{A}\cdot\boldsymbol{n}\, ds$$
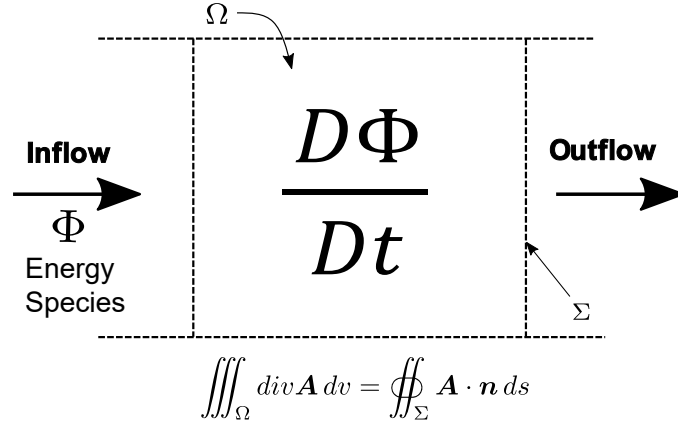
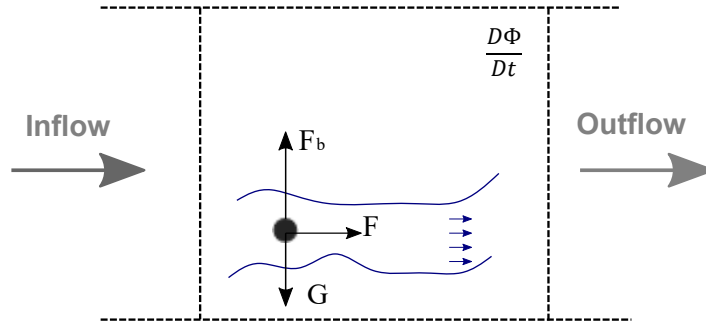Figure 3.6: Schematic of the particle fluid interaction in rhoPimpleFoam.

Figure 3.7: Schematic of the particle fluid interaction in rhoPartPimpleFoam.

equation was derived for each particle in accordance with Newton's second law. The particle phase is denoted by the subscript p. This approach enabled the determination of particle trajectories [95].

$$m_p\frac{\partial^2 x_p}{\partial t^2} = m_p[F_D(u - u_p) + \frac{g(\rho_p - \rho)}{\rho_p}] \tag{3.4}$$

where m_p, x_p, u_p, ρ_p are the particle mass (kg), position (m), velocity (m/s), and density (kg/m^3), respectively. The terms on the right side of the Equation 3.4 are the drag force and the gravity. The drag force $m_p F_D(u - u_p)$ is calculated depending on the particle Reynolds number (Re_p) and drag coefficient (C_D) [96].

$$F_D = \frac{0.75\mu C_D Re_p}{\rho_p d_p^2} \tag{3.5}$$

$$Re_p = \frac{\rho_p d_p|u - u_p|}{\mu} \tag{3.6}$$

d_p represents the particle diameter (m), and μ is the dynamic viscosity $(kg/(ms))$. Owing to the interaction between the two phases, a multitude of forces participate in the

dispersion process. However, in this study, certain forces present in the two-phase system, such as the lift force arising from the pressure difference on particles due to differences in velocity, are not considered. The impact of the lift force on the trajectories of particles is found to be insignificant [96]. Considering the diminutive size of the particles, the buoyancy force and drag forces play a substantial role in the dispersion process. In the present work, particle-particle interactions are neglected since the particle movement direction is unidirectional.

The Pressure-Implicit Method for Pressure Linked Equations (PIMPLE) algorithm was employed to perform pressure-velocity coupling. PIMPLE is a combination of the Semi-Implicit Method for Pressure Linked Equations (SIMPLE) algorithm and the Pressure-Implicit with Splitting of Operators (PISO) algorithm. The fluid field is treated as a steady state in each time step, and the SIMPLE algorithm is utilized. The PIMPLE solver was configured with 22 outer correctors and was preferred due to its capability to adjust the time step based on the Courant-Friedrichs-Lewy (CFL) number.

3.2.2 Numerical domain

The MIKE 3 apparatus flow domain was modeled in order to facilitate further investigation. Two air injection methods were considered when constructing the simulation geometries. The dispersion domain geometry, depicted in Figure 3.8, is structurally identical to the MIKE 3 apparatus, except for the inlet configuration. The dispersion tube is a vertical cylinder with a capacity of $1.2L$, featuring a nozzle at the bottom and an outlet at the top. Two symmetrical electrodes are positioned on the body of the dispersion tube to ensure experimental consistency. The cylinder tube has a height and diameter of $300mm$ and $68mm$, respectively. The flow domain comprises 509,942 hexahedral cells. Eight uniformly distributed holes are located inside the nozzle to facilitate even dispersion of the dust. The first system, system a, represents a simplified inlet system characterized by continuous pressurized air at $700kPa$. This system was designed to investigate the effect of the inlet on particle dispersion. In contrast, the second system, system b, features a $50mL$ compressed air tank with an air valve that opens at the start of the simulation. Consequently, system 1 possesses an inlet boundary condition while system 2 has an air tank but no inlet. The internal flow domain was initialized with atmospheric pressure, which is consistent with the laboratory environment. The magnitude of the velocity field is assumed to be negligible, and the total pressure corresponds to atmospheric pressure. The outlet velocity boundary condition is set to zeroGradient, and no-slip conditions are imposed on the tube wall, resulting in zero fluid
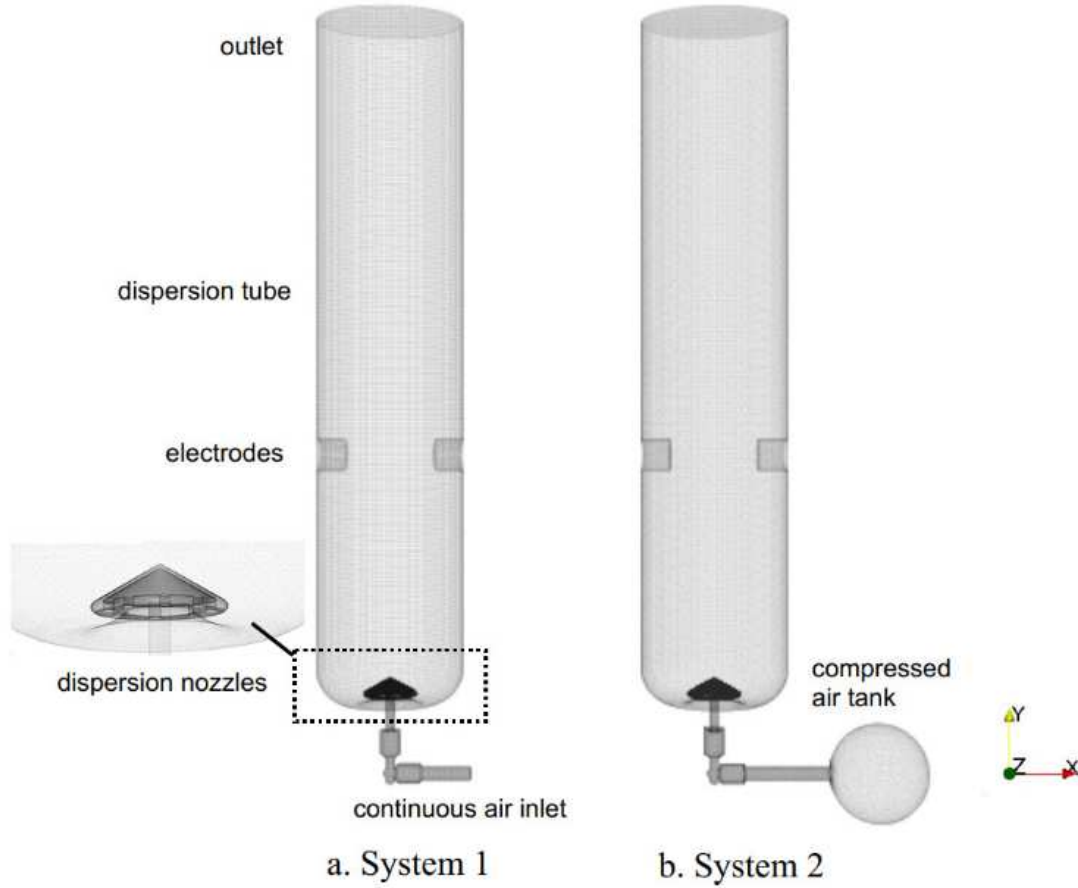
Figure 3.8: Flow domains of the simulation models. (a) system 1: continuous pressurized air injection. (b) system 2: $50mL$ compressed air injection.

velocity on the wall. Table 3.1 summarizes the boundary conditions applied to the system.

Table 3.1: Boundary conditions for three-dimensional particle dispersion simulation.

Variable	Inlet boundary	Outlet boundary	Value
Pressure	totalPressure	fixedValue	$8 \cdot 10^5 Pa$, $1 \cdot 10^5 Pa$
Temperature	fixedValue	zeroGradient	$300K$
Velocity	zeroGradient	zeroGradient	$0.0m/s$

For the simulations, uniform distributed coordinates for coal particles were generated using MATLAB (see Figure 3.9). On the curved bottom of the flow domain, $900mg$ of discrete particles were initially generated using the *manualInjection* model. The coal dust used in each simulation had a uniform diameter. The diameters of the inserted dust for different conditions were $25\mu m$, $125\mu m$, and $250\mu m$, with a density of $1007kg/m^3$. The number of particles for each case was too large to calculate their trajectories in the Lagrangian method. Therefore, the thermodynamic parcels method was implemented

to save computation time. This method scales down the particle numbers to 364,300 representative parcels. With this method, the conservative equations are calculated for only part of the particles and then transferred to the whole cloud.
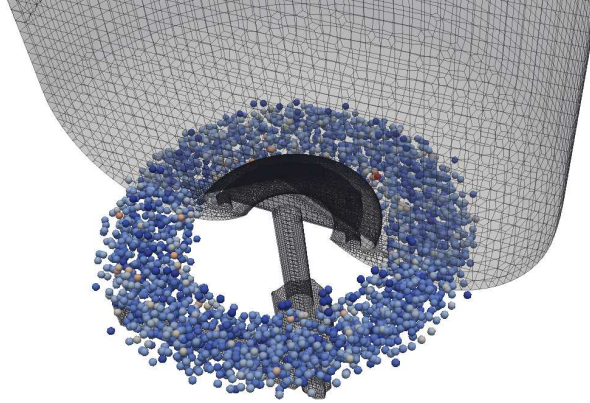
Figure 3.9: Initial positions for particles in dust dispersion simulation.

3.2.3 Particle propagation and flow properties
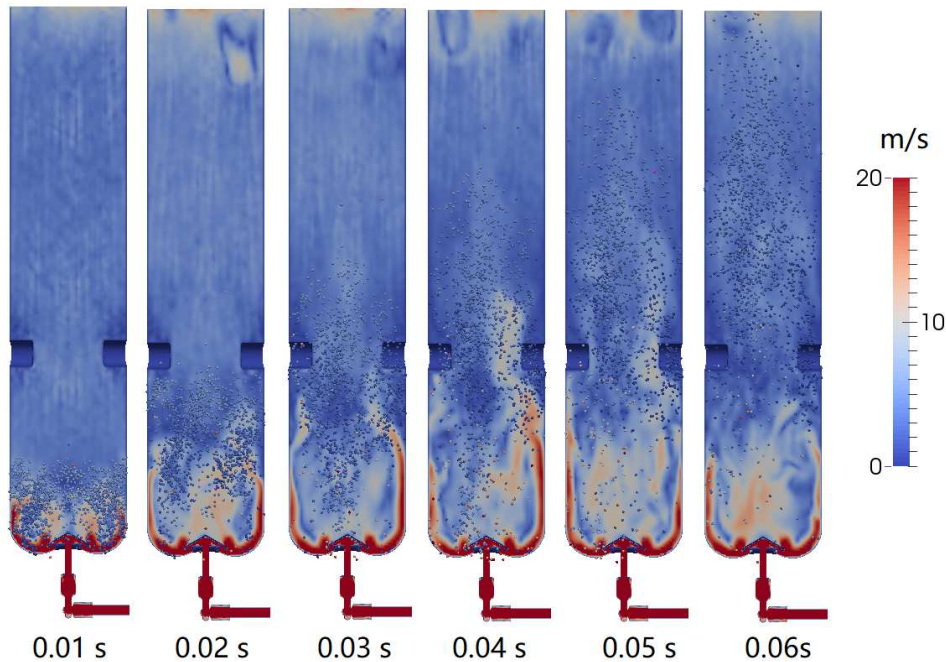
Figure 3.10: Velocity field of $25\mu m$ coal dust cloud dispersed inside of MIKE 3 apparatus.

Figure 3.10 depicts the velocity of the gas field and the position of a $25mm$ particle at different times. At $0.01s$, the particles are lifted up as the velocity field builds up. The

highest velocity is observed at the bottom, close to the round wall and the outer rim of the nozzle. Consequently, there are more particles on the two sides of the tube than in the center. The velocity magnitude in the upper part of the tube increases and exhibits a corrugated appearance due to turbulence. From $0.02s$ to $0.03s$, the velocity field near the wall changes with time. The high-pressure field region near the wall increases, and the particles scatter evenly over the tube when they surpass the high-velocity near-wall region. Finally, the particles are pushed to the whole domain as a result of the high inlet air velocity.

The front of the particles assumes a round shape after $0.03s$. At $0.05s$, the velocity field is fully built up when most particles leave the bottom part. Because of the constant inlet pressure, the flow velocity increases when the momentum exchange between the two phases reduces. At the time of $0.06s$, the particles have reached the outlet of the tube, while most particles are distributed above the electrodes. In dust explosion experiments, the dust is ignited at $0.06s$. From the simulation result, it can be observed that the dust cloud is not homogeneously dispersed in the domain. The front and bottom of the particles have lower particle concentrations than the middle region of the cloud, which can be observed after $0.03s$. When the dust concentration near the ignition electrodes is too low, the tested minimum ignition energy of the dust sample will be higher than the actual value, resulting in inappropriate safety instructions.

3.2.4   Investigations on the inlet boundary conditions

The consideration of boundary conditions is essential for obtaining accurate results in CFD simulations. While system 2 features the same inlet gas setup as that of MIKE 3, its utilization would result in a considerable increase in simulation time.

To mitigate the computational effort involved in inlet condition modeling, researchers often simplify the inlet condition using a pressure decrease model [95]. In this study, a $25\mu m$ case was simulated using this approach for validation purposes. Key data, including the inlet velocity, pressure, turbulent kinetic energy, and dissipation of turbulent viscosity, were recorded and will be utilized in the subsequent simulation of the $125\mu m$ and $250\mu m$ cases.
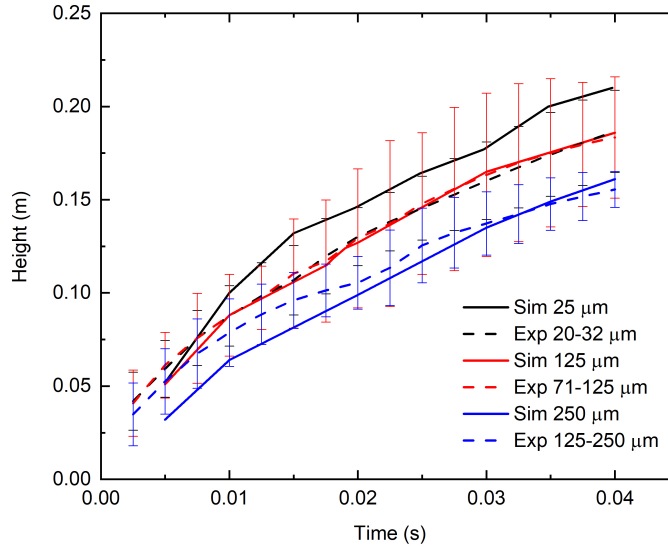
Figure 3.11: Temporal comparison between dust front positions from simulation and experiment.

Figure 3.11 illustrates a comparison between simulation and experimental results of the front position of pulverized coal particles in the dispersion tube over time. The experimental results were derived from the work of Pan [97]. In the experiment, coal particles of three size ranges moved towards the top of the pipe over time. During the process of kinetic energy transfer, large particles mostly convert the energy obtained from the gas into potential and kinetic energy. Larger particles require more energy to be raised to a certain height than smaller particles, resulting in lower kinetic energy for larger particles. Consequently, coal particles in the $125-250\mu m$ range move slower than those in the other two size ranges. The particles of $20-32\mu m$ and $71-125\mu m$ move at almost the same speed due to particle agglomeration phenomenon during their movement [95], leading to reduced motion speed. However, the present study utilizes the Lagrange particle tracking method to investigate the relationship between flow field and particle motion in MIKE 3. Therefore, particle agglomeration is not considered.

In the simulation results, particles of all three sizes move at similar speeds, with faster particle movement at the earlier stage due to higher fluid velocity flowing out of the nozzle. As the particle position rises and the nozzle inflow velocity decreases, particle movement speed reduces. Among the three sample sizes, larger particles move slower. The simulation results for the $125\mu m$ size are almost consistent with the experimental results for $125-250\mu m$ size. In the simulation of $25\mu m$ size, particle agglomeration is not considered, resulting in faster movement than the experimental results. The simulation

43

results for the $250\mu m$ size agree well with the experimental results. However, at the early stage of the flow, the particle velocity is lower than that of the experiment because the simulated particle is mono-sized ($250\mu m$), and the particles smaller than $250\mu m$ in the experiment tend to reach higher velocity at the early stage, resulting in faster dust front movement.

3.2.5 Investigations on the flow field properties
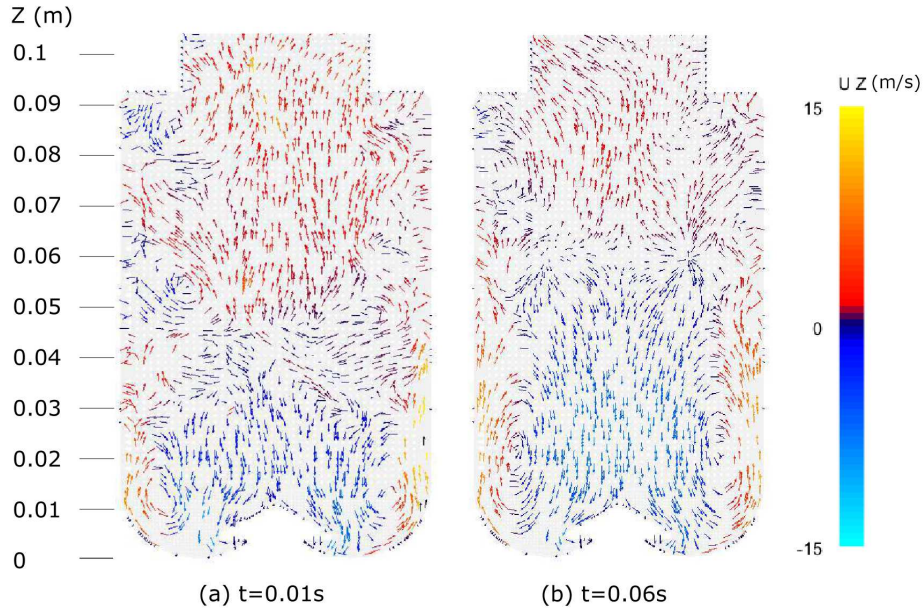
Figure 3.12: Evolution of air velocity scalar in the z-direction at the lower part of the dispersion domain. Profiles at (a) $t = 0.01s$, (b) $t = 0.06s$.

Figure 3.12 depicts the direction of gas flow in the vertical cross section passing through the electrodes (x-z plane). The velocity component in the z-direction (along the tube) is considered, and the height of the tube is indicated. Figure 3.12a-3.12b display the flow patterns at the earlier stage of $0.01s$ and the late-stage of $0.06s$ of the dispersion, respectively. After $0.01s$, the air ejected from the mushroom-shaped nozzle reaches the bottom of the tube and moves upward along the wall. Due to the high-speed airflow causing a decrease in pressure, the gas nearby is drawn to the lower part of the tube, resulting in the appearance of airflow vortex at both sides of the tube's lower part. Part of the high-speed gas at the wall continues to move upward, pushing the particles upward. As the electrodes act as a barrier, air velocity increases as it passes through them, leading to particle accumulation in crevices beneath the electrodes. After $0.06s$, the velocity of airflow in the mushroom nozzle decreases, and a significant amount of dust moves to the

middle of the tube. Consequently, the airflow vortices grow, and the amount of downward flowing air decreases. The overall velocity value in the tube decreases due to the energy transfer between air and solid.
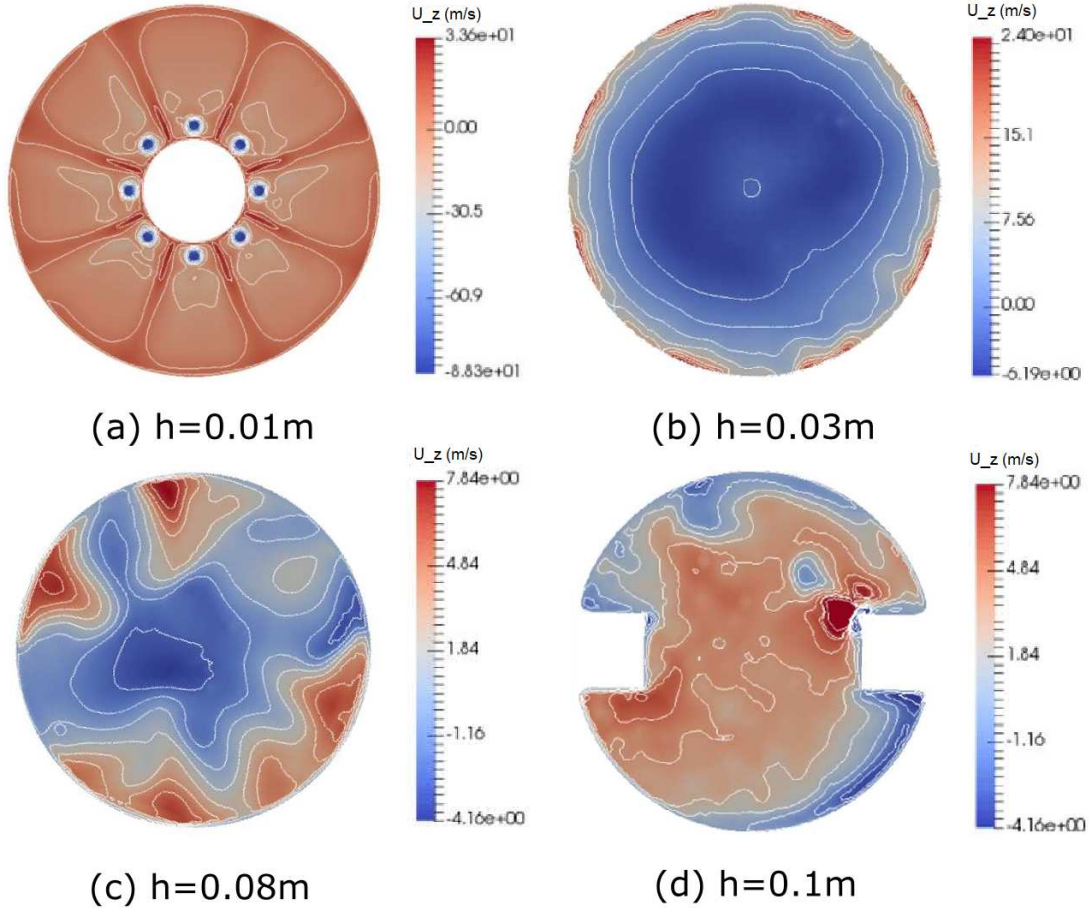
Figure 3.13: Velocity field at different height of cross sections (t=0.04 s). Profiles at (a) $h = 0.01m$, (b) $h = 0.03m$, (c) $h = 0.08m$, (d) $h = 0.1m$.

Figure 3.13 presents the fluid velocity contour map at different horizontal cross sections (x-y plane) in the tube, where (a), (b), (c), and (d) are the cloud images of velocity scalars in the z-direction at four heights in the tube: $0.01m$ (nozzle), $0.03m$, $0.08m$, and $0.1m$ (the height of electrodes). In Figure 3.13a, the air is blown towards the bottom of the tube from eight evenly distributed nozzles, passing through the curved bottom of the tube and finally lifting the particles. Consequently, the velocity at the nozzles of this section is negative, and the velocity elsewhere is positive. As the space becomes larger after the air is ejected, the gas expands rapidly, and the velocity decreases. The air velocity increases slightly near the wall. Since the velocity field in each nozzle is consistent, the velocity distribution is almost axisymmetric at this cross section. At the cross section $0.03m$, the velocity value is lower than in Figure 3.13a due to air expansion

and wall friction. The air near the wall has the highest velocity, and the velocity reduces as it moves away from the wall. In the large area of the cross section, air flows to the bottom of the pipe up to $6m/s$. The gas pressure decrease in the near-wall region when the air blasts upwards causes backflow in the central region, leading to a maximum velocity near the wall and reduced velocity away from the wall. In Figure 3.13c, the high-velocity airflow develops towards the center of the tube, and the overall velocity value decreases. The area with negative velocity gradually reduces. In Figure 3.13d, due to the obstruction of the electrodes, the airflow velocity between the electrodes is higher than the velocity at the wall.

3.2.6   Investigations on the particle size effects
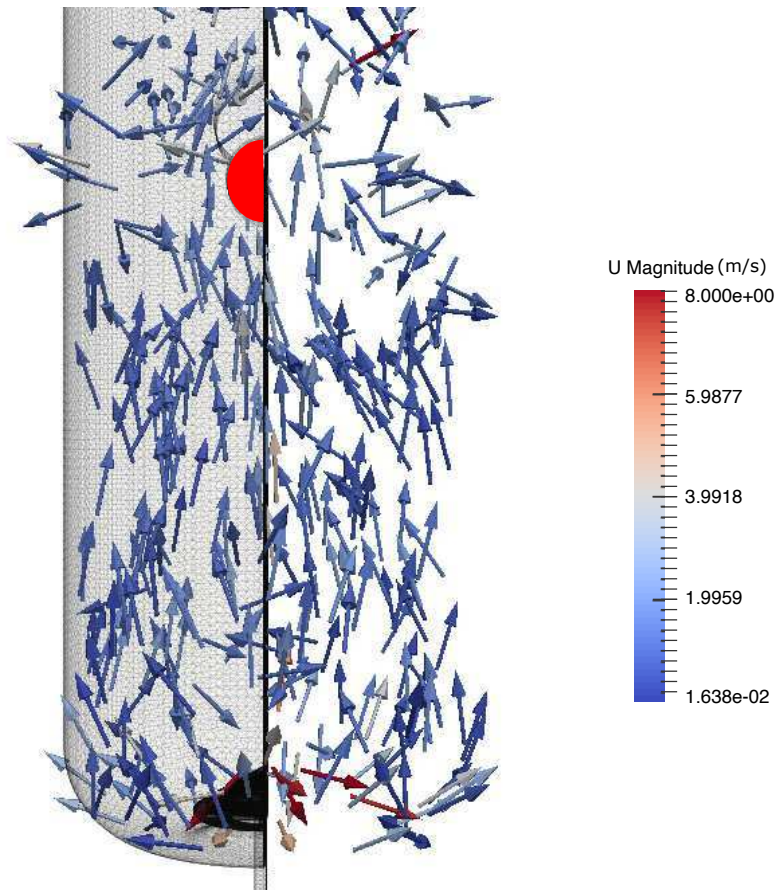
Figure 3.14: Particle movement directions and velocities at $0.04s$.

To take a closer view of the particle trajectory, the velocity direction was plotted, as shown in Figure 3.14. Due to the pressurized flow, the particles near the nozzles have the highest velocity, which moves in the negative z-axis coordinate. When the particles hit the wall, they moved inward. Therefore, the particles in the center then gradually move

upwards. The particle movement is also affected by the electrodes, which is marked with the red semicircle. The particles which meet the electrodes would bounce back, resulting in a large number of particles to be held behind. The wall remarkably reduces the particle velocity.
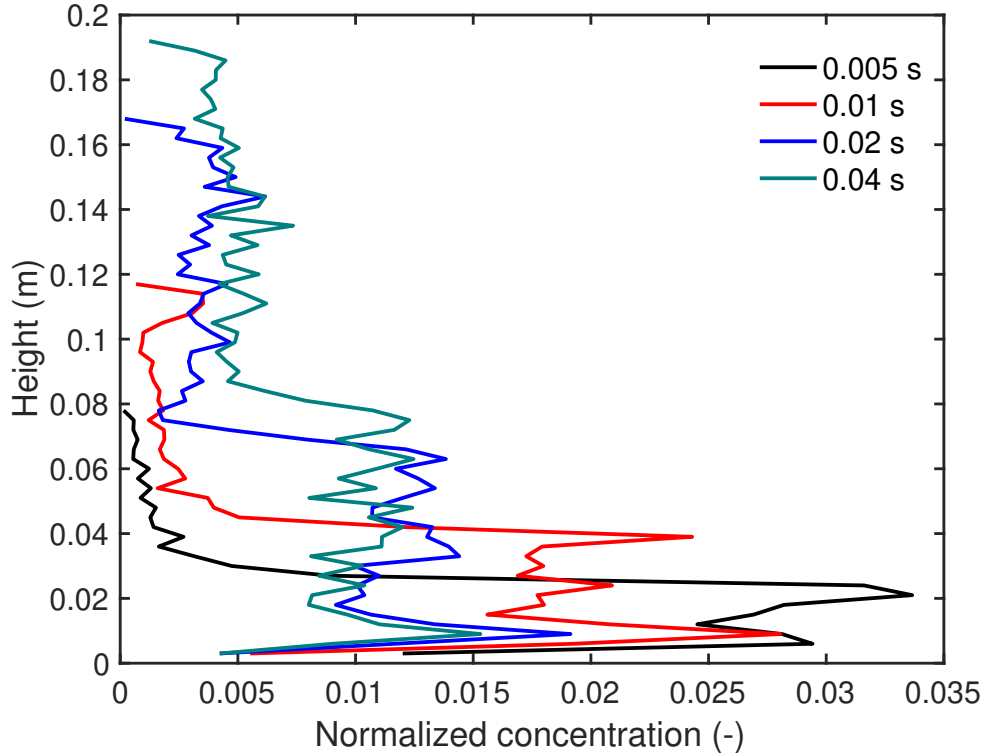
Figure 3.15: Normalized particle concentration along with the flow domian at different times (system 1).

In Figure 3.15 the normalized particle concentrations along the axis of the tube at four different times were depicted. In the beginning, particles are accumulated on the bottom of the tube near the nozzle. Between $0m$ and $0.03m$, there is a concentration gap because the gas flow separated the particles into two moving directions. The first few particles are able to move upward when they reside in the high velocity region and gain more momentum than the other group. Few other particles remained behind because of interaction with the wall. At the time of $0.1s$, a small number of particles have moved to the electrodes, while most of them are in the lower part of the tube. At a time of $0.2s$ and $0.4s$, the dust front moves slower than the first few seconds due to the momentum loss. The concentration increases in the upper part of the tube, however, due to the hinder of the electrodes, about two-third of particles accumulated in the lower part of the flow domain.
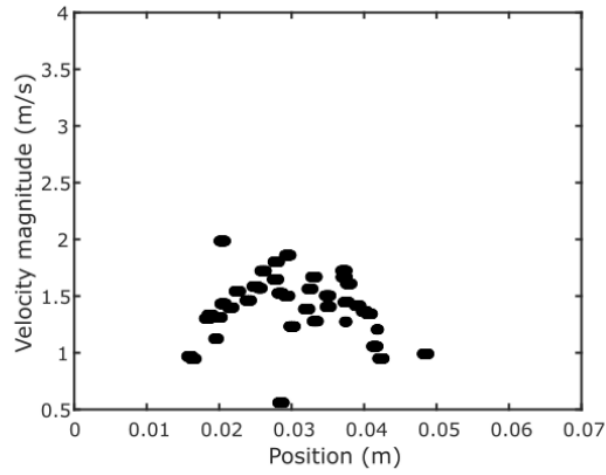
(a) h=0.2m
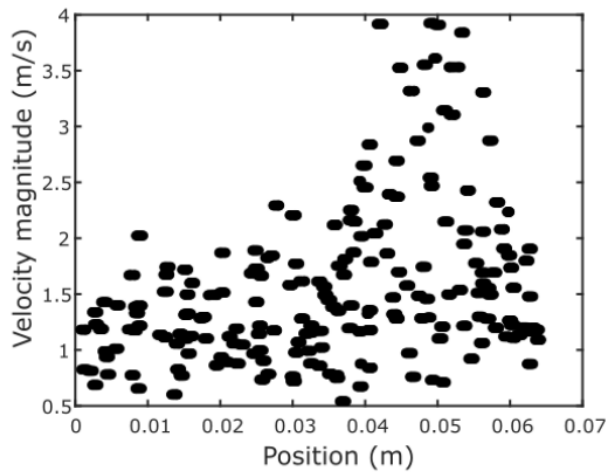
(b) h=0.1m
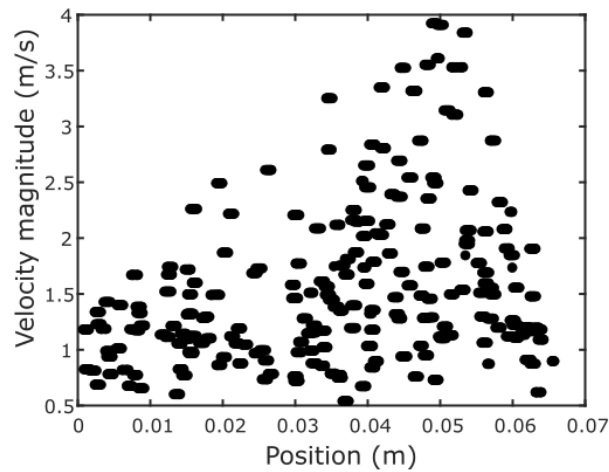
(c) h=0.08m

Figure 3.16: Particle distribution and velocity magnitude at different transversal areas ($t = 0.04s$).

Figure 3.16 illustrates the velocity distribution of the dust cloud at three transverse areas. The selected areas for analysis were the dust front level ($z = 0.18m$), the electrodes level ($z = 0.1m$), and the lower part level ($z = 0.05m$). At $0.04s$, particles moved to the upper part of the tube. It is evident from the plots that the dust front level has the least number of particles. The velocity magnitude of particles is less than $2m/s$, and they tend to accumulate near the axis of the dispersion tube. At the $0.1m$ level, the expansion of injected gas and the associated pressure decrease resulted in a more uniform velocity profile in the middle region of the dispersion tube. With a few exceptions, the velocity of particles is below $2.5m/s$, and they are more or less uniformly distributed across the transverse area. At the $0.05m$ level, particles form a peak with those close to the axis reaching a velocity of $4m/s$. The velocity of particles decreases as they approach the wall due to wall effects.
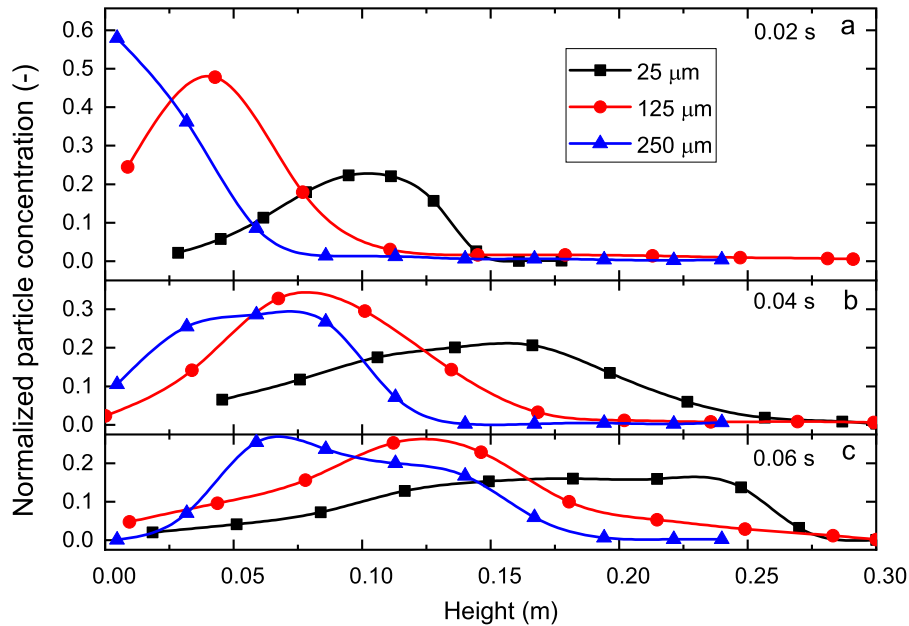
Figure 3.17: Comparison of simulation and experimental results of dust front positions over time.

The front position of pulverized coal particles in the dispersion tube over time is compared between simulation results and experimental results in Figure 3.17. In the experiments, particles of three size ranges move upward over time. During kinetic energy transfer, larger particles convert most of their energy into potential and kinetic energy, leading to a slower upward movement compared to smaller particles. Thus, coal particles in the $125-250\mu m$ range move slower than particles in the other two size ranges. Particles

of $20-32\mu m$ and $71-125\mu m$ move at a similar speed, which could be due to agglomeration of small particles during movement, resulting in reduced motion speed [98]. The Lagrange particle tracking method was employed in this study to examine the relationship between the flow field and particle motion in MIKE 3. As such, particle agglomeration is not accounted for.

The simulation results indicate that the particles of the three sizes have similar movement patterns, with faster movement observed at the earlier stage due to the higher velocity of the fluid ejected from the nozzle. As the particle position increases and the nozzle inflow velocity decreases, the particle movement speed decreases. Among the three particle sizes, larger particles move more slowly. The simulation results of the $125\mu m$ size are nearly consistent with the experimental results of the $125-250\mu m$ size. However, in the simulation of the $25\mu m$ size, particle agglomeration was not considered, leading to faster particle movement than that of the experimental results. The simulation results of the $250\mu m$ size agree well with the experimental results. During the early stages of the flow, the particle velocity in the simulations is lower than that of the experiment, primarily because the simulated particle is mono-sized ($250\mu m$), while the experiment includes particles smaller than $250\mu m$ that tend to move at higher velocities during the early stage, resulting in a faster dust front movement.

3.3   Summary

This chapter presents the development of a Lagrangian particle tracking model for simulating dust dispersion in a tube using CFD. Three particle sizes were considered in the simulations, namely $25\mu m$, $125\mu m$, and $250\mu m$. The simulation results were compared with experimental data, and good agreement was observed for the $125\mu m$ and $250\mu m$ cases. However, the slower movement of smaller particles in the experiment due to agglomeration led to faster dispersion in the simulation of $25\mu m$ particles.

The simulations also revealed the presence of flow vortices in the lower part of the tube, which entrained particles and caused them to accumulate beneath the center of the tube. The highest air velocity was found to be on the wall of the tube below the electrodes, with the velocity between the electrodes being the highest due to flow obstruction and field development.

The concentration distribution of particles during the dispersion process was analyzed, and it was found that small particles moved more slowly than large particles. The dust cloud had lower concentrations at both ends and a higher concentration in the middle. High particle concentrations were observed near the electrodes at $0.06s$ for

50

the $125\mu m$ and $250\mu m$ particles. The study suggested that the distribution of the dust cloud in the tube is a critical factor affecting dust explosion experiments, and for particles larger than $125\mu m$, the ignition delay time should be longer than $0.06s$. Particle velocity in different transversal areas indicated that particles tend to accumulate in the middle of the tube during dispersion, and their velocity magnitude is significantly higher than other particles from the same cross-section.

Chapter 4

Single-particle model for coal dust

The main elements in coal are carbon, hydrogen and oxygen. In addition, there exists a little nitrogen, sulfur and other elements [101]. The complex procedure of physical and chemical changes in the continuously heated up procedure of coal in inert gas atmospheric (air isolation) is called coal pyrolysis. In this procedure, the released gas includes pyrolysis water, CO_2, CO, paraffin hydrocarbons, aromatic hydrocarbon and some heterocyclic compounds. The solid residuals in the end become semi-coke and coke.

As the particle studied in dust explosion is relatively small, the diffusion effect inside of the particle can be neglected. Moreover, the pyrolysis is controlled by kinetics [81, 102]. As temperature increases, particle size decreases. When simulating the combustion of small particles, the primary objectives are to understand the precipitation process, determine the yield of each product, and observe how the products change based on temperature and heating rate.
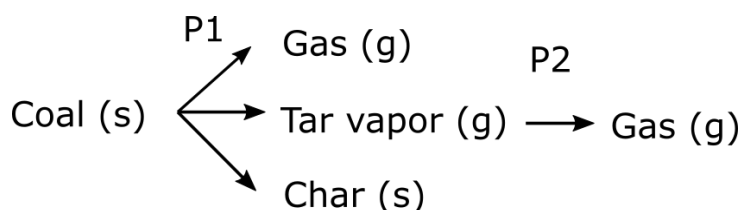
Figure 4.1: Devolatilization scheme for coal. P1 and P2 are the pyrolysis stages. g - gas, s - solid.

The schematic of the pyrolysis model is presented in Figure 4.1. Coal and char are solid-phase components, while tar and gas are gaseous byproducts of pyrolysis. When coal undergoes pyrolysis, it produces three main components: char, which is rich in carbon, tar, which is a condensable macromolecular substance, and gas, which is non-condensable. As the temperature increases, the rate of conversion during the second stage of pyrolysis

increases. During this process, the pyrolysis tar breaks down into char and pyrolysis gases [103].

Besides the pyrolysis reactions, homogeneous reactions of gases and heterogeneous reactions with the pyrolysis char occur. The homogeneous gas reactions outside the particle interacting with the oxygen form a dust deflagration flame, which provides most of the energy to heat the particles further. However, the pyrolysis gases and the oxygen have to be mixed on a molecular level. The turbulence is decisive for both the mixing and the heat transport through micro-vortices.
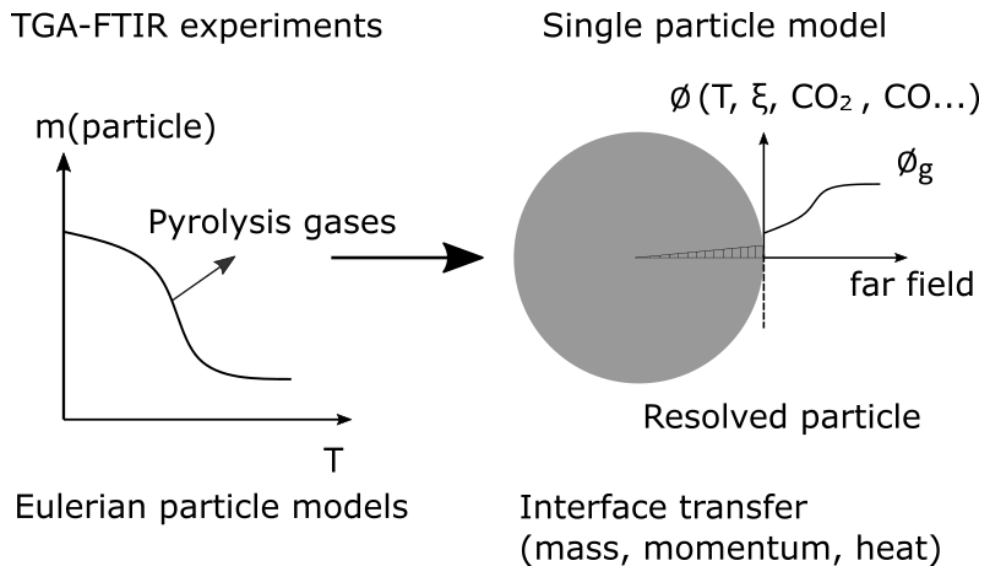
Figure 4.2: The method of single-particle model.

In this chapter, the single-particle model considers the devolatilization of coal particles, gas evolution and ambient temperature. The scheme of the method is in Figure 4.2. The thermodynamic characteristics of coal dust were determined through Thermogravimetric Analysis-Fourier Transform Infrared Spectroscopy (TGA-FITR) experiments. A single-particle model was developed using kinetic models and interface transfer properties, and the solver reactingFOAM in OpenFOAM was modified to incorporate these new models. A resolved particle geometry was then constructed, and simulations were performed with varying temperature boundary conditions. This chapter is published in paper [104].

4.1 TGA-FTIR experiments

TGA is a thermal analysis method that measures changes in sample weight in a controlled thermal environment as a function of temperature or time. This method can obtain

the thermophysical information of the sample such as phase transitions, absorption, adsorption and desorption, and chemical phenomena, including chemisorptions, thermal decomposition, and solid-gas reactions. The TG curve describes the relationship between the mass of the sample and temperature (T). It has a "step" shape. The relation between the rate of mass change dm/dt (mass loss rate) and temperature is the differential thermal gravimetric (DTG) curve. It shows with peaks, giving the change degree of mass with temperature. The number of peaks in DTG curve is in corresponds to the "steps" in TG curve [105].

FTIR is an effective analytical technique for quickly identifying the "chemical family" of a substance. TGA-FTIR combines the strength of TGA with FTIR for materials characterization and off-gas profiling. It accurately records the mass loss as a sample is heated up in the TGA analyzer and identifies the released molecular species resulting from the corresponding mass loss by injecting the released molecular species through a long optical path in the gas chamber of FTIR instrument [106, 107]. According to Beer Lambert's law, the gas concentration is obtained by using the molar absorption coefficient. The molar absorption coefficient of the evolved gases from coal is summarised in Table 4.2.

$$A = \epsilon \, c \, l \tag{4.1}$$

where A is absorbance. ϵ is molar absorption coefficient, $L/(mol \cdot cm)$. c is molar concentration, mol/m^3. l is the path length,cm. The coefficient is a characteristic constant when the temperature and wavenumber is fixed. It describes the ability of the species to absorb light in a specific wavelength [108].

4.1.1 Sample preparation and characterization

Table 4.1: Coal characterizations

Sample	Proximate Analysis/Mass %, Dry Basis				Ultimate Analysis/Mass %, Dry Basis			
	Moisture	Volatile	Ash	Fixed Carbon	C	H	N	O
Western coal	0	35.33	10.82	53.85	73.9	4.87	1.47	10.62

The TGA-FTIR tests were carried out at the chair of Process Engineering of Industrial Environmental Protection, Montanuniversität Leoben [109]. To reduce the inner particle effects , the smallest size ranges, $25 - 32 \mu m$ was used. The proximate and ultimate analysis results of the coal sample are listed in Table 4.1. The ultimate analysis was carried out as a reference of the volatile gas. Elements of mineral composition such

as S, Ca, Al, etc. [110] were not in our interest and were not included. The particle size distribution on the coal particles was tested by laser diffraction analyzer HELOS (H4439) & QUIXEL at the Chair of Process Technology and Industrial Environmental Protection (VTiU), Montanuniversität Leoben and the result is shown in Figure 4.3. The particle distribution values are $d_p(10) = 3.59\mu m$, $d_p(50) = 14.8\mu m$, $d_p(90) = 32.47\mu m$. The attached smaller particles are from the sieving method and remained due to their light weight. Figure 4.4 shows the Scanning Electron Microscope (SEM) images of the coal sample. Two size ranges $125 - 250\mu m$ and $20 - 32\mu m$ are tested and presented. The particle size varies within one size range and the shape is irregular. After breaking up, cutting faces can be identified in the $20 - 32\mu m$ particles.
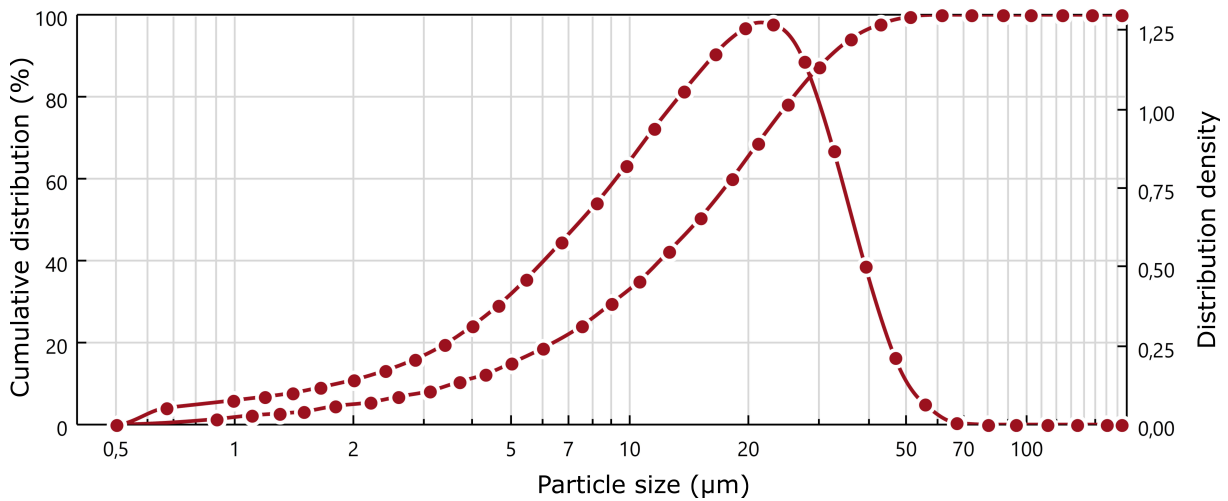
Figure 4.3: Particle size distribution of pulverized coal sample.

(a) 125 - 250 µm (b) 125 - 250 µm (c) 20 - 32 µm (d) 20 - 32 µm
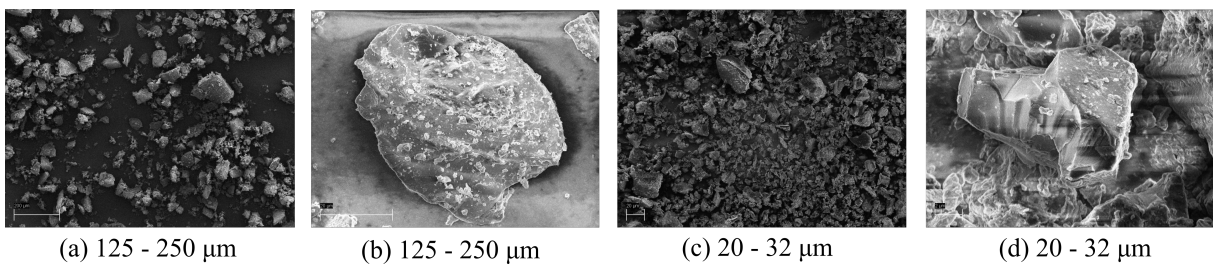
Figure 4.4: SEM micrographs of $125 - 250\mu m$ and $20 - 32\mu m$ coal particles.

In the test, $10 \pm 1mg$ coal dust was heated up from $30°C$ to $1100°C$. Two heating rates $15K/min$ and $30K/min$ were used. Inert gas N_2 was used as the shielding gas. It has a constant flow of $20mL/min$ to ensure the inert atmosphere in the thermal gravimetric analyzer and to take the gas products to the FITR analyzer pool.

The evolved gas was measured using the complementary FTIR spectrometer. The measurable spectral range is $4000 - 400cm^{-1}$. In the test, the evolved gas is transferred

through a 200°C constant temperature pipeline to the FTIR analyzer gas pool, which is real-time monitoring in the analysis of the components and characters of pyrolysis products.

4.1.2 TGA experiments

The mass change over temperature is the TG curve. The first derivative of mass change on time (dm/dt) is the weight loss rate curve, i.e., DTG curve. From these curves, the information of reacting stages is obtained, and the data will be used for calculating the kinetic parameters. The TG and DTG curves of the coal sample at different heating rates are shown in Figure 4.5 and Figure 4.6 respectively.
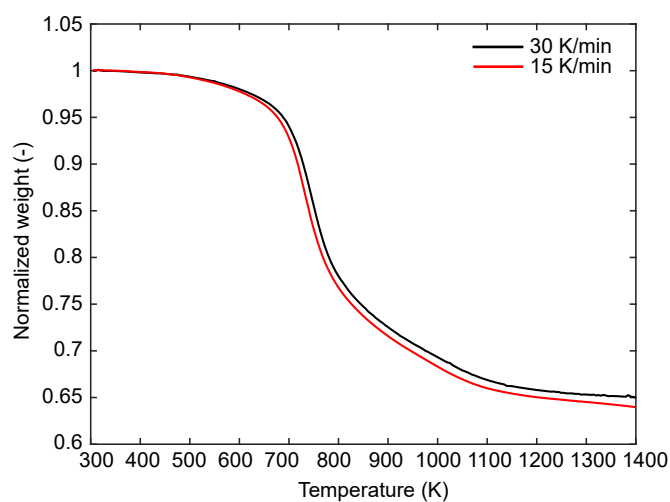
Figure 4.5: TGA data of coal sample at two heating rates.
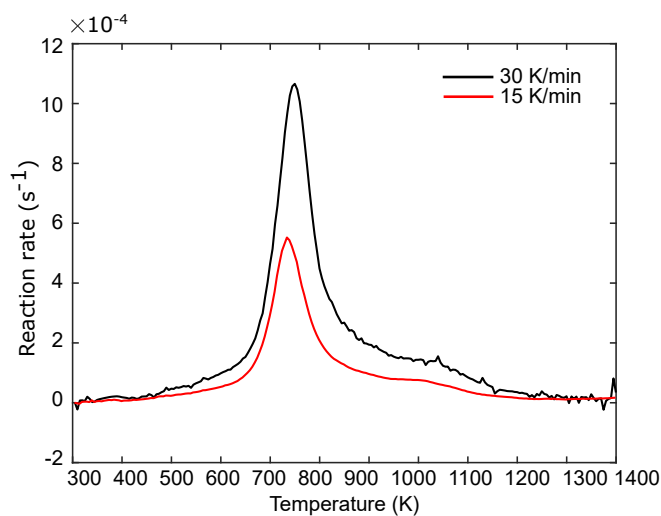
Figure 4.6: DTG data of coal sample at two heating rates.

56

In Figure 4.5, the mass of coal samples was normalized by their initial value. This will be beneficial for implementing the kinetic model into further calculations. The two curves for coal samples that experienced different heating rates have similar mass loss patterns. The gap between them grows over time. Three stages can be observed from the decomposition curve.

The first mass loss between $300K$ and $600K$ is approximately 2%. The pyrolysis begins gradually from this stage. The second stage is between $600K$ and $1200K$, in which the main decomposition occurs. In this stage, the coal mass decreases remarkably due to active pyrolysis. In the meantime, volatile gases, CO, CO_2, CH_4 and light hydrocarbons are released and measured in the FTIR analyzer. The mass of coal decreased around 30% of the total weight in this stage. The total mass loss of the two experiments are 34.98% ($\beta = 30K/min$) and 36.03% ($\beta = 15K/min$). The test of $\beta = 15K/min$ has a longer heat time than the test of $\beta = 30K/min$. Because of the longer thermal decomposition time, the final mass of the coal sample undergoes $15K/min$ is lower than that of $30K/min$.

The DTG curves from two heating rates (Figure 4.6) present a similar pattern. In each heating rate, two obvious reaction peaks can be observed. The highest peaks in each curve occur at between $700 - 800K$. It corresponds to the main decomposition stage. In this stage, the coal undergoes active decomposition, rapidly releasing pyrolysis gases and tar. In the curve of $\beta = 30K/min$, the first peak has a reaction rate of $10.66 \times 10^{-4}\ s^{-1}$ at $749.7K$; In the curve of $\beta = 15K/min$, the first peak has a reaction rate of $5.524 \times 10^{-4}\ s^{-1}$ at $733.8K$.
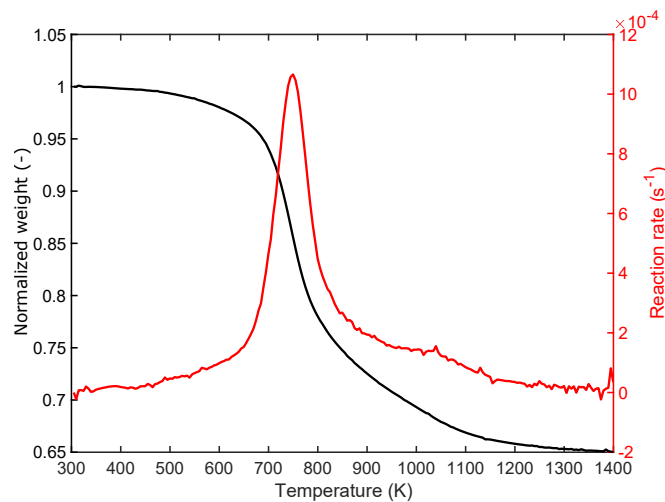
Figure 4.7: TG and DTG data of coal sample at $30K/min$.

The second peaks in the DTG occur between $900 - 1100K$. In this stage, the reaction rate values of the peaks are distinctly lower than the first peaks. Their highest reaction

rates are $1.411 \times 10^{-4}\ s^{-1}$ at $1050K$ ($\beta = 30K/min$) and $0.7656 \times 10^{-4}\ s^{-1}$ at $1005K$ ($\beta = 15K/min$). The mass loss of the coal in this stage is from the second pyrolysis of the gaseous tar; the curve shifts to higher temperature ranges when the heating rate increases. The peak becomes wider because of the heat and mass transfer limitations.

Figure 4.7 illustrates the TG and DTG curves from the experiment of $30K/min$. The second reaction rate is not able to shape a "step" in the TG curve and can only be observed in the DTG curve. At $600K$, the reaction rate gradually increases when the mass of the coal decreases remarkably. Around $900K$, the first reaction finishes and the second reaction starts. The second reaction is less vigorous and lasts for a longer temperature range.

Due to the complex reaction of the coal, the kinetics of the coal decomposition can not be described by one reaction. Instead of describing the kinetics of coal decomposition, one approach is to use the production of evolved gases. By studying the reaction of each gas species individually, the kinetic parameters are obtained. This method gives the opportunity to divide the total kinetics of the coal into several reactions of the pyrolysis gases. The sum of the produced gases is equal to the total mass loss of the coal.

4.1.3 Evolved gas analysis

FTIR examined the gaseous products of TG in order to investigate the kinetics further. In the test, mid-infrared light was used to detect the gas molecules. Molecules and functional groups can be identified at specific bands. Furthermore, a real-time measurement was applied to obtain the spectrogram in a three-dimensional way. Figure 4.8 is the spectrum of the evolved gases at $30K/min$.

The three dimensions are absorbance, temperature and wavenumber, respectively. The absorbance varies from 0 to 1, indicating the intensity of infrared light absorbed by the gases at a specific wavenumber. If the absorbance is 0, the infrared light is not absorbed. According to Beer Lambert's law (Euqation 4.1), the gas concentration is proportional to the absorbance. Therefore, the absorbance can reflect the concentration of each gaseous products. Gaseous products can be identified with their wavenumber. The pyrolysis product of the coal that are detected are CO ($2190cm^{-1}$),CO_2 ($2345cm^{-1}$),CH_4 ($1295cm^{-1}$ and $2810cm^{-1}$), and light carbohydrates ($1450cm^{-1}$). We assume the the light carbohydrates as C_2H_4 and also to compensate the H_2 gas. Molecules such as CH_4 absorbs both bands at $1295cm^{-1}$ and $2810cm^{-1}$, showing two peaks in the spectrum. Each evolved gas is indicated by an absorbance peak in the spectrum graphic. Initially, the rate of gas release is low. However, CO_2 is observed to be released slightly earlier than the other

gases at the beginning of the experiment. As the temperature increases, the release of CO_2 gradually increases.The intensive gas release is between $800K$ and $1100K$, which is in correspondence to the active mass loss period of the coal. For CH_4 and C_2H_4, they have relatively small ranges. The concentration of CO_2 reduces after the intensive gas release period and then increases remarkably as a result of tar pyrolysis. At the end of the measurement, the continuous temperature rise enables char decomposition and gas production. However, in the study of dust explosion, the coal dust is not fully combusted, which means that we only need to consider the pyrolysis stage of the coal [111].
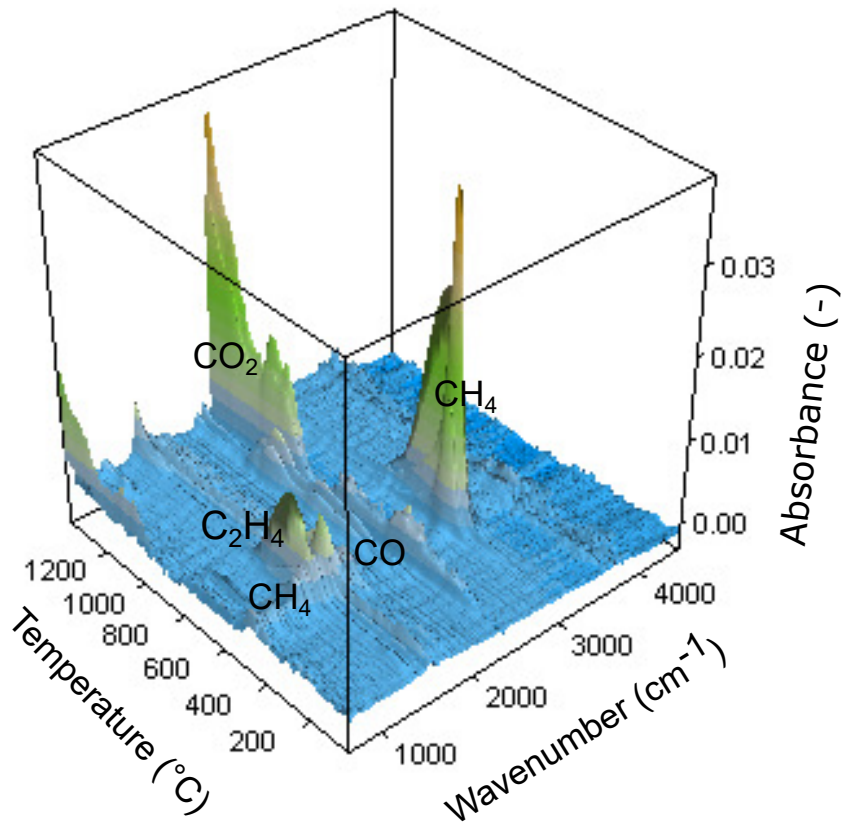
Figure 4.8: FTIR three-dimensional spectrum of evolved gas at $30K/min$ [109]. .

The molar absorption coefficients of evolved gases (Table 4.2) are used to calculate their concentration. The concentration of each gas is calculated and plotted in Figure 4.9. It can be observed that the C_2H_4 and the CO_2 gases have higher concentrations. There is a high release amount of CO and CO_2 after $1200K$ due to the decomposition of the char, which will not be discussed in this study. The production of C_2H_4 and CH_4 are located at the active decomposition temperature range. In this range, the concentration of CO_2 is on the same level as C_2H_4, thus leading to the fast mass loss of the coal. Around $1050K$, the high concentrations of CO_2 and C_2H_4 are the results of the second reaction due to

the tar decomposition.

Table 4.2: Molar abosrption coefficient of evolved gases [112].

CO $L/mol \cdot cm$	CO$_2$ $L/mol \cdot cm$	CH$_4$ $L/mol \cdot cm$	C$_2$H$_4$ $L/mol \cdot cm$
1146	945	784	612
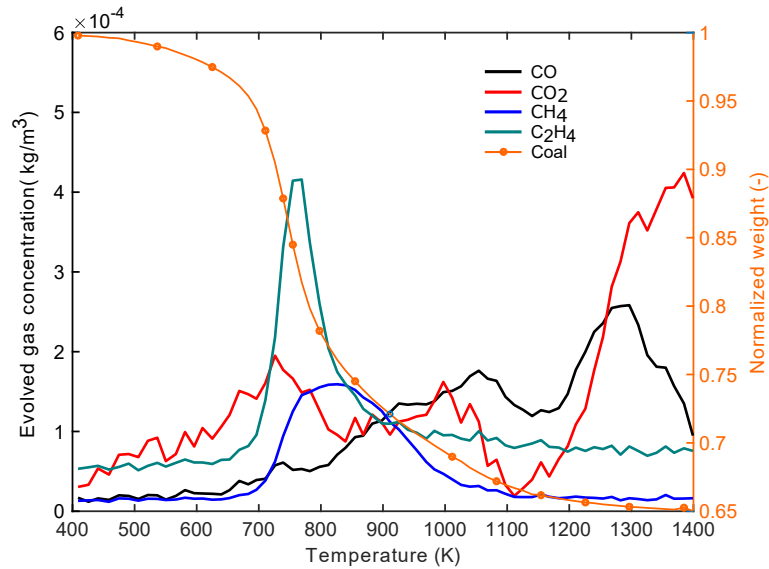
Figure 4.9: Evolved gas concentration compares with normalized coal mass loss.
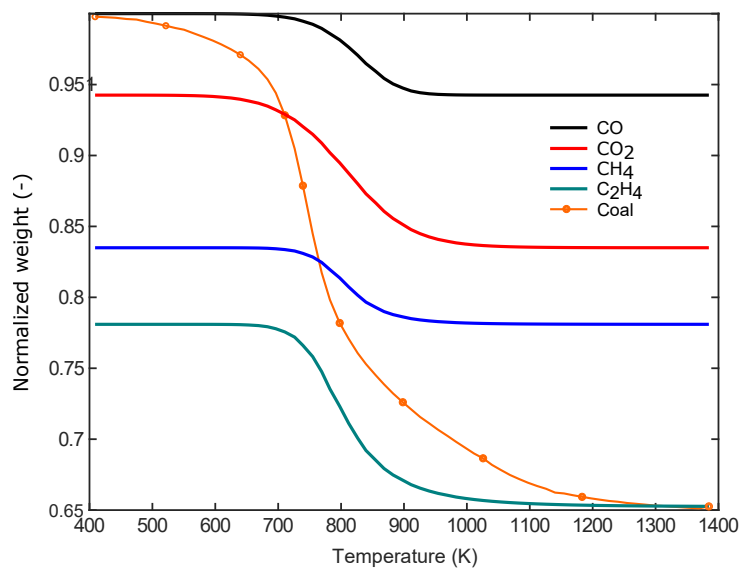
Figure 4.10: Coal mass loss from evolved gases.

By rearranging the concentration, the mass loss due to each evolved gas is plotted in

a sequence to compare with the coal mass loss, as shown in Figure 4.10. For example, the final value of CO at $1400K$ is the start value of CO_2 at $400K$. Therefore, the final value of the last gas, C_2H_4, shows the residual coal mass. CO_2 takes the highest mass fraction among the gas products. The start point of production of CO and CO_2 are earlier, which is around $650K$. Each gas will be analyzed to obtain its kinetic data in the following section.

4.1.4 Evolved gas kinetics

For a mass-related pyrolysis speed $r_j^{pyro}(kg/m^3 \cdot s)$ of a gas component i from a single, independent parallel reaction j applies:

$$r_j^{pyro} = A_j \, exp(-\frac{E_j}{RT})(V_{max,j} - V_j)^{n_j} \qquad j = 1, ..., n_{pyro} \tag{4.2}$$

where $V_{max,j}$ is the maximum mass fraction of the pyrolysis gas determined experimentally. For the calculation of the formation rates r_j^{pyro} of the individual independent, parallel pyrolysis reactions (n_{pyro}) were considered at a certain point in time t. A mass fraction of V_j from solid is already volatilized to this point in time. These solid fractions that are released by the decomposition reactions of the solid will be represented by the evolved-gas mass fractions. The total formation rate of one gas component i results from the sum of the individual independent parallel reactions:

$$r_i^{pyro} = \sum_{j=1} r_j^{pyro} \qquad i = 1, ..., n_{gas} \tag{4.3}$$

In order to implement the kinetic data into simulation models, the kinetics of each gas evolution is fitted by using parallel gas reaction kinetic equations. Take the gas specie CH_4 as an example, the reaction rate is calculated out of the gas concentration:

$$r_{CH_4} = A_1 exp(-\frac{E_1}{RT})(V_{max,1} - V_1)^{n_1} \tag{4.4}$$

Take logarithmic on both sides of the Equation 4.3 for CH_4:

$$lnr_{CH_4} = lnA_1 + (-\frac{E_1}{RT}) + n_1 * (V_{max,1} - V_1) \tag{4.5}$$

Due to two reaction peaks being observed in the reaction rate of CO_2 (Figure 4.9), two parallel reaction models were used in MATLAB to calculate its kinetics. The fitting curves are shown in Figure 4.11, compared with the experiment result. Compared to the first peak, the second one is not distinct but essential for describing the tar decomposing

stage. The reaction stages are not separated into primary and secondary pyrolysis stages in this method. This simplification will reduce the computation time when considering high solid loading combustions. The total mass over the temperature range is plotted in Figure 4.11b. The difference between the model and experiment result is about 2%. The models of other gas species are in Figure 4.12-4.14. The gas release over time are in good agreement with the experimental data. Therefore, the model can predict the CO_2 evolve profile. The kinetic data of the coal profiled using evolved gases determined experimentally is shown in Table 4.3, where $T_b = E_j/R$.

(a) Reaction rate over temperature.

(b) Mass increase over temperature.
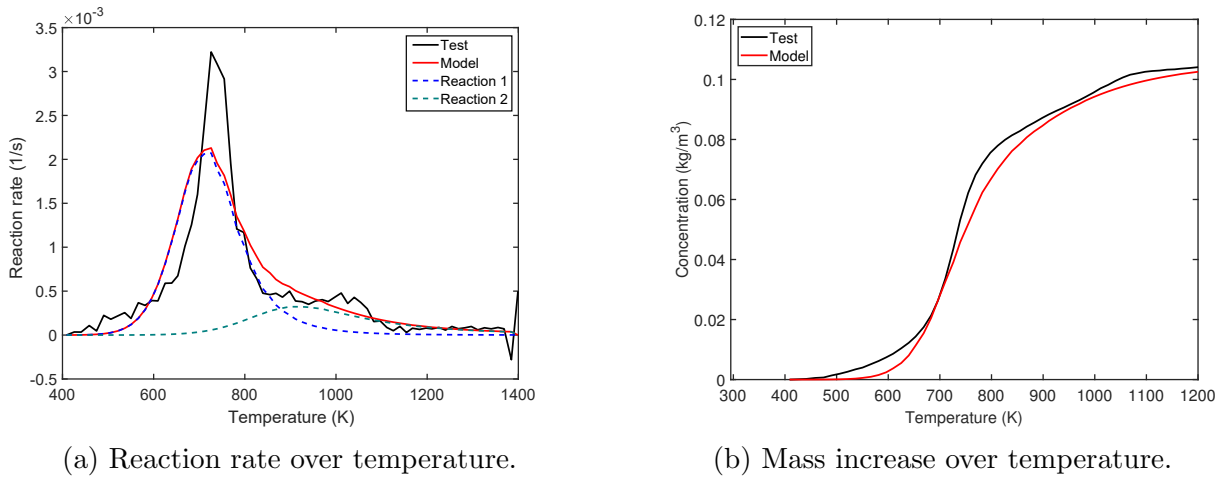
Figure 4.11: Comparison of evolved gas reaction model with the experimental result:CO_2.

(a) Reaction rate over temperature.

(b) Mass increase over temperature.
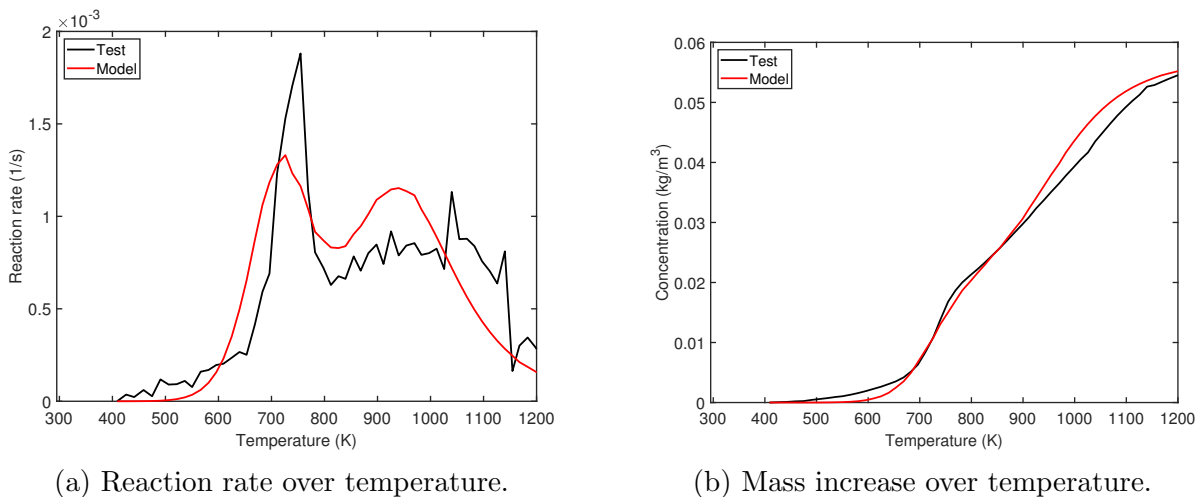
Figure 4.12: Comparison of evolved gas reaction model with the experimental result:CO.

In the modeling of the formation of a single gas component (e.g., CO, CO_2), up to two independent parallel reactions j were used in the calculations for coal pyrolysis. However, if necessary, more independent parallel reactions can be used to describe the

formation of a single pyrolysis gas component.

Table 4.3: Pyrolysis kinetic data of coal.

Gas	$A(1/s)$	T_b (K)	$V_{max}(kg/kg)$	Order, n (-)
CO	1.60E+08	14000	0.9778	2
	7.00E+03	10500	0.9426	2
CO_2	9.00E+08	15000	0.86	2.4
	8.00E+03	10000	0.8353	2
CH_4	1.00E+04	9000	0.781	2
C_2H_4	1.00E+06	13000	0.6523	1.6
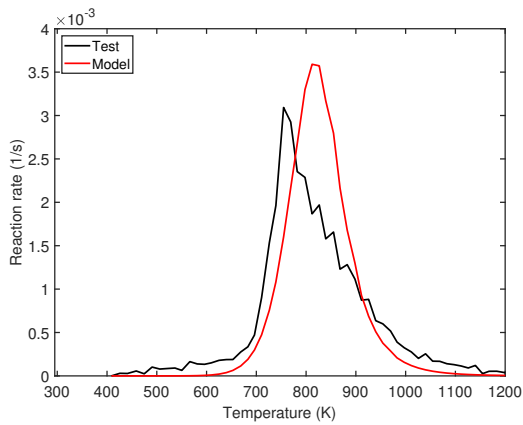
(a) Reaction rate over temperature.
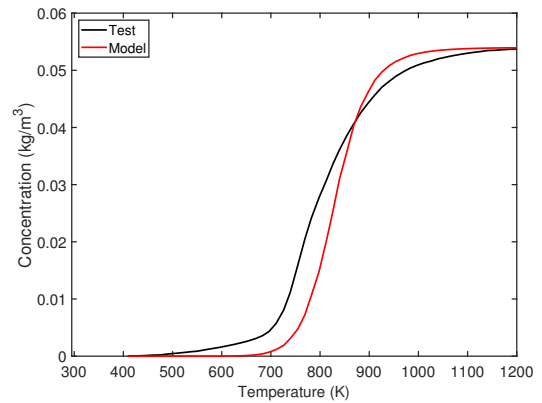
(b) Mass increase over temperature.

Figure 4.13: Comparison of evolved gas reaction model with the experimental result:CH_4.
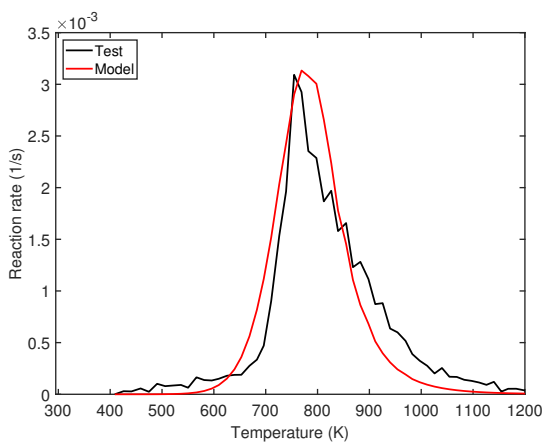
(a) Reaction rate over temperature.
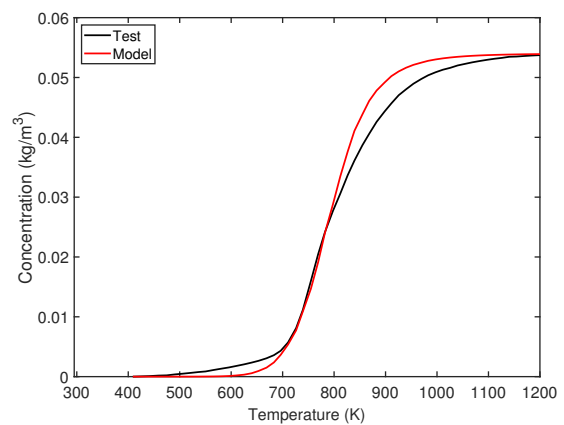
(b) Mass increase over temperature.

Figure 4.14: Comparison of evolved gas reaction model with the experimental result:C_2H_4.

4.2 Model implementation

In this chapter, the single-particle model will be set up using the TGA data for the coal particles. The SEM picture of one coal particle shows the porous channel on the surface with a width of around $1mm$. Therefore, the steps for setting up the single-particle model start from implementing the physical property of a single coal particle and then applying the kinetic of particle decomposition into the simulation. The modification of the solver is based on reactingFoam. It is a transient solver for the turbulent flow of compressible fluids, including the chemical reactions used for dust combustion. The already existing solver rhoPorousSimpleFoam is not used because the diameter of the pores is fixed in the solver and does not include chemical properties for further reaction modeling.

4.2.1 Transport effect

The heterogeneous reactions and phase transitions in coal particles will lead to a mass fraction change in species. Furthermore, due to the combustion, the enthalpy in the gas phase is increased and therefore the temperature increases. The temperature increase results in pressure increase or decrease in the flow, thus creating a convective flow in the gas phase inside the particle. To model this flow, an E-E approach was used for the gas phase. The pressure drop is then derived by considering the pore diameter and the void volume.
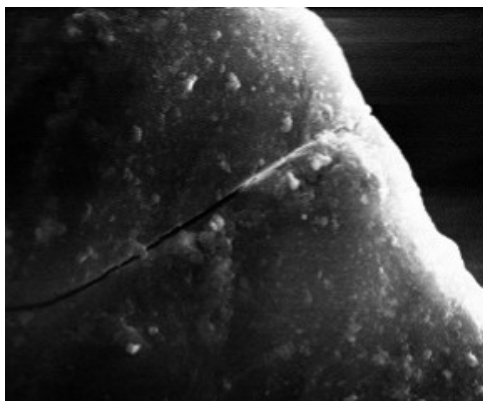
Figure 4.15: SEM picture of coal particle.

The porous structure of the coal particle is assumed as a parallel channel (Figure 4.15). The larminar Navier-Stokes equation for a 2D flow in the channel shown in Figure 4.16 can be written in x coordinates as,

$$u\frac{\partial U}{\partial x} + v\frac{\partial U}{\partial y} - \nu\nabla^2 U = -\frac{1}{\rho}\frac{\partial p}{\partial x} \tag{4.6}$$

where, u,v are the velocities on x, y coordinates, m/s, ν is the kinematic viscosity of the fluid, m^2/s, ρ is the density of the fluid, kg/m^3.
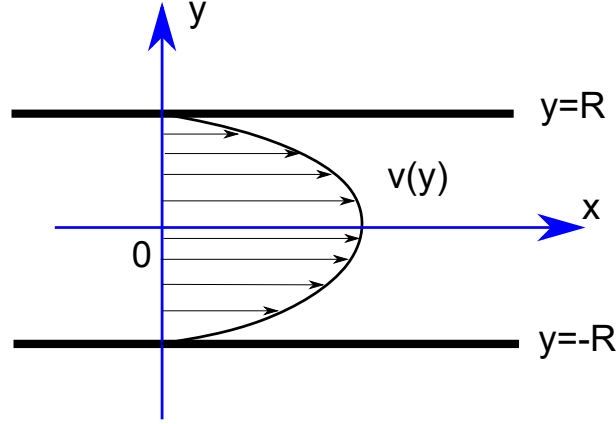
Figure 4.16: Velocity distribution of incompressible flow in a 2D channel.

The flow is assumed on x direction, so $v = 0$. For a steady state, u only changes along the y coordinate, therefore, $dU/dx = 0$. First two terms in Equation 4.6 will be eliminated. The third term of Equation 4.6 can be written as,

$$\nu\nabla^2 U = \nu(\frac{d^2U}{dx^2} + \frac{d^2U}{dy^2})$$ (4.7)

Similarly, $d^2U/dx^2 = 0$, and Equation 4.6 will finally be formed in,

$$\mu\frac{d^2U}{dy^2} = \frac{\partial p}{\partial x}$$ (4.8)

where μ is dynamic viscosity, $\mu = \rho\nu$, $N \cdot s/m^2$.

The boundary condition of the flow on the two sides of the wall are $U(-R) = 0$ and $U(R) = 0$. At position of $(0, 0)$, there is $dU/dy = 0$. Using these values, the equation can be integrated and result as,

$$-\frac{\partial p}{\partial x} = \mu\overline{U} \cdot \frac{12}{D^2}$$ (4.9)

This equation gives the relationship of the pressure drop on x-direction, the diameter of the channel, D (m) and the average velocity on the direction of the channel.

To include the porous structure of the particle, the porosity coefficient ξ is introduced into the conservative Equation 4.10. $\xi = 1$ represents a hollow domain. $\xi = 0$ represents a solid domain. The conservative momentum equation is implemented in 3D to perform spatial observations within the model. The gas volume and the hydraulic pore diameter D_{pore} are stored as "volScalarFields" because their value changes are due to chemical reactions.

$$\frac{\xi \rho_g U}{\partial t} + \nabla \cdot (\xi \rho_g UU) - \nabla \cdot (\xi \tau_g) + \xi \mu \frac{12U}{D_{pore}^2} = -\xi \nabla p + \xi \rho_g g + S_U \qquad (4.10)$$

A 2D geometry was created to evaluate the model as shown in Figure 4.17. The porosity ξ is set as 0.5 in the middle block of the geometry, meaning this is a porous structured material. The other parts have a porosity of 1. The boundary conditions for the bottom and upper walls are set as "symmetry". A flow with $2m/s$ velocity comes from the inlet (left side) of the geometry.

Figure 4.17: 2D testing geometry for testing porosity model.

The data of pressure is illustrated in Figure 4.18. Inside the porous media, the ambient pressure decreases gradually because half of the media is empty. Therefore, the modified solver for porous media can predict the flow field.

The continuity equation of the gas phase is relatively simple. Besides the transient and convective transportation terms, it contains source terms from heterogeneous reactions.

$$\frac{\partial \xi \rho_g \overrightarrow{U_g}}{\partial t} + \nabla \cdot (\xi \rho_g \overrightarrow{U_g}) = S_m \qquad (4.11)$$

Besides the transient and convective terms, the S_m are the inter-phase mass transfer terms from the solid phase due to heterogeneous reactions at the gas-solid interface or from physical processes such as evaporation. For our kinetic model, $\sum_{n=1}^{N} S_{gn} = 1$. In which N is the total number of species. In the solid phase, no convective transport occurs; there is only a transient term from the pyrolysis for each species. Thereby, X is the mass concentration of the substance i in the computation cell. This will be implemented in the
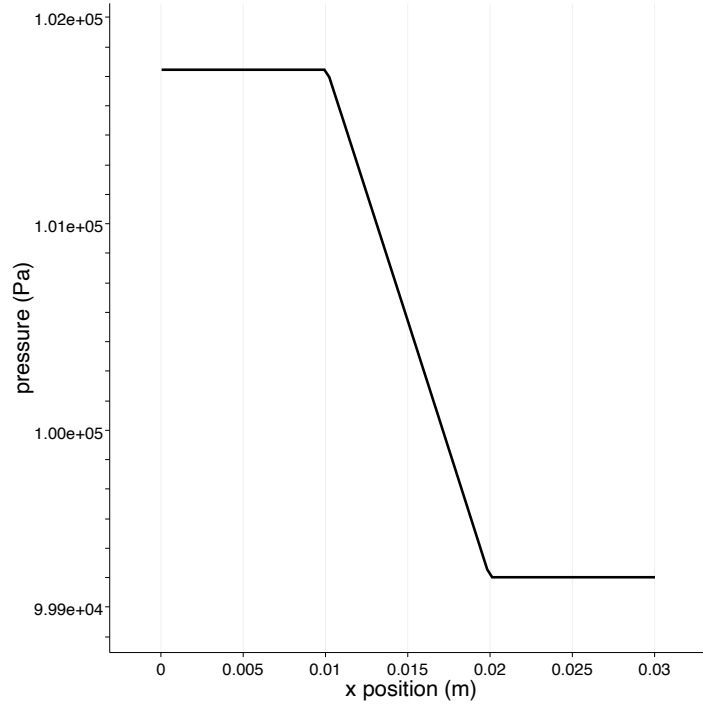
Figure 4.18: Pressure field along the geometry.

next steps.

$$\frac{X_i}{\partial t} = -S_m \tag{4.12}$$

4.2.2 Conservation of energy

The energy conservation equation of the gas phase includes the time derivation of the volume-specific heat, the convective transport, the diffusive transport, the energy transfer to the gas phase and the source term for the energy from the particle combustion. This source term is derived from the combustion model via the source term Q and the enthalpy of combustion H.

$$\frac{\partial(\xi\rho_g(h+K))}{\partial t} + \nabla(\xi\rho_g U(h+K)) - \nabla \cdot (\xi\alpha_{eff}\nabla h) = S_s + S_h \tag{4.13}$$

The effective thermal diffusivity of the gas phase is determined with the help of the thermophysical model and the thermal diffusivity of the gas phase α_g is used.

In order to record the energy transport through the particle, a separate energy conservation equation is required for each phase. The energy conservation of the particle phase includes, in addition to the temporal dissipation of the volume specific heat, only the convective transport and the energy exchange to the gas phase. The energy

transport through the diffusive movement of the particles is in the flow field through the granular pressure p_s, the collision viscosity μ_{co} and the kinetic particle viscosity $\mu_{k,s}$ of the conservation of momentum equation and is mapped via the velocity vector v.

$$\frac{\partial(1-\xi)\rho_s C_{ps} T_s}{\partial t} - \nabla \cdot ((1-\xi)\lambda_s \nabla T_s) = S_g + S_h \tag{4.14}$$

$$S_g = \xi A_V h(T_g - T_s) \tag{4.15}$$

$$A_V = \frac{A}{V} = \frac{2}{D_{pore}} \tag{4.16}$$

The volume-specific heat flow between the two phases is determined by the volume-specific particle surface A_V and the average heat transfer coefficient h. The heat transfer coefficient is calculated using the particle Reynolds number through the similarity relationship described by Ranz-Marshall [113].

A sensitivity test was conducted on the volume-specific particle surface A_V using various values, and the results were compared in Figure 4.19-4.20. The temperature difference between the surface and core phases was calculated and plotted for each value. The initial heating time showed significant variation in surface temperature for different A_V values, with the least fluctuation observed for $2 \times 10^5 m^{-1}$. This value also exhibited stable temperature prediction in the core throughout the process. As a result, $2 \times 10^5 m^{-1}$ was chosen for use in subsequent simulations.
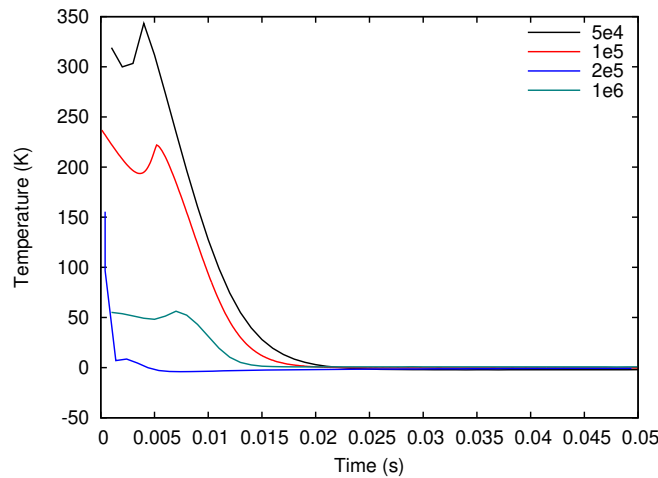
Figure 4.19: Temperature difference between solid and fluid at the surface of particle.
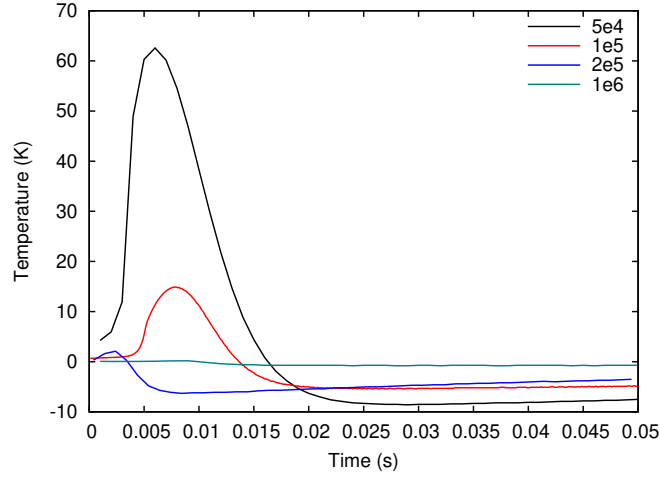
Figure 4.20: Temperature difference between solid and fluid at the core of the particle.

Heat transfer between two phases

In the single-particle model, the pore size increase when the coal is decomposed further. The porosity should be included inside the heat transport between the two phases. The heat transfer coefficient (Equation 4.15) has a form of:

$$h = Nu * \frac{\lambda_g}{d_p} \tag{4.17}$$

where the Nusselt number is used based on a study that considered the porosity of the particles [114].

$$Nu = (4.31 - 12.71\xi + 9.81\xi^2) \cdot (1 + 0.8Re^{0.6}Pr^{1/3}) \tag{4.18}$$

4.2.3   Heterogeneous and homogeneous reactions

The evolved gas produced in the pyrolysis is assumed to become gas phase immediately. The reaction rate of each gas specie is obtained by TGA-FTIR in Chapter 4.1.3. The reaction rate follows:

$$r_j^{pyro} = A_j \, exp(-\frac{E_j}{RT})(V_{max,j} - V_j)^{n_j} \qquad j = 1, ..., n_{pyro} \tag{4.19}$$

Next step the combustion in the media will also be tested. To fulfill heterogeneous reactions, the volatile from coal are created as volume scalars in the *createFields.H* file. Four volatile gases are assumed according to the coal kinetics data: CO, CO_2, CH_4, and C_2H_4.

The reaction rates for homogeneous gas uses a simplified chemistry approach from

[115]. This approach uses an optimized global scheme that is approved to be well suited for CFD calculation. The calculations are based on the Arrhenius rate. In Table 4.4, it lists the four reactions as well as the pre-exponential factor A, activation energy E (cal/mol) and temperature exponent β.

Table 4.4: Pre-exponential factor A, activation energy E, and temperature exponent β for simplified reactions.

Reaction	A($1/s$)	E(cal/mol)	β (-)
$CH_4 + 0.5O_2 \longrightarrow CO + 2H_2$	9.6608e12	35000	0
$H_2 + 0.5O_2 \longleftrightarrow H_2O$	1.4284e18	40445	-1.1682
$CO + 0.5O_2 \longrightarrow CO_2$	5.5313e14	40735	0
$CO + H_2O \longrightarrow CO_2 + H_2$	1.7917e12	20845	0

The reaction rates for the four reactions are:

$$RR_1 = A_1 T^{\beta 1} exp(-\frac{E_1}{RT})[CH_4]^{0.37}[O_2]^{1.3991} \tag{4.20}$$

$$RR_2 = A_2 T^{\beta 2} exp(-\frac{E_2}{RT})[H_2]^{0.5}[O_2]^{1.1} \tag{4.21}$$

$$RR_3 = A_3 T^{\beta 3} exp(-\frac{E_3}{RT})[CO]^{1}[O_2]^{0.5} \tag{4.22}$$

$$RR_4 = A_4 T^{\beta 4} exp(-\frac{E_4}{RT})[CO]^{1}[H_2O]^{1} \tag{4.23}$$

In the context of this work, the heterogeneous reaction after pyrolysis is not considered because the reaction has a high demand for oxygen supply. In the study of dust explosion, the oxygen will be exhausted in the gas phase reaction.

4.2.4 Thermophysical data

Fluid properties

In OpenFOAM, the variation of fluid viscosity with temperature is modeled using the Sutherland relationship. This relationship relates the dynamic viscosity of a fluid to its temperature and is based on the kinetic theory of gases. The Sutherland relationship is expressed as:

$$\mu = \frac{\mu_0 T^{3/2}}{T + S} \tag{4.24}$$

where μ is the dynamic viscosity, μ_0 is a reference viscosity value, T is the temperature, S is the Sutherland temperature, and both S and μ_0 are constants.

In OpenFOAM, the Sutherland relationship is implemented with fixed values for S and μ_0. These values are typically determined from experimental data for the specific fluid being modeled.

By including the Sutherland relationship in the model, the variation of fluid viscosity with temperature can be accurately captured. This is particularly important for simulations involving high temperature gradients or large temperature ranges, where the viscosity can vary significantly.

Solid properties

From the experiment result of Tomeczek [116], the specific heat capacity c_s $(kJ/(kg \cdot K))$ of coal during pyrolysis is correlated by the polynomial:

$$c_s(T) = 1 \times 10^3 (1.13 + 3.58 \times 10^{-3}T + 2.28 \times 10^{-6}T^2 - 9.81 \times 10^{-9}T^3 + 4.63 \times 10^{-12}T^4) \quad (4.25)$$

in which T is in °C. The coefficients of Rydultowy coal are chosen for this study due to the similarity of the components of Rydultowy coal and the coal from this study.

The thermal conductivity for coal $\lambda_s(W/m \cdot K)$ is assumed to be a linear function of the temperature [117].

$$\lambda_s(T) = 0.23 \times (1 + 0.0033T) \quad (4.26)$$

where the temperature unit is K.

4.3 Model test

The coal particle is assumed to be in a sphere shape. To evaluate the models, a 1D geometry was created. As shown in Figure 4.21, the geometry is a 6° × 6° section of a sphere in 100 equidistant cells along the axis. On the axis, the positive z-direction points to the surface of the particle and the end of the other direction is the coal core. In this geometry, only two boundary conditions are needed. The first one is the particle surface, which is the outlet. The other surfaces on the geometry are "wedges", which represent the rotational symmetry of the geometry. The desired particle size can then be defined by scaling the finished computational grid.

The gas content at the initial condition inside of the fluid phase is 100% of N_2 and without O_2. The boundary condition on the surface of the particle is defined in Table 4.5, where the same ambient temperature as the TGA test is defined. The model test geometry size is with a $15\mu m$ radius, which is a representative size based on the sample used in the test. Two sets of solid properties such as solid heat conductivity are used, one of which are constants, and the other set are temperature-dependent profiles.
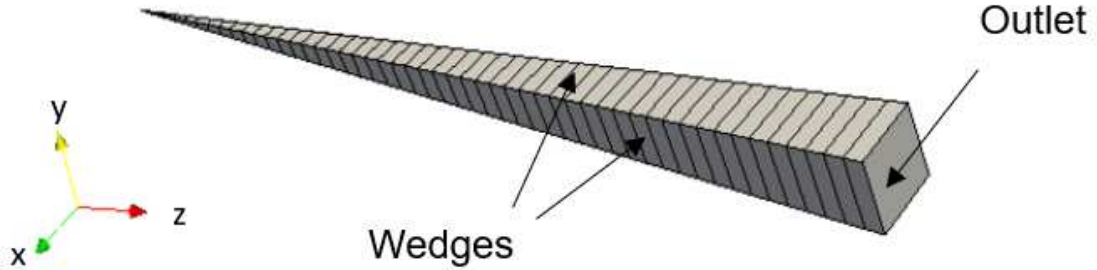
Figure 4.21: Illustration of the computational grid of the 1D coal particle geometry.

Table 4.5: Boundary conditions in single-particle model test.

BC	Value
Temperature (solid, fluid) (K)	300 ~1400 $(\beta = 30K/min)$
Velocity (m/s)	zeroGradient
Pressure (Pa)	100 000

Table 4.6: Particle properties in single-particle model test.

Parameter	Value
Radius (μm)	15
Density (solid) (kg/m^3)	1 007
Initial porosity (ξ) (μm)	0.02
Solid heat conductivity (λ) $(W/m \cdot K)$	3;Eq.(4.26)
Solid heat capacity $(C_{pSolid})(J/K)$	1550;Eq.(4.25)
Convective heat transfer coefficient $(h)(W/m^2K)$	5;Eq.(4.17-4.18)

4.3.1 Temperature profile

The temperature curves of solid and fluid phases on both of the particle surface and core positions are plotted in Figure 4.22. Some inconsistencies between the two phases
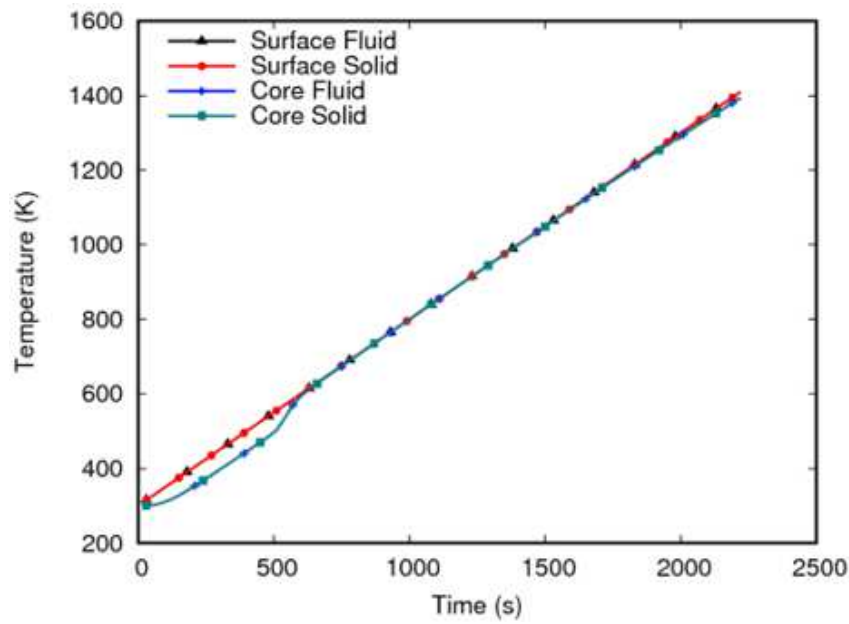
Figure 4.22: Temporal temperature profile of solid and fluid phases on particle surface and core positions during single particle heating at 30 K/min with variable material properties.

are observed until around $600s$. The temperature difference is now due to the positions within the particle. The core of the particle in both fluid and solid phases exhibits a lower temperature profile because of the low porosity during the early devolatilization stage, which causes heat transfer to take longer to reach the particle core.
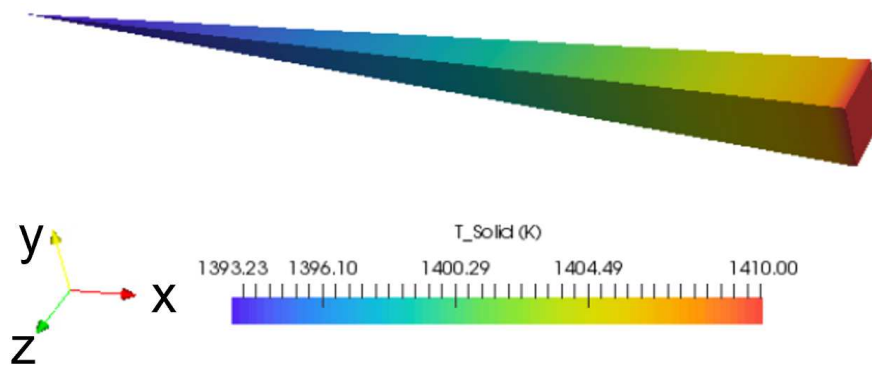
Figure 4.23: Coal solid phase temperature field at $t = 2220s$ and atmospheric temperature of $1410K$ during single particle heating at $30K/min$.

The temperature field, as well as velocity component on x-direction inside of the geometry, are displayed in Figure 4.23-4.25. The color legend bars of each figure have the range of the maximum and minimum values. At $2220s$, the boundary temperature is $1410K$, which equals to the particle surface temperature. The temperature field for solid and gas phases in the particle both have a minor temperature gradient inside of

73

the particle. The gas temperature is slightly higher than the solid temperature. The velocity component on x-direction is given in Figure 4.25. The contrast of the velocity values proofs that there exists convective gas flow inside of the particle. In our model, it properly predicts the escape of the pyrolysis gases.
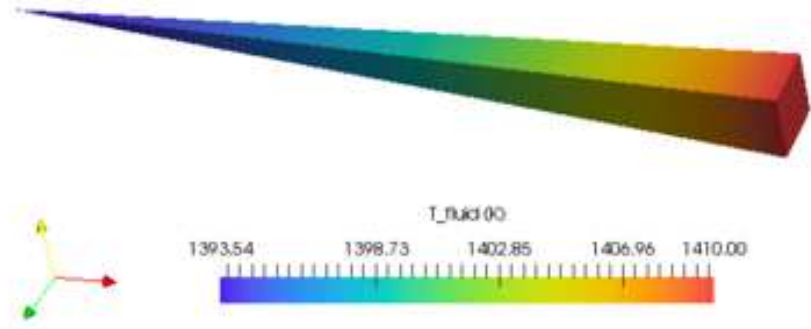
Figure 4.24: Coal fluid phase temperature field at $t = 2220s$ and atmospheric temperature of $1410K$ during single particle heating at $30K/min$.
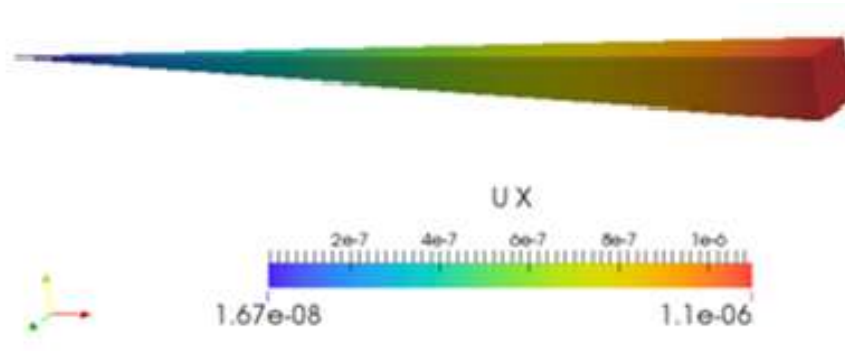
Figure 4.25: Velocity of fluid phase in the x-direction during coal single particle heating at $30K/min$, at $t = 2220s$ and atmospheric temperature of $1400K$.

4.3.2 Heterogeneous reaction result

The accuracy of the heterogeneous reaction model was verified by comparing it with experimental results. To ensure the correct prediction of the heterogeneous reaction, accurate temperature data was essential. In OpenFOAM, the gas species that escape from the solid phase are included in the gas phase and participate in mass and heat transfer phenomena through diffusion and convection. The mass of each gas species can be determined by integrating the pyrolysis gases released during the heterogeneous reactions.

The mass of the gas species that evolved out of the solid particle is compared with the FTIR tests in Figure 4.26. The models show different agreement level with the experiment results. In C_2H_4, the simulation has a late prediction and starts to react from $600K$. Similar effect is also found in CO and CO_2 but less intensive. Overall, the simulation result has acceptable deviation from the experiment and gives right prediction of the total amount of evolved gas mass. The coal mass decreases as a result of the gas evolve during the heterogeneous reactions.Therefore, the mass over time can be calculated by subtracting the volatile mass. In Figure 4.27, the total mass decrease in the coal is plotted.The late prediction of the gas evolve leads to a slower mass loss in the solid. The heterogeneous reactions are well predicted in the simulation and therefore the single-particle model can be used to predict particle behavior in high temperatures.
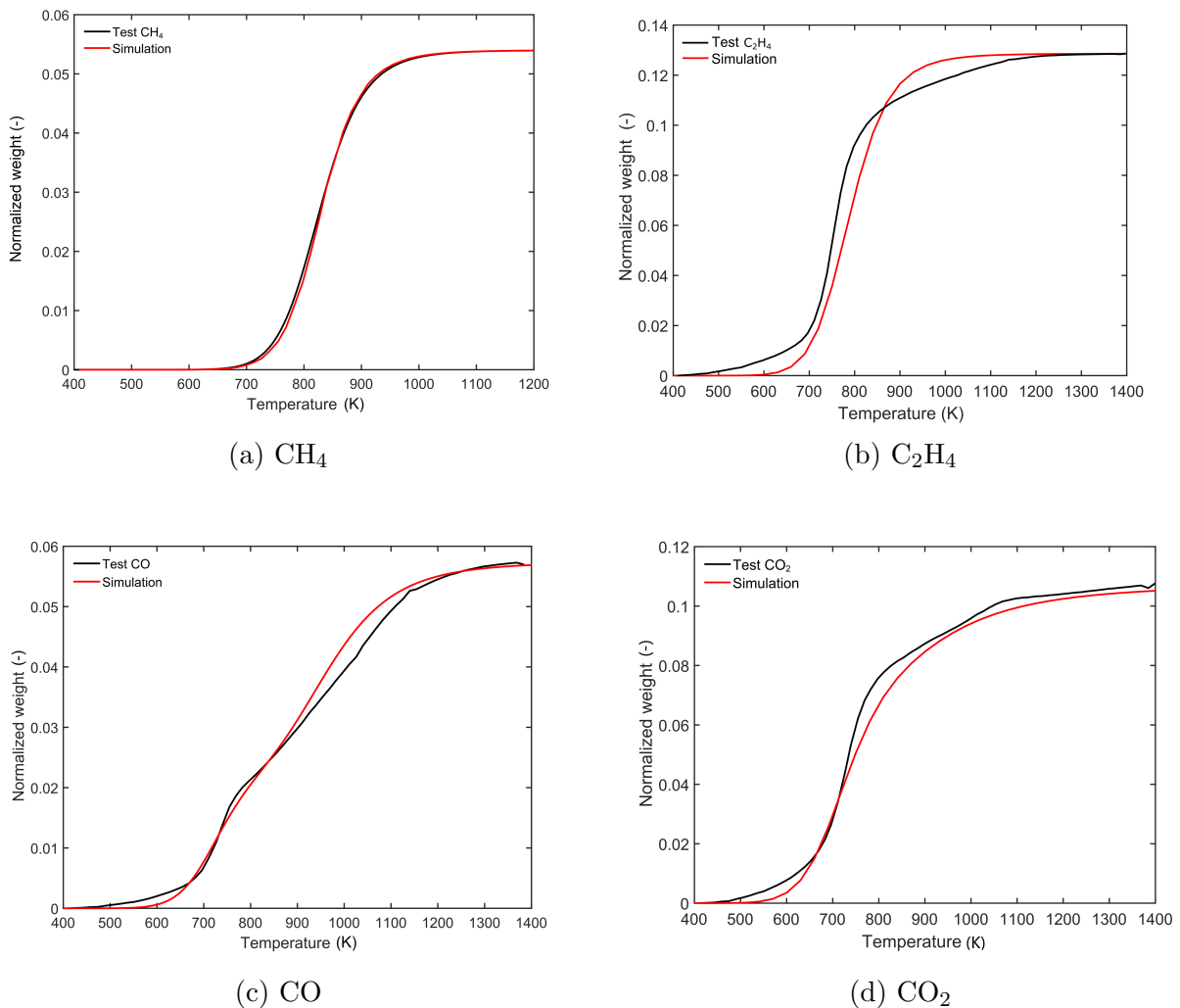
Figure 4.26: Comparison of simulated gas mass evolution at a heating rate of $30K/min$ with experimental data: (a) CH_4, (b) C_2H_4, (c) CO, (d) CO_2.
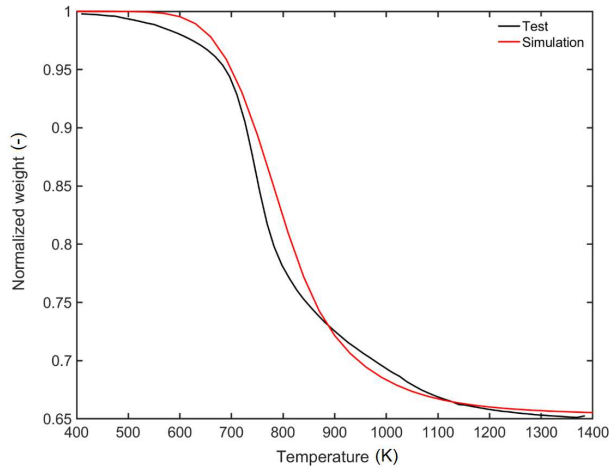
Figure 4.27: Coal total mass decrease calculated from evolved gas compared with experimental result.

4.4 Summary

In this chapter, a single-particle model was developed for the deflagration of coal dust. The TGA experiments were conducted to obtain the kinetic data of the coal sample. Two active pyrolysis phases were identified in the TG curve: at $700 - 800K$ and $900 - 1000K$. The second reaction rate peak is due to the gases tar reaction when the temperature increase to a higher range. In the dust deflagration simulations, the second pyrolysis should not be ignored because it would lead to a lower reaction rate and not promising predictions. Therefore, an alternative approach by counting the evolved gases was used. The evolved gases during the pyrolysis of coal are analyzed by the FTIR instrument. In order to implement the kinetic data and evolved gas content into the dust deflagration simulations, sub-models of the gas evolvement are applied. The kinetic data of the gases were obtained, some of which are two-function models. The models were implemented into the CFD simulations, which is a two-phase Eulerian model including the particle porosity, heat transport of conduction and convection, the pyrolysis of particle and species transport in the porous structure.

The single-particle model shows promising results in the prediction of dust decomposition, including the heterogeneous reaction and mass and heat transport phenomenon. From the 0D and 1D simulation results, the temperature gradient does not effect strongly on the evolution of the volatile content of the particle if the particle size is under $250\mu m$. The further steps would be using the single-particle model to predict the dust explosion process. By using a simplified model, the computation time would

be reduced remarkably and a new method in predicting the dust explosion process is proposed.

Chapter 5

Shock tests and simplified model

This chapter examines the single-particle model developed in the previous chapter (Chapter 4) using different boundary conditions for dust deflagration situations. Dust deflagration occurs when the surrounding temperature suddenly increases and ignites the particles. During the combustion of particles, devolatilization and surface reactions occur on the particle's surface, causing combustion to occur near the particle. Therefore, heat and mass transfer are crucial in determining the combustibility or explosivity of the dust sample. Part of the chapter is published in the paper [104].

5.1   Boundary conditions

At the interface between coal and the ambient gas, an appropriate boundary condition is required to couple the energy equations and to solve the species equations in the single-particle model. Two discretized coal solid cells and one boundary cell are considered for deriving the equations for this boundary.

As shown in Figure 5.1, T_∞ is the ambient gas temperature. The energy conservation indicates that the temperature at both sides of the interface should be equal. Therefore, T_0 is the temperature on the patch/boundary. T_1 is the temperature of the first and second boundary cell center. The distance between the first cell center and the boundary is $\frac{1}{\Delta}$. q''_{conv} is the convective heat from ambient gas to coal. q''_{cond} is the conductive heat transferred from the coal boundary to the coal center. The heat flux is described using the heat transfer coefficient h between the ambient gas and the particle. The convective heat conduction can be described as:

$$q''_{conv} = h(T_0 - T_\infty) \tag{5.1}$$
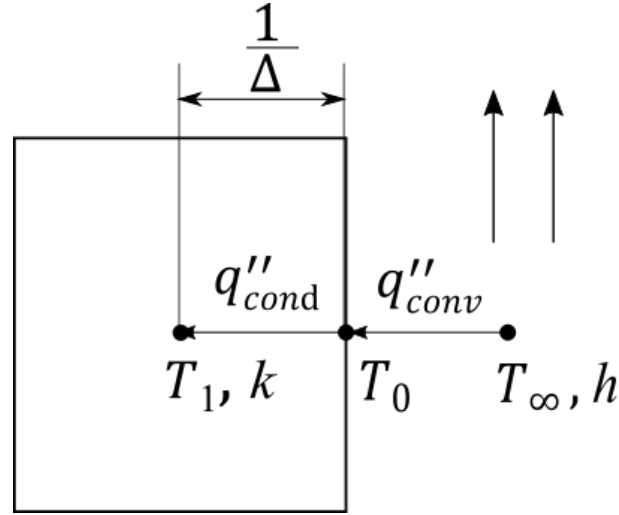
Figure 5.1: Schematic of cells at the boundary between the solid particle and ambient gas.

The heat flux enters into the particle and thus can be calculated from the one dimensional Fourier's law which gives:

$$q''_{cond} = -k\frac{\partial T}{\partial n} \tag{5.2}$$

where k is the thermal conductivity of the particle and n is the direction normal to the boundary. The heat flux that comes from the convective transfer should be equal to that of the conductive heat transfer.

$$q'' = q''_{conv} = q''_{cond} \tag{5.3}$$

The heat flux balance on the boundary is achieved:

$$-k\frac{\partial T}{\partial n} = h(T_0 - T_\infty) \tag{5.4}$$

Assuming a first order discretization of the temperature gradient on the previous equation, gives us:

$$-k\Delta(T_0 - T_1) = h(T_0 - T_\infty) \tag{5.5}$$

The value of the T_0 on the boundary can be calculated as:

$$T_0 = \frac{k\Delta T_1 + hT_\infty}{h + k\Delta} \tag{5.6}$$

By rearranging the equation, it has the form of:

$$T_0 = \frac{1}{\frac{k\Delta}{h} + 1} T_1 + \frac{1}{\frac{h}{k\Delta} + 1} T_\infty \tag{5.7}$$

The ambient temperature where the particle is located changes over time, which also result in the change of the solid properties such as thermal conductivity. Therefore, the boundary temperature T_0 is dependent on the ambient temperature and should be updated in the computation. This boundary condition can be fulfilled using the existing boundary condition "codedMixed" in OpenFOAM.

5.1.1 codedMixed BC

A codedMixed BC is a mixed boundary condition that is defined using an arbitrary function or algorithm that calculates the values of the field at the boundary. The boundary condition can be defined for any type of field, such as velocity, pressure, or temperature.

In a mixed boundary condition, the boundary value is determined by the combination of a fixed value and a fixed gradient [118], which has a form of:

$$\phi_f = \omega \phi_{ref} + (1 - \omega)(\phi_c + \frac{\nabla_\perp \phi}{\Delta}) \tag{5.8}$$

where ϕ_f is the value on the patch that is calculated by the boundary condition code. ω is the weight of the fixed value and the patch normal gradient value, and is named "**valueFraction**" in the code. And these two values are ϕ_{ref} and $\nabla_\perp \phi$ in the equation. They are named "**refValue**" and "**refGrad**" in the code. ω varies from 0 to 1. When it is 0, it refers to a *fixedGradient* boundary condition, the same as the Neuman boundary condition; when it is 1, it refers to a fixedValue boundary condition, the same as the Dirichlet boundary condition. ϕ_c is the internal cell value. And Δ is the inverse distance from the cell face center to the internal cell center. Therefore, in the implementation of the boundary condition, three values should be defined in OpenFOAM: **refValue**, **refGrad** and **valueFraction**.

To implement the "CodeMixed" boundary condition, its physical meanings should be compatible with Figure 5.1. Based on the explanation above, the ϕ_{ref}, $\nabla_\perp \phi$ ω in Equation 5.8 are identified as:

$$\textbf{refValue} = \phi_{ref} = T_\infty \tag{5.9}$$

$$\textbf{refGrad} = \nabla_\perp \phi = 0.0 \tag{5.10}$$

$$\mathbf{valueFraction} = \omega = \frac{1}{\frac{k\Delta}{h} + 1} \tag{5.11}$$

Rearrange Equation 5.8 by inserting these values; the boundary temperature becomes:

$$T_0 = \left(\frac{1}{\frac{k\Delta}{h} + 1}\right)T_1 + \left(\frac{1}{\frac{h}{k\Delta} + 1}\right)(T_\infty + 0.0) \tag{5.12}$$

The "codedMixed" boundary condition is tested using the basic solver laplacianFoam. It solves the heat transport in a flow domain. Its governing equation is:

$$\frac{\partial T}{\partial t} - \frac{\lambda}{\rho c_p}\frac{\partial^2 T}{\partial x^2} = S_T \tag{5.13}$$

Table 5.1: Assessing the efficacy of coded mixed boundary condition tests 1-2 in predicting particle surface heat transfer.Two geometries and different **valFrac** values are tested.

Test	Geometry	BC	BC details
1-1		fixedValue	$1000K$
1-2	$3\mu m \times 3\mu m$	**codedMixed**	**valFrac = 0**
1-3	$\frac{1}{\Delta} = 0.15\mu m$	**refValue = 1000**	**valFrac = 0.5**
1-4		**refGrad = 0**	**valFrac = 1.0**
2-1		fixdValue	$1000K$
2-2	$0.1m \times 0.1m$	**codedMixed**	**valFrac = 0**
2-3	$\frac{1}{\Delta} = 0.005m$	**refValue = 1000**	**valFrac = 0.5**
2-4		**refGrad = 0**	**valFrac = 1.0**

Two sizes of geometries are tested using both fixedValue and codedMixed boundary conditions as shown in Table 5.1. In the two sets of tests, different **valueFraction**s are also used in the codedMixed BC: 0 (Neuman BC), 0.5 (mixed) and 1 (Dirichlet).

The temperature profile of two sets of tests is plotted on the axis of the geometries shown in Figure 5.2. In the **valFrac** = 0 cases, the temperature is a straight line. There is no heat transfer inside the domain. In other cases, the temperature of fixedValue and **valFrac** = 1 are the same. The mixed gradient BC **valFrac** = 0.5 has a slightly lower temperature than the previous two BCs. The first test geometry has dimensions of $3\mu m \times 3\mu m$, while the second geometry is significantly larger, with dimensions of $0.1m \times 0.1m$. Both geometries are 2D with 20×20 cells. Tests with **valFrac** = 0.5 in both cases showed no temperature gradient and no temperature increase in the flow domain. In contrast, the fixedValue cases exhibited a wider temperature range than the **valFrac** = 0.5 and 1.0 cases, indicating more intense heat transfer with fixedValue boundary conditions.

The smaller cell sizes in test 1 resulted in faster temperature transport. Although the difference between **valFrac** = 0.5 and 1.0 was not significant.
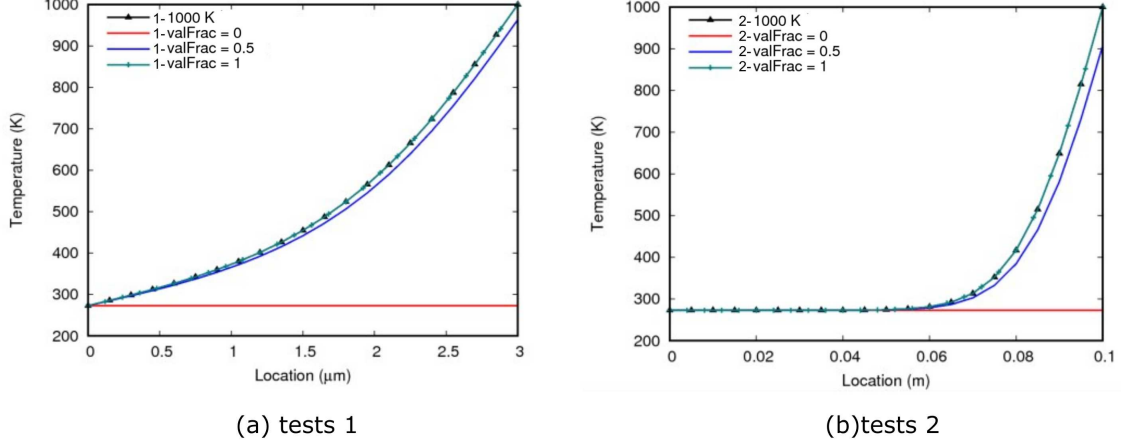
(a) tests 1

(b) tests 2

Figure 5.2: Temperature profiles in the axis of the geometries: (a) tests 1: geometry size $3\mu m \times 3\mu m$; (b) tests 2: geometry size $0.1m \times 0.1m$.

Table 5.2: Assessing the cell size sensitivity and efficacy of coded mixed boundary condition tests 3-4 in predicting particle surface heat transfer.

Test	Gemetry	BC	Cell size
3-1			$0.3~\mu m$
3-2		**codedMixed**	$0.15~\mu m$
3-3		**valFrac = 0.5**	$0.1~\mu m$
3-4	$3~\mu m$ * $3~\mu m$		$0.05~\mu m$
4-1		**valFrac = 2.394e-03**	$0.3~\mu m$
4-2		**valFrac = 1.199e-03**	$0.15~\mu m$
4-3		**valFrac = 7.994e-04**	$0.1~\mu m$
4-4		**valFrac=3.998e-04**	$0.05~\mu m$

The **valueFrac** parameter is crucial in defining the boundaries for dust deflagration, and its value is highly dependent on the cell size $\frac{1}{\Delta}$. To examine the influence of cell size on the results, two additional series of tests were conducted using a geometry size of $3\mu m \times 3\mu m$. In tests 3, the codedMixed boundary condition was used with **valFrac** = 0.3, and the cell sizes were varied between $0.1\mu m$ and $0.3\mu m$. In tests 4, the cell size was varied in each test, and the **valFrac** was adjusted based on the cell size using the equation **valueFraction** = $\frac{1}{\frac{k\Delta}{h}+1}$ (Equation 5.11), where the constant values of $k = 1W/(m \cdot K)$ and $h = 8000W/(m^2 \cdot K)$ were used.

Figure 5.3 shows the temperature profiles of tests 3 and 4 at the central axis of the test domain. Varying the cell size did not affect heat transfer within the test domain.

However, using a finer cell size provided more accurate temperature field predictions as it captured more data in the local field. A slight temperature difference is observed in tests 3, with larger cell sizes showing lower temperatures at the same location in the domain. The $0.3\mu m$ case exhibits a lower temperature than the other cases, suggesting that temperature differences increase as the differences in cell size increase. This finding indicates that cell size has a notable impact on the prediction of temperature fields when using the codedMixed boundary condition, even when employing the same mixed gradient boundary condition. Figure 5.3 shows that the temperature prediction remains consistent across different cell sizes when **valFrac** varies with cell sizes.
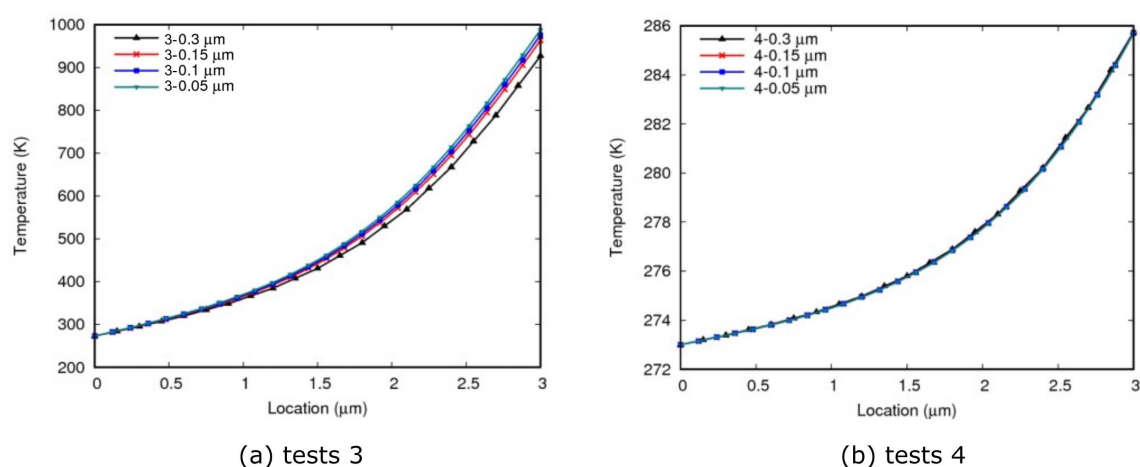
(a) tests 3   (b) tests 4

Figure 5.3: Temperature profiles in the axis of the geometries: (a) tests 3: **valFrac** = 0.5; (b) tests 4: **valFrac** = $\frac{1}{\frac{k\Delta}{h}+1}$.

5.1.2   GroovyBC

A second way we used to implement the boundary condition is the developed external OpenFOAM utilities "groovyBC" [119].

In this boundary condition, the **fractionExpression** determines wheter the face is Dirichlet (1) or Neumann (0). When a Dirichlet-condition (1) is used, the value next to **valueExpression** is read as the boundary temperature. When a Neumann-boundary condition (0) is used, a gradientExpression **gradientExpression** should be defined for the gradient on the boundary. In the tests, four different conditions were used for the same test geometries from previous Chapter 5.1.1. The first three tests used the default functions in the groovy BC, seen in Table 5.3. Test 5-1 is the Dirichlet BC with $1000K$ on the boundary. Test 5-2 and 5-3 are the Neumann BC with 10 and 100 gradient. The boundary condition can also be designed by users by using the implemented expression syntaxes.

The test 5-4 used an expression to define the gradient boundary. The temperature code is listed in the Appendix A.1.

Table 5.3: groovy BC tests for single-particle model

Test	Gemetry	BC
5-1	$0.1m \times 0.1m$	**fractionExpression= 1** **valueExpression** $= 1000K$
5-2	cell size: $0.005m \times 0.005m$	**fractionExpression=0** **gradientExpression=10**
5-3		**fractionExpression=0** **gradientExpression=100**
5-4		**fractionExpression=0** **gradientExpression**$=-(T_{bc} - T_{inf}) * coeff$

In the test 5-1, the temperature range is up to $1000K$ because of a constant boundary temperature value. The tests 5-2 and 5-3 does not induce a high temperature increase inside the domain. The user defined gradient boundary condition is well performed in test 5-4. The temperature profiles in the axis of the geometry is plotted in Figure 5.4. The difference between the testes can be observed. The temperature in side of Grad func is lower than the $1000K$ BC. And the boundary of the Grad fun does not keep $1000K$ even though the ambient atmospheric temperature is $1000K$. In the temperature gradient profiles (Figure 5.5), the gradient of the user-defined gradient BC is also lower than the $1000K$ BC. Therefore, the user-defined gradient boundary condition can be used in the next studies.
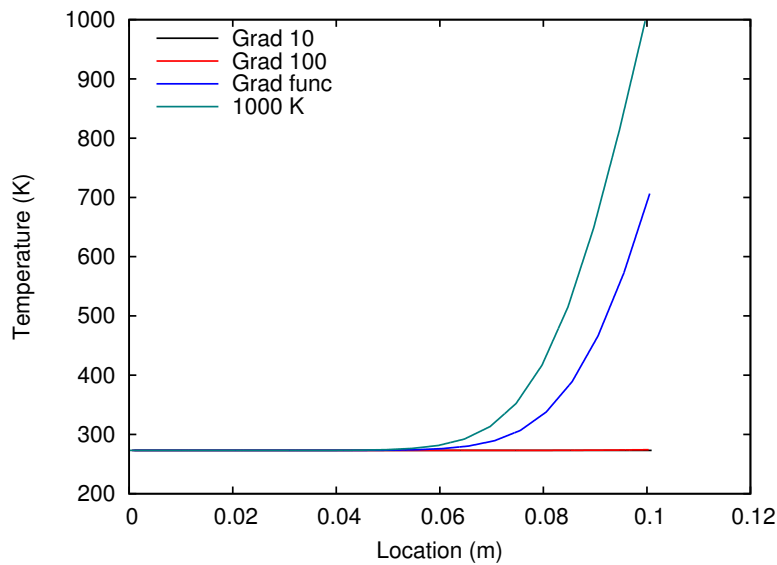
Figure 5.4: Temperature profile from tests 5 in the axis of the geometry.
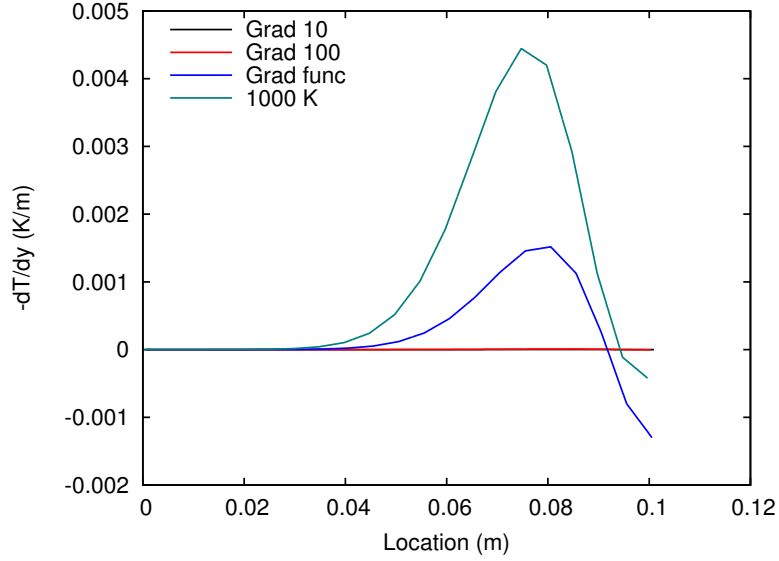
Figure 5.5: Temperature gradient from tests 5 in the axis of the geometry.

5.1.3 Determination of boundary condition properties

The description of the heat and mass transfer coefficient is based on the relationship according to Ranz-Marshall:

$$Nu = 2 + 0.6Re^{1/2}Pr^{1/3} \tag{5.14}$$

$$Sh_i = 2 + 0.6Re^{1/2}Sc_i^{1/3} \tag{5.15}$$

The empirical functions were used because the occurring particle Reynolds numbers in the simulation of flame acceleration ranges between 0 and 36.2 [81]. The approach according to Ranz-Marshall has a range of validity of the particle Reynolds number from 0 to 200.

The particle Reynolds number is calculated using the relative velocity between the particle and the environment fluid flow. It is the ratio between inertial force and the viscous force of the particle,

$$Re_p = \frac{\rho_g |U_g - U_s| d_p}{\mu_g} \tag{5.16}$$

where the ρ_g is the fluid density, d_p is the diameter of the particle, μ_g is the fluid dynamic viscosity.

Determination of heat transfer coefficient

From the result of Spijker [81], the Prandtl number in particle denigration is almost constant. Therefore, its value is assumed as a constant based on the result of porous solid heat transfer properties from [114].

$$Pr = 0.744 \tag{5.17}$$

At the instant of the dust ignition, the particle velocity and fluid velocity are around $5 m/s$ and $100 m/s$ respectively. And their directions are the same. By inserting the values into Equation 5.16, the maximum particle Reynolds number is $Re_{p,max} = 211$. The Nusselt number used in the paper considers the porosity of the particle [114]:

$$Nu = (4.31/12.71\xi + 9.81\xi^2) \cdot (1 + 0.8Re^{0.6}Pr^{1/3}) \tag{5.18}$$

The Nusselt number is much higher than that from [81] ($Nu_{max} = 2.05$). In Spijker's study, the Nusselt number on particle surface is recorded from $50 ms$. The heat transfer is less intensive at that time compared to the instant of ignition. This result is in good agreement with the prediction from [114].

The temperature dependent heat transfer coefficient of coal particle surface is therefore obtained by inserting the variables into the function:

$$h(T) = Nu \cdot \frac{\lambda_g}{d_p} \tag{5.19}$$

In the implementation of the heat transfer coefficient into OpenFOAM boundary conditions, temperature of the solid part and fluid part of one coal particle were considered separately.

The temperature gradient and the individual substances on the surface boundary is defined in the 0 folder of each OpenFOAM case.

$$grad(T) = -\frac{h(T)}{\lambda_s} \cdot (T_s - T_{inf})\xi \tag{5.20}$$

$$grad(T) = -\frac{h(T)}{\lambda_s} \cdot (T_f - T_{inf})(1 - \xi) \tag{5.21}$$

where the h_s, λ_s and T_s, T_f, T_{inf} are heat transfer coefficient between the particle and its surrounding air, thermal conductivity and temperature of the solid and fluid part of the particle, and surrounding air temperature.

Determination of mass transfer coefficient

Similar to the approach in heat transfer coefficient, the mass transfer coefficient uses the Ranz-Marshall correlation:

$$Sh_i = 2 + 0.6Re^{1/2}Sc_i^{1/3} \tag{5.22}$$

The maximum particle Reynolds number is known from heat transfer calculation. $Re_p = 168.25$. Since each substance in the gas phase has a different diffusion coefficient, a separate Schmidt number must be determined for each substance.

To determine the diffusion coefficients of the substances in the mixture, the relationship according to [120] was used. Here, the gas mixture is considered as a gas with an averaged molar mass and an averaged diffusion volume. The simplification has to be made because an exact description of multicomponent diffusion is only possible from the kinetic theory of gases.

$$D_{mix,i} = \frac{1.1325 T^{1.75}\left(\frac{(M_{mix}+M_i)}{M_{mix}M_i}\right) \times 10^{-7}}{p[(\sum V_{mix})^{1/3} + (\sum V_i)^{1/3}]^2} \tag{5.23}$$

The values for the diffusion volumes V were taken from [121]. For molecules included in the pyrolysis stage (CO, CO_2, CH_4, C_2H_4), the averaging of molar mass and diffusion volume mixture are not included as these are considered as second substances. For substances only used in the single-particle model, all substances should be used for averaging the molar mass and diffusion volume. Now a Schmidt number can be determined for each substance through the diffusion coefficient.

$$Sc_i = \frac{\mu}{\rho D_{mix,i}} \tag{5.24}$$

$$h_{mix,i} = \frac{Sh_i D_{mix,i}}{D_{coal}} \tag{5.25}$$

$$grad(Y_{mix,i}) = -\frac{h_{mix,i}(T)}{D_{mix,i}(T)} * (Y_{b,i} - Y_{inf,i}) \tag{5.26}$$

5.2 Temperature profile of shock tests

Due to the small size of the test domain, the simulation is prone to numerical instability. To address this, the grid size is varied, and the results are shown in Figure 5.6. In addition, the time steps in the simulation are kept lower than $1e-6s$ to prevent high heat source

values caused by the numerical instability between the two phases. The simulation is written to file every $0.0001s$ until $0.1s$ and then every $0.001s$ for the remaining time.

The results of varying the grid size in the simulation are depicted in Figure 5.6. The grid sizes tested are $5\mu m$, $3\mu m$, $1.5\mu m$, and $1\mu m$. The particle temperature surpasses $1000K$ within $0.0001s$ at grid sizes of $5\mu m$ and $3\mu m$. As the grid size decreases, the temperature increase rate slows down, and the influence of grid size is deemed acceptable once it is below $1.5\mu m$. The turning point of the temperature curves is attributed to an increase in pore size. At this point, the flow of the pyrolysis gases becomes active, and the velocity exceeds $40m/s$ since the pore size is $5\mu m$. The rapid gas flow reduces the heat transfer on the particle boundary.
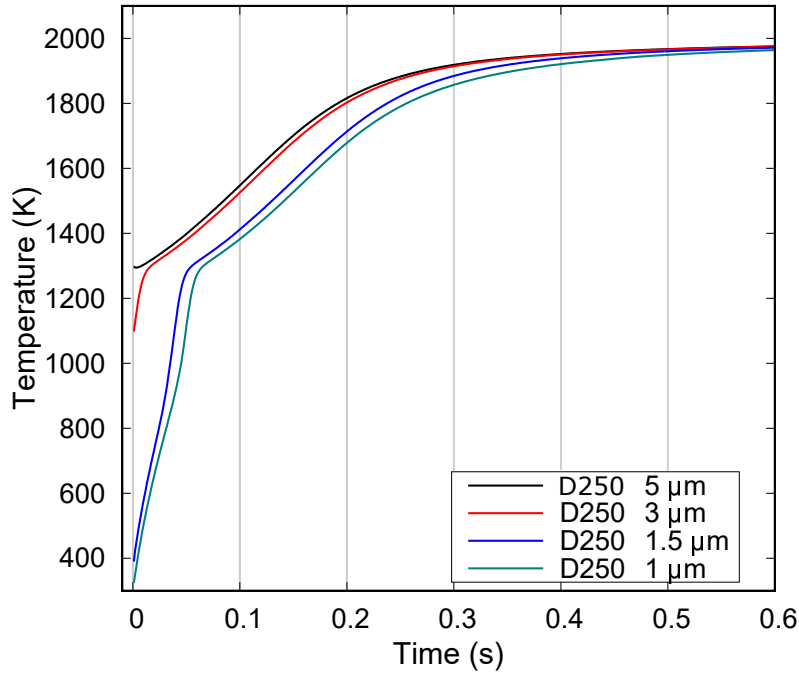
Figure 5.6: Grid size sensitivity analysis for $250\mu m$ particles under shock tests with $2000K$ temperature boundary condition.

In order to investigate the temperature profile and reactions of coal particles under abrupt thermal shock, a shock test was conducted using groovyBC in the single-particle model (see Chapter 4). The boundary condition used in the study was $2000K$, and the simulations were conducted for four different particle sizes: $25\mu m$, $50\mu m$, $125\mu m$, and $250\mu m$. The groovyBC code used in OpenFOAM for the simulations is provided in Appendix A.5 and A.5, which corresponds to Equations 5.20 and 5.21.

The temperature increase over time of $2000K$ shock tests is in Figure 5.7. The positions of the particle core and surface are examined both in the fluid and solid phases of the particle. The T_c and T_s represent core and surface temperatures, respectively.

The intensive heat exchange during the abrupt thermal shock causes the temperature of the coal particle to rapidly increase to $2000K$. This quick heating results in rapid heterogeneous reactions, which release pyrolysis gases. As the particle size increases, the time required to heat the particle also increases. The data presented in Figure 5.7d demonstrates a significant reduction in temperature increase rate as particle size increases. This phenomenon can be attributed to the enlarging coal pore size, which results in a decrease in heat transfer between the particle and its boundary. As the particle size increases, the temperature discrepancy between the fluid and solid phases becomes more pronounced, while the core temperature of the two phases becomes less prominent.
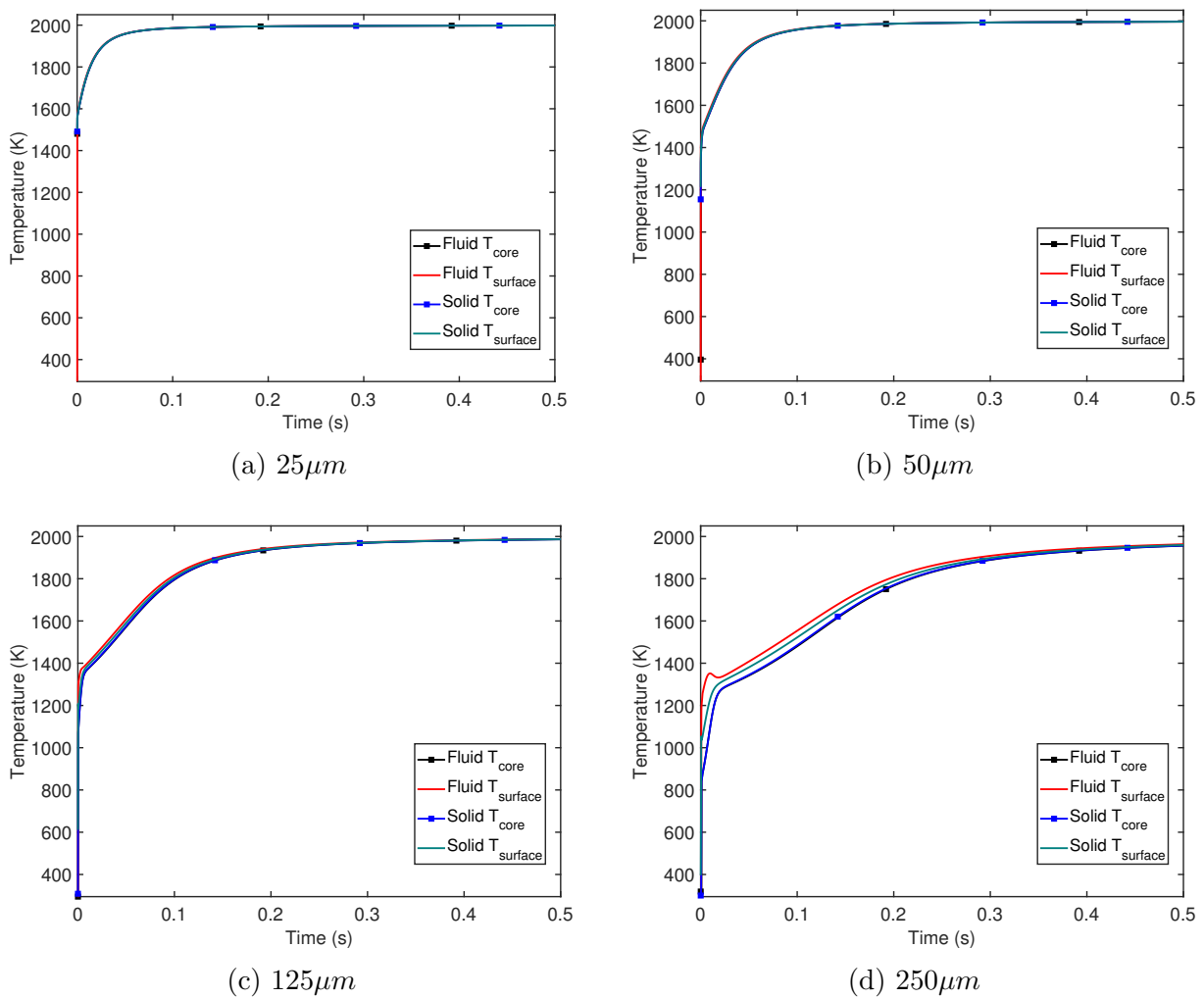
Figure 5.7: The temperature increase of particles with different sizes over time under $2000K$ shock tests, range of $0-0.5s$: (a) $25\mu m$; (b) $50\mu m$; (c) $125\mu m$; (d) $250\mu m$.

In Figure 5.8, the temperature profiles are compared between four particle sizes. The temperature used is the solid temperature and is averaged by the particle volume in order to cancel the particle size influence. When the particle size increases, more time
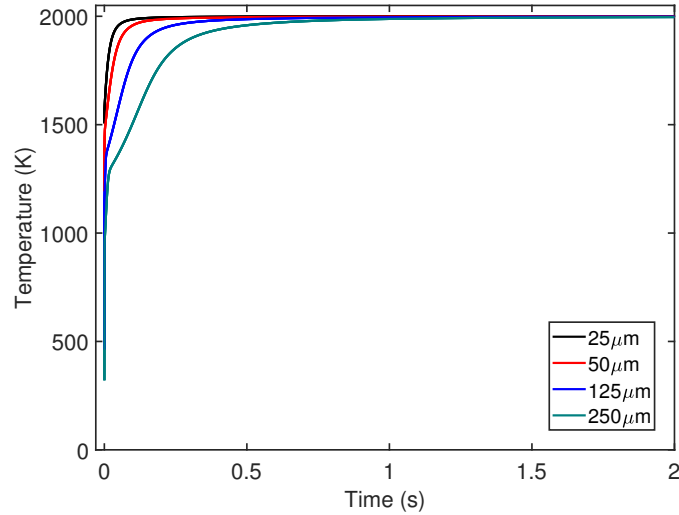
Figure 5.8: The temperature increase of particles with different sizes over time under $2000K$ shock tests: the volume average temperature of different particle sizes.

is required to heat the particle. A sudden increase at the initial time can be observed. After that, the temperature increase becomes slightly slower due to the expansion of the gas phase.

The temperature difference between the surface and the core of the particle is plotted in Figure 5.9. The value is calculated as $\Delta T = T_{surface} - T_{core}$ with the cell values. Due to the instability of the calculation, ΔT starts with high values before it decreases. The temperature difference after the instability starts from $0.03s$, where the most significant difference value is $37K$ in the $250\mu m$ particle. ΔT decreases with a slower speed with time and finally reaches zero.
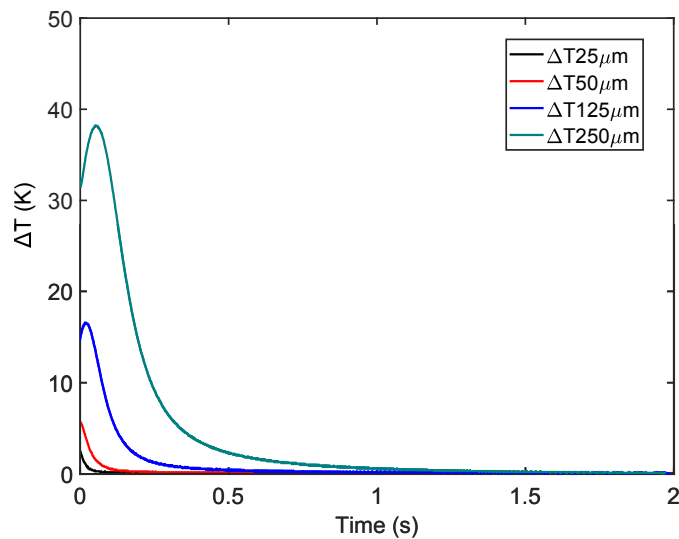
Figure 5.9: The temperature increase of particles with different sizes over time under $2000K$ shock tests: surface and core temperature difference of the particles.

5.3 Evolve gas profile of shock tests

The gas evolution of different sizes of particles is illustrated in Figure 5.10. The volume-averaged values are also used. Each gas specie reaction rate is compared with other particle sizes. The reaction rate of the CO (Figure 5.10a) reaches the highest value and then decreases sharply. The reaction happens between 0 and $0.4s$. The maximum reaction rate is in the smallest particle. The reaction peak moves to later times and becomes wider when the particle size increases. CO_2 has similar patterns as the CO. In CH_4 and C_2H_4, their maximum reaction rates are higher than CO and CO_2. The reaction rate values reach zero earlier.

(a) CO
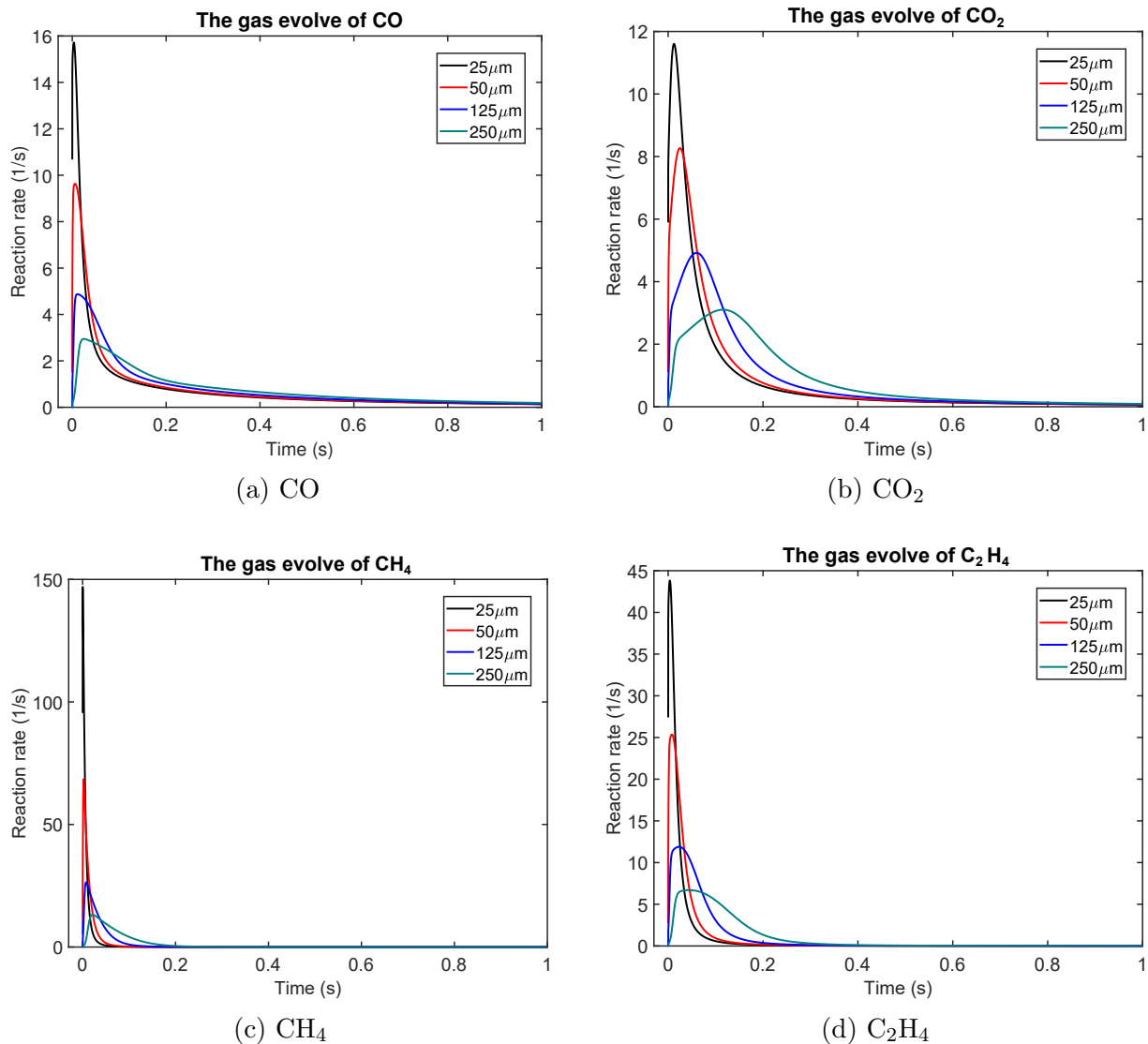
(b) CO_2

(c) CH_4

(d) C_2H_4

Figure 5.10: $2000K$ shock test results: reaction rate in four particle sizes.(a) CO; (b) CO_2; (c) CH_4; (d) C_2H_4.

5.4 Comparison to 0D analytical model

In order to explore the inner particle temperature gradient effect on the prediction of particle reactions. A 0D model using MATLAB was created to model the reaction rate without the temperature gradient.

The difference equation to update the temperature is:

$$T(i+1) = T(i) + h(T_{inf} - T(i)) * 6/(d_p \rho Cp) \Delta t \tag{5.27}$$

where the heat transfer coefficient is:

$$h = Nu \cdot k_g/d_p \tag{5.28}$$

And the Nusselt number used the Ranz-Marshall model.

$$Nu = 2 + 0.6 Re^{(1/2)} Pr^{(1/3)} \tag{5.29}$$

$$Re = \frac{|U_p - U_g| d_p}{\mu} \tag{5.30}$$

The particle porosity is calculated out of the density.

$$\xi = 1 - (m_{p,i}/m_{p,0}) \tag{5.31}$$

And the particle mass is updated by the pyrolysis kinetic, which is the same in the single-particle model (see Table 4.3).

5.4.1 Evolve gas profiles of single particle model and 0D analytical with volume averaged temperature
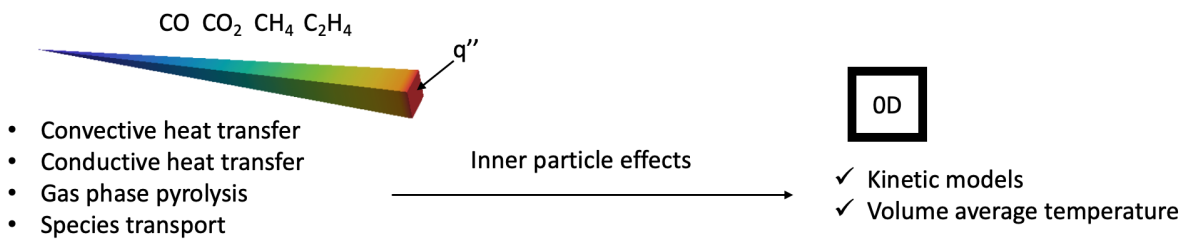
Figure 5.11: Comparison of chemical and physical aspects considered in 0D model and 1D single-particle model.

The simplified temperature, volume averaged temperature (see Figure 5.8), was used in the model. The kinetic models of the evolved gases, particle size, and simulation time range keep the same as the 1D OpenFOAM model. As seen in Figure 5.11, the 1D model single-particle model considers the convective heat transfer, the conductive heat transfer, the gas phase pyrolysis, and species transport. At the same time, the 0D model is simplified by using the average temperature from the simulation results and includes the kinetic models with inner particle effects.
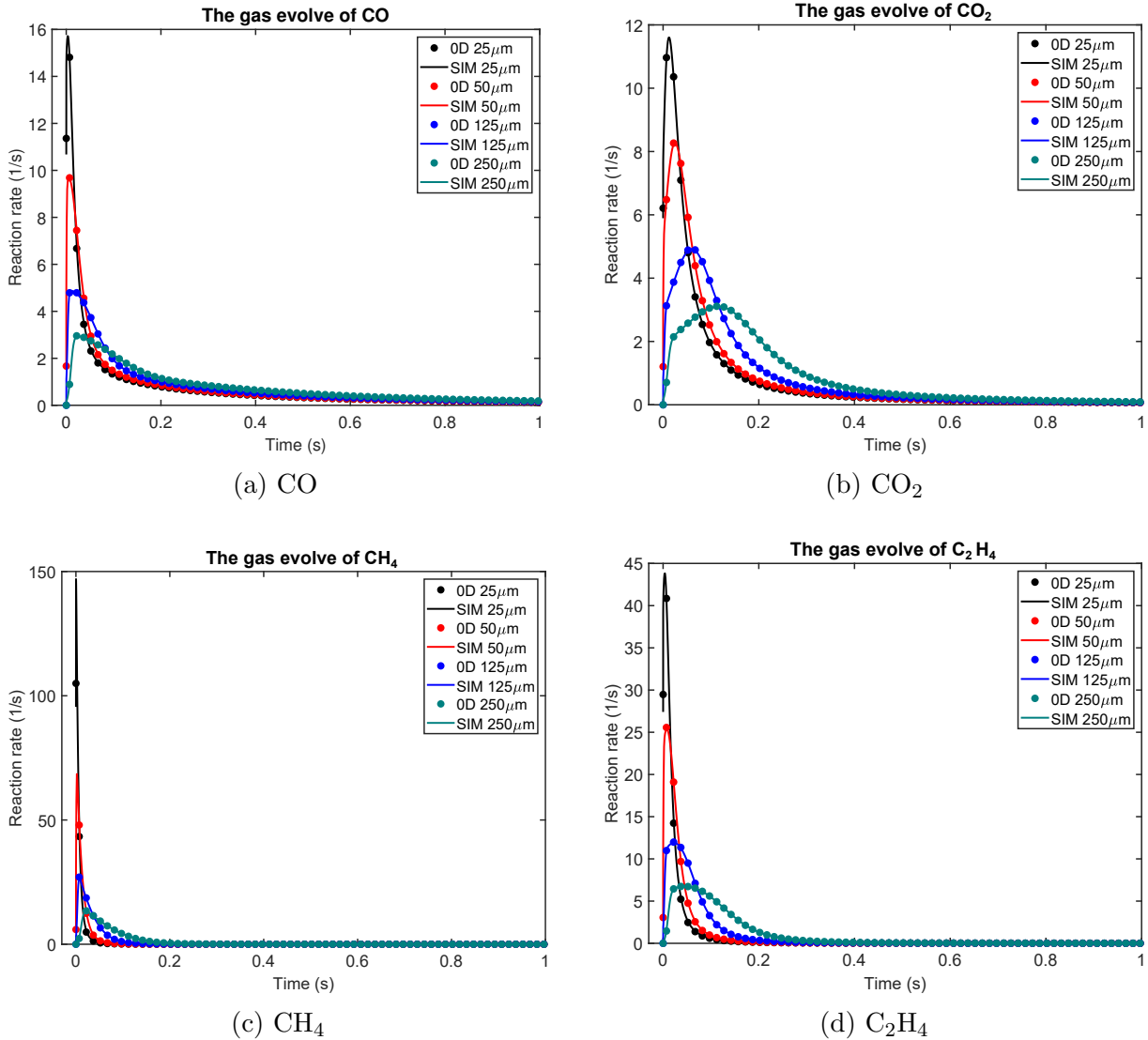
Figure 5.12: $2000K$ shock test results:comparison of the evolve gas reaction rate between 0D and 1D models. Each gas evolve is compared between different particle sizes.(a) CO; (b) CO_2; (c) CH_4; (d) C_2H_4.

Figure 5.12 presents a comparison of the reaction rates of the evolving gases between the 0D and 1D models, where the dots represent the 0D model results. The outcomes of both the 0D and 1D models demonstrate a high degree of agreement, indicating that

the temperature gradient within particles having a diameter of $250\mu m$ or less can be considered negligible in the context of dust deflagration.

5.4.2 Temperature profiles of single particle model and 0D analytical

The 0D analytical model is used for the validation of the temperature predicted by the single-particle model. To eliminate the influence of coal mass and pore size change, the pyrolysis kinetics in the single-particle model is deactivated. Due to the high sensitivity of heat transfer to geometric resolution in thermal shock tests, the geometry is discretized into 100 cells. The porosity is maintained at a constant value of 0.084 as the initial porosity value. A mixture function of the thermal conductivity of the two phases is used for the boundary thermal conductivity of the solid phase, whereas the thermal conductivity of the fluid phase is that of air.

$$K_{mix} = \xi K_f + (1 - \xi)K_s \tag{5.32}$$
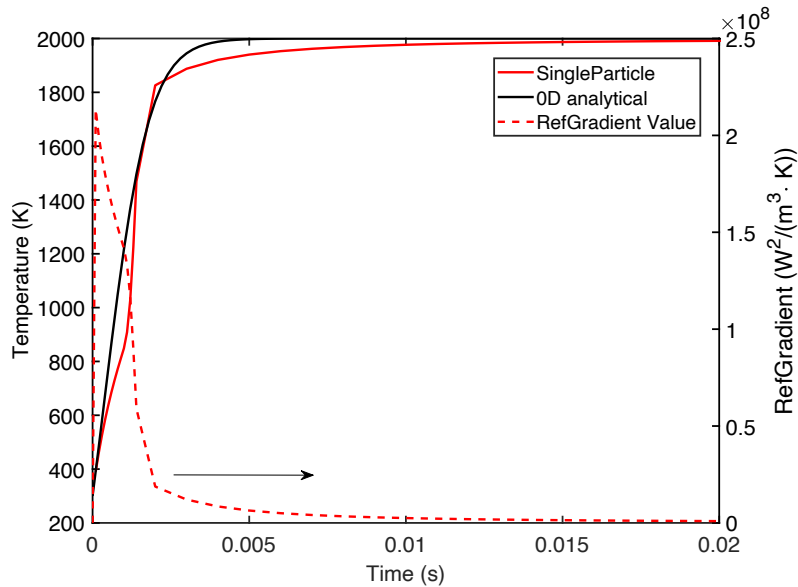
Figure 5.13: Comparison of temperature profile of single-particle model and 0D analytical model.The second y-axis is the **refGradient** value on the temperature boundary condition.

Figure 5.13 compares the temperature increase results of two models. The heat transfer calculation uses Equation 5.20 to determine the **refGradient** value exerted on the particle surface. Initially, the **refGradient** value increases to its maximum as

there is a high temperature difference between the two phases. However, with time, the value gradually decreases as the temperature difference between the ambient and particle temperatures reduces.

The temperature profile of the single-particle model exhibits slight discrepancies with the 0D analytical model. Nevertheless, the single-particle model still demonstrates a reasonable predictive capability for temperature increase.

5.5   Summary

In order to explore the inner particle effects, the shock tests of particles were carried out in this chapter and compared with other models. Unlike the temperature ramp used to reproduce the TGA furnace temperature in the previous chapter, the temperature of the shock tests is considered a sudden increase of the surface. The GroovyBC was used after five sets of tests with different parameters and mesh sizes because it has more size independence than codedMixed BC from the OpenFOAM database.

In the shock tests, $2000K$ ignition temperature was used to heat the particles. And four different sizes of particles, $25\mu m$, $50\mu m$, $125\mu m$ and $250\mu m$, were tested and compared. The particle surface and core temperature differences are not distinct except $250\mu m$. Further, the pyrolysis gas evolvement from the shock tests was compared with the 0D analytical model. The results showed that the temperature gradient in the particles does not make a noticeable difference in the evolved gas. Therefore, the inner particle effects from the porous structure of the coal dust with up to $250\mu m$ can be neglected in the dust explosion simulations. Since the coal powder with higher than $250\mu m$ is much less hazardous in coal dust explosion [122], the model can be applied to most coal dust explosion situations.

Chapter 6

Numerical studies using the models

This chapter conducts simulations of dust explosions utilizing default models, which are based on the dust dispersion data presented in Chapter 3. Additionally, OpenFOAM models concerning the chemical combustion of Lagrangian particles are introduced. The default models are utilized to implement the single-particle model developed in Chapter 4 and tested in abrupt thermal shock in Chapter 5 within OpenFOAM. The results are then compared to the default model. Part of this chapter is published in [123] and [124].

6.1   Numerical models

6.1.1   Devolatilization models

In OpenFOAM there are two default devolatilization models: *constantRateDevolatilization* model and *singleKineticRateDevolatilization* model.

In the *constantRateDevolatilization* model, the volatiles inside of the particles are assumed to be released at a constant rate [125].

$$-\frac{1}{f_{v,0}(1-f_{w,0})m_{p,0}}\frac{dm_p}{dt} = A_0 \tag{6.1}$$

where m_p is the particle mass (kg), $f_{v,0}$ is the fraction of volatiles initially present in the particle, $m_{p,0}$ is the initial particle mass (kg), A_0 is the rate constant (s^{-1}). The gas species is then participating in the gas phase transport.

In the *singleKineticRateDevolatilization* model, it assumes that the rate of devolatilization is first-order dependent on the amount of volatiles remaining in the particle :

$$-\frac{dm_p}{dt} = k[m_p - (1 - f_{v,0})(1 - f_{w,0})m_{p,0}] \tag{6.2}$$

where m_p is the particle mass (kg), $f_{v,0}$ is the mass fraction of volatiles initially present in the particle, $f_{w,0}$ is the mass fraction of evaporating/boiling material when the wet combustion is modeled, $m_{p,0}$ is the initial particle mass (kg), k is the kinetic rates (s^{-1}), which is described by Arrhenius equation.

$$k = A \cdot e^{-\frac{E}{RT_p}} \tag{6.3}$$

where T_p is the particle temperature.

A new devolatilization model was implemented from the single-particle model. The *MultiKineticRateDevolatilization* model implementation code is listed in Appendix A.1, which is further discussed in Chapter 6.5 .

6.1.2 Surface reaction models

In OpenFOAM, there are several options in the surface reaction models such as *COxidationDiffusionLimitedRate* model, *COxidationIntrinsicRate* model, and *COxidationHurMichell* model.

The *COxidationDiffusionLimitedRate* model limits the surface reaction model to:

$$C(s) + Sb * O_2 \rightarrow CO_2 \tag{6.4}$$

where the Sb is the stoichiometry of the reaction.

The surface reaction is assumed to be fully diffusion limited and the reaction rate is calculated as:

$$\frac{dm_C}{dt} = \frac{4\pi d_p D_C^*(Y_{O_2})_s T\rho}{S_b(T_s + T)} \tag{6.5}$$

where the D_C^* is the diffusion coefficient of the oxidants (m^2/s), and $(Y_{O_2})_s$ is the mass fraction of oxygen at the surface of the particle. In the heterogeneous reaction, the oxygen is supplied from the gas phase and the carbon content in the particle is reduced.

The heat of reaction is:

$$q_s = dm_C * Hs(C) - dmCO_2 * Hc_{CO_2} \tag{6.6}$$

where $Hs(C)$ is the sensible enthalpy of carbon (J/kg), $Hc(CO_2)$ is the heat of formation of CO_2 (J/mol).

Other surface reaction models can be referred to [75].

6.1.3 Gas phase combustion model

The simulation employs the Partially Stirred Reactor turbulence model (PaSR) for the turbulence combustion model. PaSR calculates a finite rate using both turbulence and chemistry time scales. The C_{mix} parameter can be utilized to scale the turbulence mixing time scale, depending on mesh resolution. Compared to the Eddy Dissipation Concept (EDC), PaSR has superior predictions for temperature and species concentration when used in conjunction with both RANS and LES models [126].

The PaSR model takes into account both the effects of turbulence flow and chemical reaction kinetics on the combustion process, resulting in a more realistic prediction of the reaction rate. The model consists of two components that consider the reaction in a control volume (PSR). The first component assumes that the reactant and oxygen are well-mixed, while the second component represents the effect of turbulence flow. To describe both components, the model introduces the chemical reaction time scale (τ_{chem}) and mixing scale (τ_{mix}). The reaction products or consumption within the time of $\tau_{chem} + \tau_{mix}$ are then equivalent to the PSR reaction, which is represented as the reaction rate ($\dot{\omega}_r$, in units of $kg/(m^3 \cdot s)$) [126].

$$\dot{\omega}_r^{PSR} = \dot{\omega}_r(\tau_{chem} + \tau_{mix}) \tag{6.7}$$

the actual reaction rate is:

$$\dot{\omega}_r = a \cdot \dot{\omega}_r^{PSR}, a = \frac{\tau_{chem}}{\tau_{chem} + \tau_{mix}} \leqslant 1 \tag{6.8}$$

The chemical time-scale τ_{mix} considers the minimum time of species in the system reaching isotropic equilibrium. The mixing time-scale τ_{mix} considers the time of breakage of turbulence and the mixing of fuel, oxidizer, and anisotropic products.

$$\tau_{mix} = C_{mix}\frac{k}{\epsilon} \tag{6.9}$$

where k is turbulence kinetic energy, m^2/s; ϵ is the turbulence dissipation rate, m^2/s^3; C_{mix} is a constant depending on the type of combustion.

Therefore, the transport equation for PaSR turbulence combustion model is:

$$\frac{\partial(\overline{\rho}\dot{Y}_i)}{\partial t} + \frac{\overline{\partial u_j Y_i}}{\partial x_j} = \frac{\partial}{\partial x_j}(\rho D \frac{\partial \dot{Y}_i}{\partial x_j} - \overline{\rho}\dot{Y}_i'' u'') + \overline{\rho} + \overline{\rho}\dot{\omega}_r \tag{6.10}$$

In current study, the mixing time-scale τ_{mix} is assumed as the turbulence time scale. So the $C_{mix} = 1$.

6.1.4 Radiation model

The radiation model used in the dust ignition is the P-1 model. Typically, P-1 and Discrete Ordination (DO) models consider heat exchange between Lagrangian particles and the gas phase. The P-1 model is not directional dependent due to the assumptions in integration and resulting in a diffusion equation for incident radiation. It includes the scattering effects which can be used on particles. The radiative heat transfer equation is easy to solve with little CPU demand [127]. P-1 model has application in optical thickness, $\tau = a * L > 3$, where L is the distance between objects. This model can be used in combustion. Especially, the value of τ for coal particles lies in the required region [128]. However, it tends to overpredict radiative fluxed from localized heat sources or sinks. Pollhammer [129] proposed that in the choice between the P-1 and DO model in the simulation of particle ignition effects, the results of the two models have no significant difference but the DO model demands high computation time. In this study, due to high particle load, the radiation model P-1 is used.

The P-1 model is the simplest model in P-N radiation models. It is based on the expansion of radiation intensity into an orthogonal series of spherical harmonics [130, 131]. When only four terms in the P-N model are used, the radiation flux q_r is obtained:

$$q_r = -\frac{1}{3(a + \sigma_s) - C\sigma_s}\nabla G \qquad (6.11)$$

where a is the absorption coefficient, σ_s is the scattering coefficient, G is the incident radiation, and C is the linear-anisotropic phase function coefficient. By introducing parameter:

$$\Gamma = \frac{1}{3(a + \sigma_s) - C\sigma_s} \qquad (6.12)$$

The Equation 6.11 is simplified as:

$$q_r = -\Gamma\nabla G \qquad (6.13)$$

The transport equation for the incident radiation G becomes:

$$\nabla \cdot (\Gamma\nabla G) - aG + 4an^2\sigma T^4 = S_G \qquad (6.14)$$

where n is the refractive index of the medium, σ is the Stefan-Boltzmann constant and S_G is the radiation source term.

Combining the Equation 6.13 and Equation 6.14, the term is extracted:

$$-\nabla \cdot q_r = aG - 4an^2\sigma T^4 \tag{6.15}$$

In OpenFOAM source code P1.C, the left hand side in Equation 6.15 is read out by using two functions $Ru()$ and $Rp()$:

$$Sh() = Ru() - Rp()T^4 \tag{6.16}$$

where $Sh()$ is the additional term for the enthalpy equation representing the amount of emitted radiation subtracted from the amount of absorbed irradiation.

The scattering model *cloudScatter* is used to describe the radiation scatter due to the presence of particles. The absorption-emission model is *binaryAbsorptionEmission* which uses two absorption models, including the *cloudAbsorptionEmission* model. The coefficients that are used in the models are absorption coefficient $a(1/m)$, emission coefficient $e(1/m)$, and emission contribution $E(W/m^3)$.

6.1.5 Heat transfer model

In the combustion of a solid particle, the energy transport comes from the heat exchange with the gas phase ($\dot{H}_p$), the devolatilization of the particle ($\dot{Q}_{v,p}$) and the surface reactions ($\dot{Q}_{s,p}$). The specific enthalpy of the particle (h_p) is described as:

$$m_p\frac{dh_p}{dt} = \dot{H}_p + \dot{Q}_{v,p} + \epsilon_p\dot{Q}_{s,p} \tag{6.17}$$

where the ϵ_p is the heat retention coefficient that determines the ratio of energy from surface reaction used to heat the particle or the surrounding gas.

This model assumes a constant size of particles and the density of the particles reduces due to devolatilization and surface reactions.

The temperature throughout one particle is assumed as a constant. The heat exchange from the continuous phase to the discrete phases is described by the RanzMarshall heat transfer model [113], which is the sole existing heat transfer model in the current version of OpenFOAM. In this model, the Nusselt number is determined by the Reynolds and Prandtl number of the particles:

$$Nu_p = 2.0 + 0.6Re_p^{(1/2)}Pr^{(1/3)} \tag{6.18}$$

$$Re_p = \frac{\rho_g |U_g - U_p| d_p}{\mu_g} \tag{6.19}$$

$$Pr = \frac{C_p \mu_g}{\kappa_g} \tag{6.20}$$

The heat transfer coefficient on the particle phase:

$$h = Nu * \kappa_g / d_p \tag{6.21}$$

The heat balance of the particle temperature, $T_p(t)$ considers the convective heat transfer and the absorption/emission of radiation at the particle surface:

$$m_p c_p \frac{dT_p}{dt} = hA_p(T_{inf} - T_p) + \epsilon_p A_p \sigma(\theta_R^4 - T_p^4) \tag{6.22}$$

where c_p is the heat capacity of the particle $(J/kg \cdot K)$, A_p is the particle surface area (m^2), T_{inf} is the local temperature of the fluid (K), ϵ_p is the particle emissivity (-), σ is the Stefan-Boltzmann constant $(5.67 \times 10^{-8} W/(m^2 \cdot K))$, and θ_R is the radiation temperature, $((G/4\sigma)^{1/4})$.

$G(W/m^2)$ is the incident radiation:

$$G = \int_{\Omega=4\pi} I \, d\Omega \tag{6.23}$$

The heat transfer from radiation is included only if the radiation model (see Chapter 6.1.4) is activated. After integration, Equation 6.22 is rearranged as follow:

$$T_p(t + \Delta t) = \alpha_p + [T_p(t) - \alpha_p]e^{-\beta_p \Delta t} \tag{6.24}$$

The value of particle temperature is obtained at the next time step. And

$$\alpha_p = \frac{hT_{inf} + \epsilon_p \sigma \theta_R^4}{h + \epsilon_p \sigma T_p^3(t)} \tag{6.25}$$

$$\beta_p = \frac{A_p(h + \epsilon_p \sigma T_p^3(t))}{m_p c_p} \tag{6.26}$$

6.2 Dust explosion experiment

6.2.1 Experiment setup

In this part, the MIKE 3 apparatus was utilized to perform dust explosion tests on coal samples. Additionally, a high-speed video camera was employed to capture the experimental process. To ensure consistent measurement results, tests were conducted five times for each dust size category. All tests were performed at standard temperature and pressure conditions. The experimental sample consisted of coal, with a density of $1007kg/m3$, which was milled and dried prior to testing. The sample has a size range of $71-125\mu m$. In the experiment, $900mg$ of dust sample was put on the curved bottom under the nozzle. When the experiment started, an air blast was released from a high-pressure container into the dispersion tube. The dust is lifted with the high turbulence flow, forming a cloud in the dispersion tube. According to the test standard in dust explosion, the spark discharge is drawn from the electrodes at $100mm$ above the tube bottom after a specific time from the dust dispersion. The discharge time delay from the onset of the air blast is the ignition delay time, which is $60ms$ in the tests. The ignition delay time decides the turbulence level and dust cloud concentration in the flow domain at the instant of spark ignition. The ignition energy is set at $1000mJ$ to ensure dust ignition. A detailed introduction and result analysis of the dust explosion experiment can be found in documents [11, 132].

6.2.2 Experiment result

Figure 6.1 shows a series of recorded images of the flame propagation of coal dust at a concentration of $750g/m^3$ and particle diameter of $125\mu m$. At $0.001s$, a faint flame shows after the spark ignition, which propagates slowly for several milliseconds, which could be due to the burning of small and easily released volatile particles of coal particles which leads to weight loss. The particles are separated by the volatiles released from the heated particles. When the oxygen diffuses to the surrounding of the particle, the combustible volatile gases react. The heat from combustion continues to heat the separated particles. The flame starts to be luminous, which is a diffusion-controlled reaction. The flame shape is irregular due to the particle suspension conditions at the instance of ignition. As seen in $0.03s$, the flame has a direction towards the left wall because there is more particle accumulation, which means more reactant. The flame propagates along the wall and continues to heat particles nearby. Therefore, the particles on the right side of the tube are ignited. The flame is very luminous in the active reaction center due to the high

volatile content released from particles. This also explains the discontinuous flame front. The flame top front is hard to capture due to scattering burning particles, which can be observed in 0.07s. Similar irregular flames were also observed by Kern [133], who did flame propagation experiments using lycopodium particles in a 2-meter-long cylindrical tube. Different from his result, the flame in the MIKE 3 does not propagate to the bottom of the tube intensely due to the lack of oxygen. Only part of the dust is combusted, which can be identified from 0.04s to 0.08s. Similarly, the particle concentration towards the right bottom of the tube is high, and more combustion heat is produced, indicating a lower temperature gradient in the neighborhood of the particle. The high particle concentration part is named particle clusters in the study of Hosseinzadeh [11]. The flame reached the top of the tube at 0.08s. After that, the flame still burns as the flame is extinct, and more oxygen is diffused to the tube bottom.
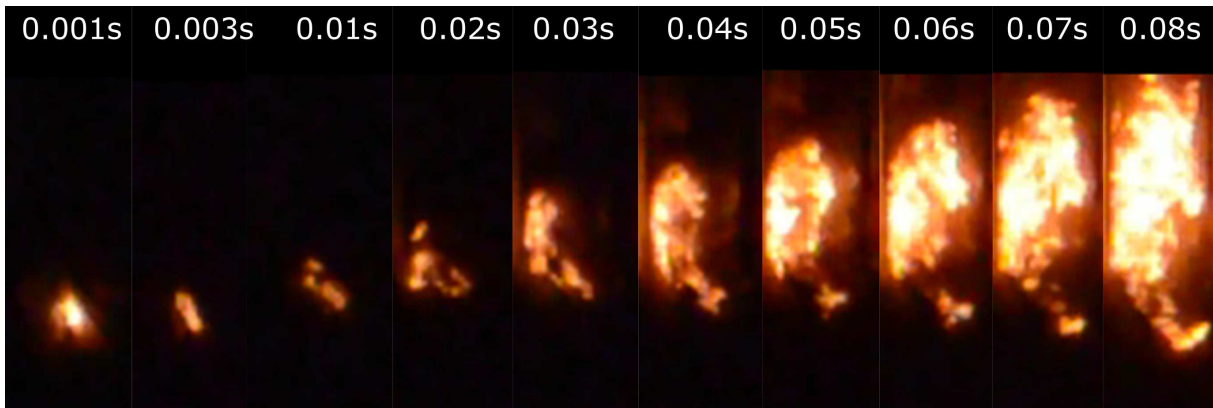
Figure 6.1: Video screen shot at different time of dust explosion propagation.

The variation of flame front positions with different particle size ranges is shown in Figure 6.2. The flame front in each video frame is captured using RGB filters in MATLAB. One example of the image process is shown in Figure 6.3. Firstly, the resolution of each frame in the video is obtained. In this example, the pixel count is $650'' \times 240''$. Then, in each frame, the colored image is filtered by red, green, and blue colors. The green tunnel filter is used in the presented example because it gives the best edge capture. The threshold in the green tunnel filter is defined, and at last, Figure 6.3(c) returns the edge of the flame shape. The treatment was applied to all the frames, and the flame front position was obtained by the pixel value. Finally, the flame front positions were defined, and corresponding times are counted by the frame number.

In Figure 6.2, the flame front positions as a function of time of different particle size ranges are depicted. The flame propagation velocity increases after a while because the flame reaches the tube wall. Due to the confinement, the pressure and the flame
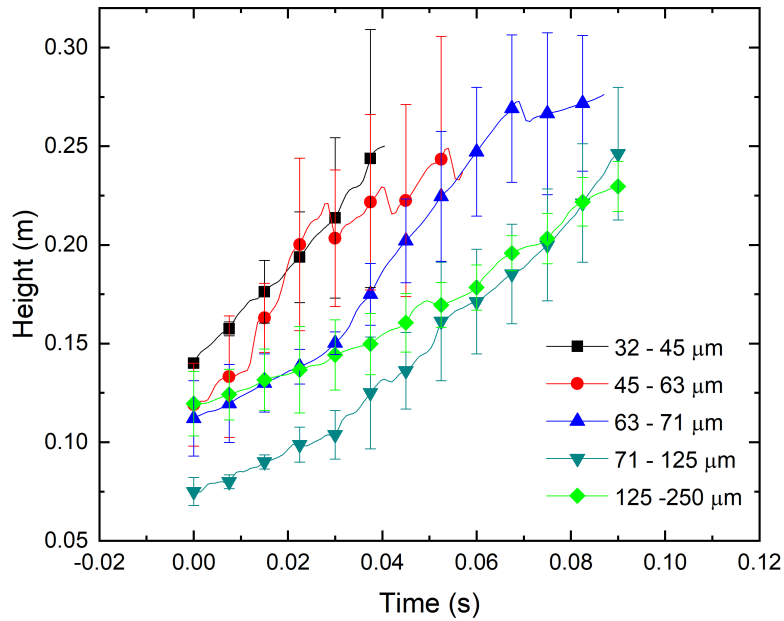
Figure 6.2: Flame front position of different sizes of coal dust over time in MIKE 3 apparatus.

(a) Original   (b) Green tunnel level   (c) Flame edge
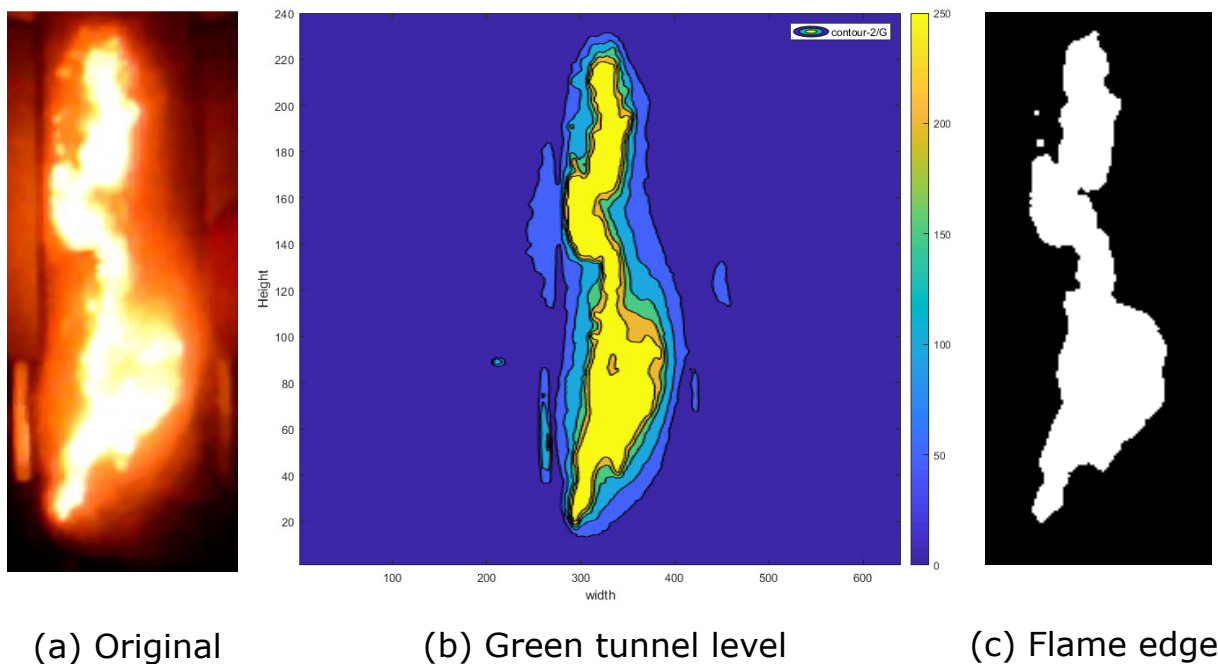
Figure 6.3: Flame image treatment process by RGB filters.(a) The original snapshot of the dust flame; (b) The green tunnel image; (c) Flame shape filtered by the threshold value of the green tunnel.

velocity increase. For example, in the $71 - 125\mu m$ case, the time it reaches the tube wall is around $0.05s$, which corresponds to Figure 6.1. As the particle size decreases, there is an overall pattern that the lateral flame propagation becomes faster due to the lower critical time. The flame velocity also increases as the particle size decreases. However, the flame propagation is strongly influenced by the initial flame position generated during the spark. The starting positions of the flames increase as well as the particle decreases. This can be explained by the cloud clusters in the domain. The smaller particles tend to concentrate at a higher position at the same ignition delay time, leading the initial flame to a higher position.

6.3 Dust explosion simulations in the 2D geometry

The 2D simulation employs a simplified geometry, representing the center plane of the MIKE 3 apparatus. Its primary objective is to assess the feasibility of simulations involving high particle loads. In coalChemistryFoam, particles are treated as infinitesimal points, and their coordinates, temperature, velocity, and species are computed in each Lagrangian time step. The explosion encompasses chemical and physical changes, and the combustion model is implemented in greater detail than in the dust dispersion process (refer to Chapter 3).

6.3.1 Numerical domain and simulation cases

Outlet

Wall

(a)Geometry   (b)Particle position
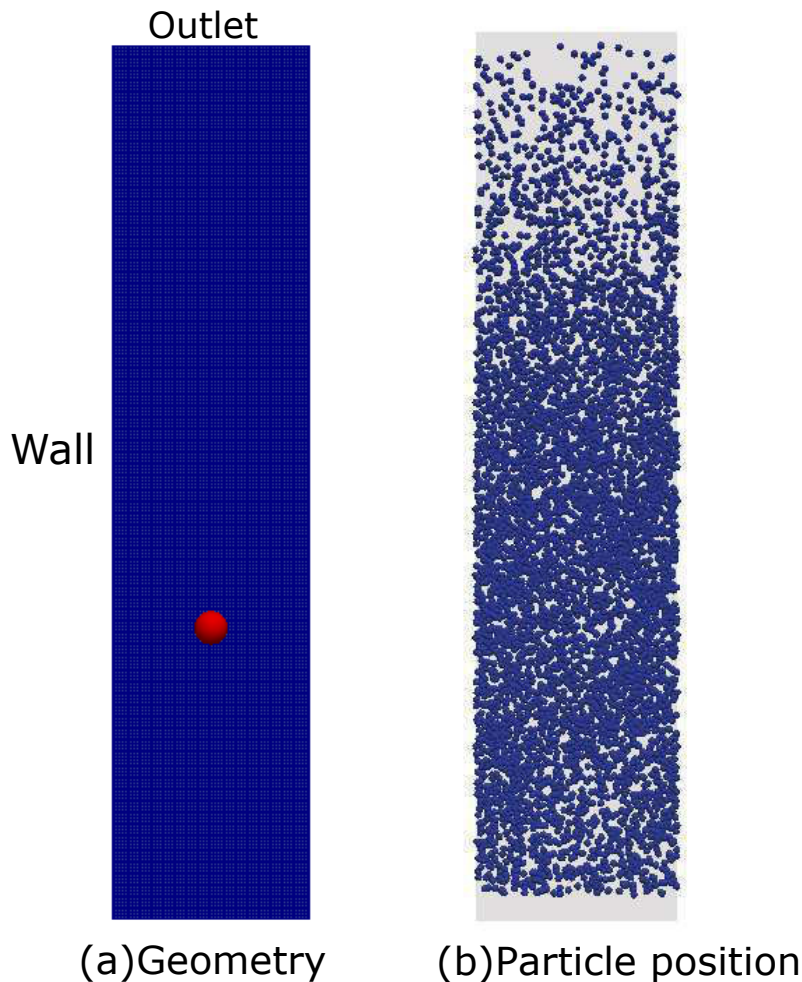
Figure 6.4: The numerical domain of simulation.(a) The two-dimensional geometry represented with meshes. Outlet is on the top. The red sphere ($D = 6mm$) marks the position of the ignition position. (b) The initial particle positions of $125\mu m$ particles at the instance of ignition [97].

Figure 6.4 depicts the utilization of a numerical domain that exists in two dimensions. The geometry simplified the domain of the MIKE 3 apparatus into a rectangular plane. It has a dimension of $300mm$ in height and $68mm$ in diameter. The spark ignition source is located at the center of the tube at the height of $100m$, which is marked with a red sphere in the figure. The diameter of the ignition source is $6mm$. The geometry is discretized into 22 000 hexahedra cells. The grid size is $1mm$ and is enough to capture the intensive heat transport phenomenon. The top of the geometry is the outlet, and the others are walls as boundary conditions. The initial temperature in the internal field is $300K$. Figure 6.4b indicates the particle positions at the instant of spark ignition. The positions are obtained from previous simulation results in the particle propagation simulation [92, 97]. Contrast cases with evenly distributed particles are also simulated to explore the influence of particle concentration. The temperature in the ignition source is $2000K$. It starts from $0.001s$ and lasts for $0.1s$ in order to ignite the particles. The particles are set as fixed in three cases: $25\mu m$, $125\mu m$, and $250\mu m$. The total particle mass is $900mg$, and the mass parcel basis is used in the simulation. The solid particles are two-way coupled with the flow domain. A summary of the simulation parameters used in the present study is shown in Table 6.1.

Table 6.1: Simulation parameters used in the 2D explosion model.

Parameter	Value
Fluid	Air
Solid	Coal dust
Particle size (μm)	25, 125, 250
Dust concentration (g/m^3)	750
Particle density (g/m^3)	1 007
Ambient pressure (Pa)	100 000
Temperature (fluid) (K)	300
Temperature (solid) (K)	300
Ignition temperature (K)	2 000
Cell size (m)	0.001 - 0.002
Simulation time (ms)	500
Ignition period (ms)	0 - 100

6.3.2 Numerical simulation results of flame propagation

Because the particle cluster affected the flame propagations during the explosion, different particle distributions were used in the simulation. Figure 6.5 summarised the flame propagation in the simulations. The letter 'e' marks the cases with evenly distributed particles. The flame propagates over time until it reaches the outlet. The $250\mu m$ case

finishes the propagation at $0.16s$, much slower than the other two cases. However, the flame speed of the smallest particles $25\mu m$ is not higher than the $125\mu m$ particles because the $25\mu m$ particle escape from the outlet and less fuel exists. The initial particle positions do not seem to influence the flame propagation. The thermal expansion and the evolved gases push away the particles at the flame front.
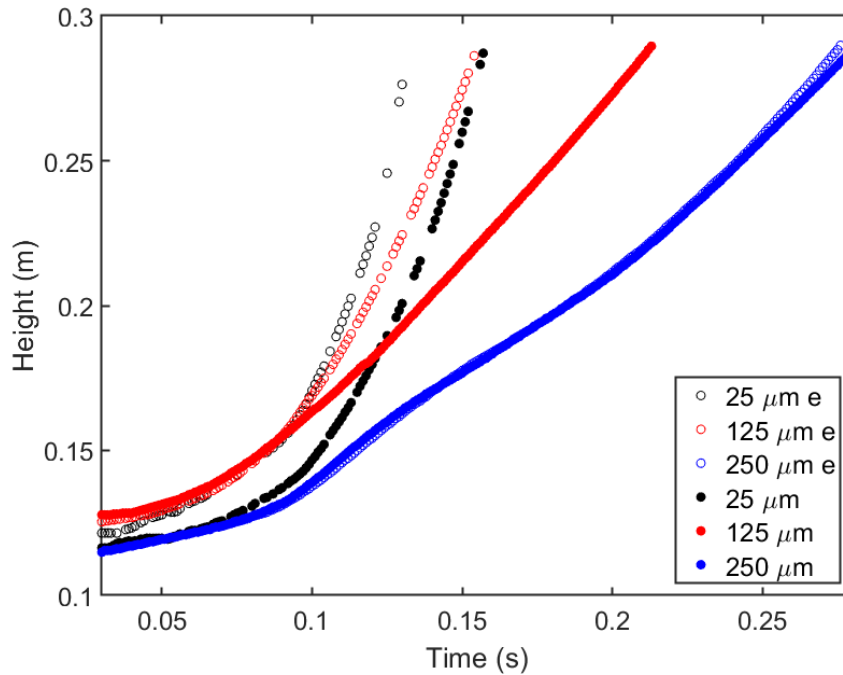
Figure 6.5: Flame front propagation with varied initial particle positions in 2D simulations: comparing evenly distributed ('e') with unevenly distributed particles.

6.3.3   Particle propagation characteristics

Simulations were conducted to study the behaviors of particles with initial positions evenly distributed over the tube. Figures 6.6-6.7 present the results of particle concentration and gas content over time for the $250\mu m$ particle size case. The x-axis corresponds to the longitudinal axis of the MIKE 3 apparatus, while the y-axis represents the particle concentration.
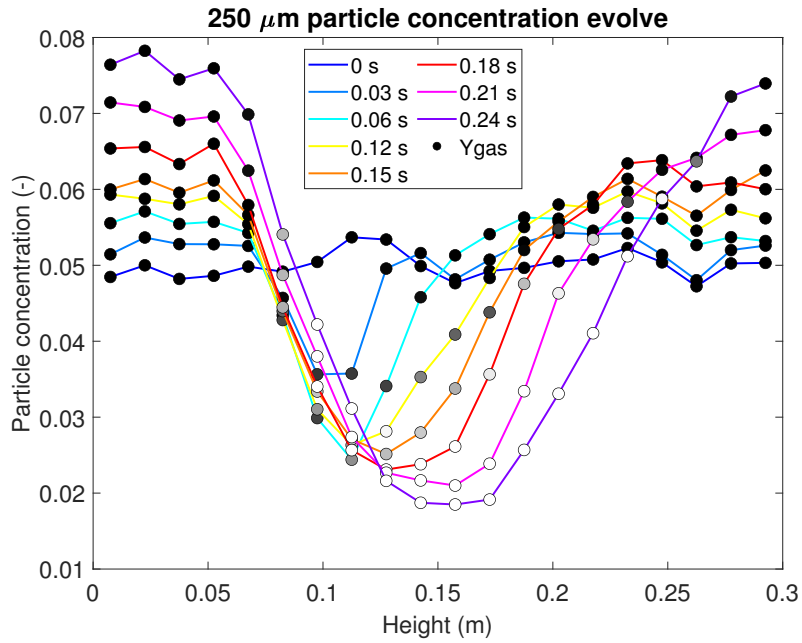
Figure 6.6: Evolution of $250\mu m$ particle concentration and volatile content along the tube axis with evenly distributed initial particle positions: visualizing gas content with grey-scale circles.
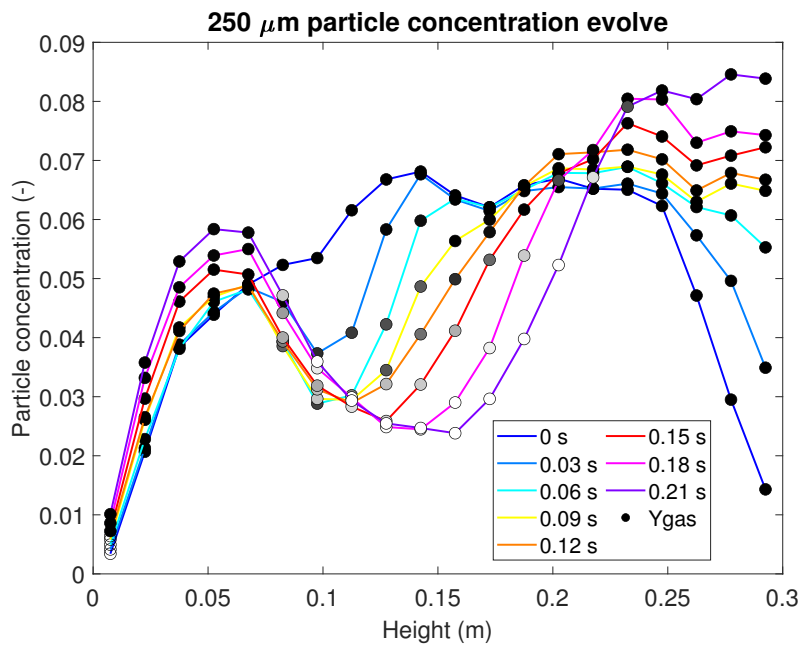
Figure 6.7: Evolution of $250\mu m$ particle concentration and volatile content along the tube axis with unevenly distributed initial particle positions: visualizing gas content with grey-scale circles.

A 'U' shape gradually forms when the ignition starts in both cases. The particle concentration decreases remarkably near the ignition source over time. Particles that are initially lower than the ignition point descends to the bottom of the tube over time. The shape 'U' becomes wider over time due to the flame propagation. In Figure 6.7, the initial position of particles is distributed in the domain with different concentrations. There are more particles between $0.1m$ and $0.25m$ and fewer near the bottom of the tube. The particle concentration at the bottom of the tube does not increase remarkably, resulting in a higher particle concentration at the top of the tube compared to Figure 6.6.

The circles in the figures represent the volatile content of the particles, with the shade of the filling indicating the remaining volatile content. Black denotes that all volatiles are present, while blank indicates that all volatiles have been released. Moreover, the circles can also be used to indicate the position of the flame front. Due to gas expansion, the particle concentration is at its lowest near the center of the flame. Additionally, the particles near the ignition source begin to decompose as the flame forms. As the flame propagates, more particles are burned.

6.4 Pilot simulations using coalChemistryFoam 3D

6.4.1 Numerical domain and simulation case

The three-dimensional numerical domain for the current model is shown in Figure 6.8, which has the same dimensions as the explosion tube in MIKE 3 apparatus. It is a $1.2L$ vertical cylinder with a dimension of $300mm$ in height and $68mm$ in diameter. The spark ignition source is located at the center of the tube at the height of $100m$. The geometry is discretized into 600 000 hexahedra cells. The grid sizes range from $1mm$ to $2mm$, enough to capture intensive heat transport. The outlet is the top of the tube, and the others are walls as boundary conditions. The initial temperature in the internal field is $300K$. Figure 6.8(b) indicates the particle positions at the instant of spark ignition. The positions are obtained from previous simulation results in the particle propagation simulation [92]. The spark ignition is set as a sphere region with $6mm$ radius. The temperature in the ignition source is $2000K$. It starts from $0.001s$ and lasts for $0.01s$ in order to ignite the particles. The particles are set as monodispersed with a diameter of $125\mu m$. The total ignited particle mass is $900mg$ and the mass parcel basis is used. The solid particles are two-way coupled with the flow domain. A summary of the simulation parameters used in the present study is shown in Table 6.2.
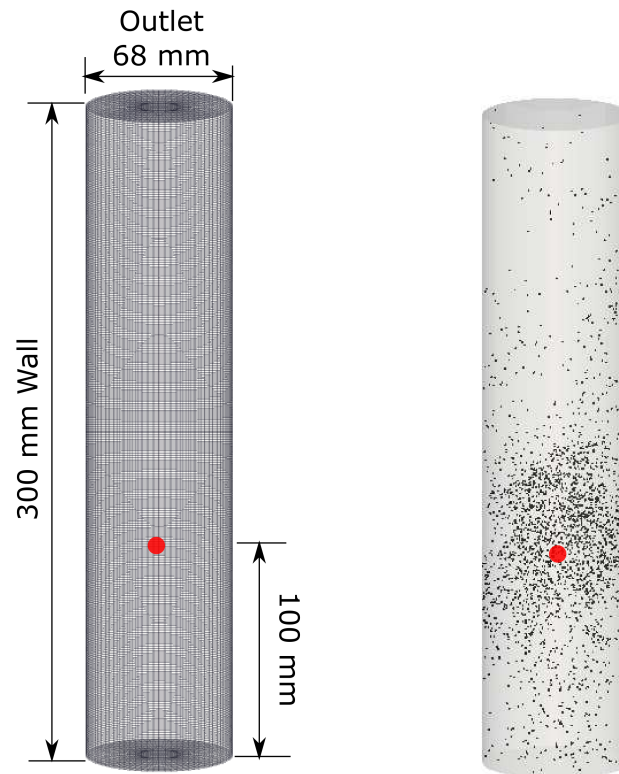
Figure 6.8: Schematic of three-dimensional computational domain indicated the ignition source position. (a) the geometry scale and boundary conditions; (b) the initial position of dust cloud.

Table 6.2: Simulation parameters used in the 3D explosion model.

Parameter	Value
Fluid	Air
Solid	Coal dust
Particle size (μm)	125
Dust concentration (g/m^3)	750
Particle density (g/m^3)	1 007
Ambient pressure (Pa)	100 000
Temperature (fluid) (K)	300
Temperature (solid) (K)	300
Ignition temperature (K)	2 000
Cell size (m)	0.001 - 0.002
Simulation time (ms)	180
Ignition period (ms)	1 - 11

6.4.2 Simulation results
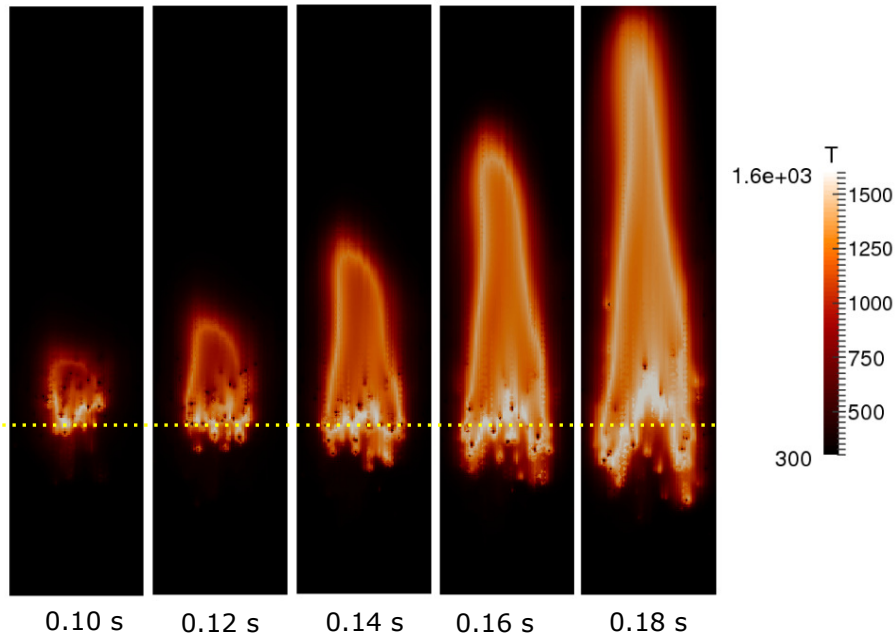
Figure 6.9: Simulation results of coal cloud flame propagation over time in the 3D geometry with stationary particles as initial condition.

Figure 6.9 shows the flame propagation in the simulation, and the yellow dashed line marks the height of the ignition source. The particle starts to form a flame at $0.1s$ when the ignition source ends. It differs from the experiment, where the flame forms at $0.003s$ right after the spark discharge. Such a high energy transfer condition is hard to achieve in the simulation due to the instability and unknown material property at very high temperatures [129]. It can be observed from Figure 6.9, that the flame gradually spreads to the top of the tube. At $0.18s$, the flame front reaches the outlet. The propagation lasts for $0.08s$, which agrees with the experiment result. At $0.1s$, the coal particles near the ignition source lose volatile content. The volatiles in the surroundings of the particle combust due to the high temperature. After that, the ignition source is removed, and the heat transfer continues with the heat of combustion. The presence of darker coal particles can be found near the yellow line. The particle temperature is lower due to the release of volatile content. There is also a temperature gradient around the particles. The highest temperature in the field locates neighboring the particles, where active homogeneous combustion occurs. Due to air expansion and buoyancy, the flame spreads upward. In the meantime, the burning particles simultaneously drive the flame to the bottom of the tube as a result of gravity. The particle concentration is higher near the yellow line compared

to the upper part of the tube. These particle clusters yield more combustible gases and higher combustion heat.

The coal particle decomposition level is shown in Figure 6.10. The Ygas represents the particle volatile content varying from 0 to 1. When the Ygas equals 0, all the volatiles from one particle is released by the devolatilization. At $0.1s$, the particles in the ignition source region are heated up and release a large percentage of gas volatiles. The particles decrease into a lower location due to gravity. The high-temperature volatile gas moves upwards due to buoyancy and is combusted when the oxygen diffuses to the particle surroundings. The fully decomposed particles become more in the lower part of the tube, where more active combustion happens due to the high particle concentration. At $0.16s$, the particle number is low in the upper part of the tube, and the particles are mostly undecomposed. This indicates that the fuel in the flame front is raised from the middle of the tube. At $0.18s$, the flame reaches the outlet, while high particle accumulation is found at the bottom of the tube. Those particles are not combusted due to the lack of oxygen.
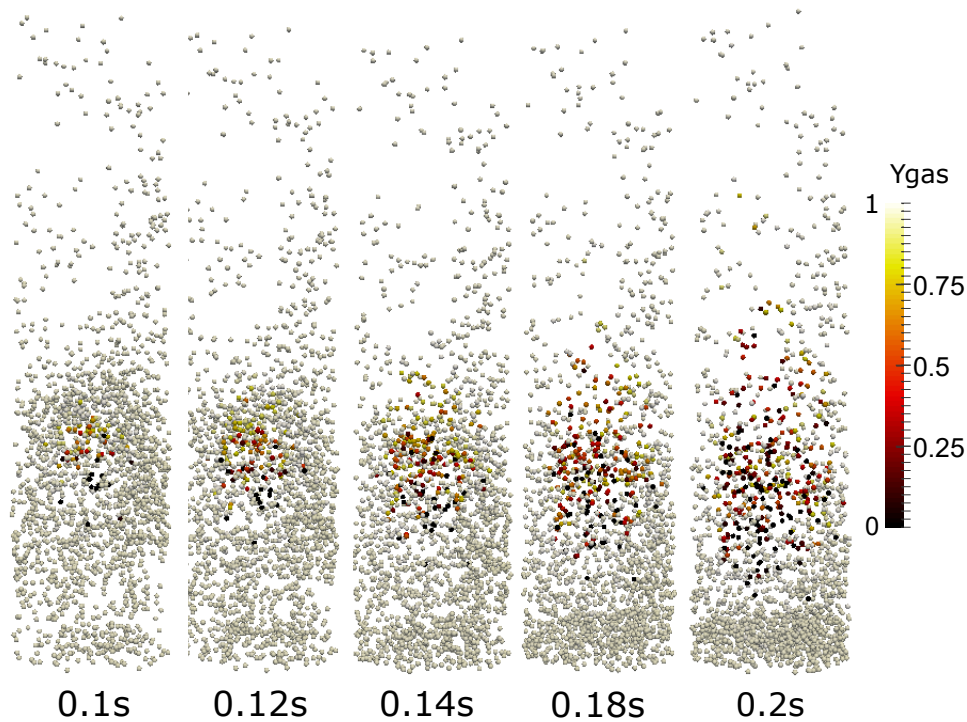
Figure 6.10: Simulation results of coal particle volatile content over time.

6.5 Single-particle model implementation

6.5.1 *MultiKineticRateDevolatilization* model

A novel devolatilization model is developed based on the single-particle model. To utilize the model, specific data pertaining to the evolved gas must be defined. The data used in the model is provided in Listing B.2, and is derived from the kinetic analysis conducted on the coal sample (Table 4.3).

To examine the implementation of the model, a Lagrangian particle simulation is performed. The particle is placed in an environment with a temperature of $2000K$, while the particle motion is suppressed, and the force coupling with the gas phase is not activated. This approach is adopted to check the evolution of the pyrolysis gases. The comparison of particle reaction rate between the simulation model and the single-particle model is illustrated in Figure 6.11. When treating the particle temperature as a single value within the particle, the simulation model shows an acceptable level of discrepancy with the single-particle model. However, the simulation model predicts a slightly faster decrease in the reaction rate of CH_4. Additionally, a higher degree of numerical instability is observed at the beginning of the simulation in the prediction of CO and CO_2. Nonetheless, the implementation of the single-particle model is deemed successful, and the kinetics of different gases are prominently displayed in the simulation results.
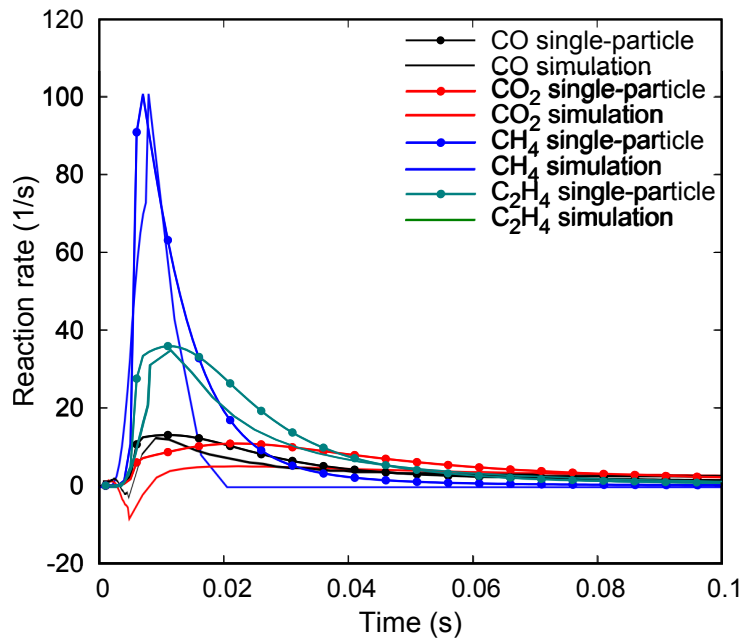
Figure 6.11: Comparison of pyrolysis gas reaction rates: single-particle model vs OpenFOAM simulation with *MultiKineticRateDevolatilization* model.

114

6.5.2 Comparison with default OpenFOAM case

To further evaluate the model, a single coal was burned at a fixed location using the 2D geometry from the default coalChemistryFoam case. The ignition source had a temperature of $2000K$, and its location, with a diameter of $0.005m$, is shown in Figure 6.12. Additional simulation properties can be found in Table 6.3.
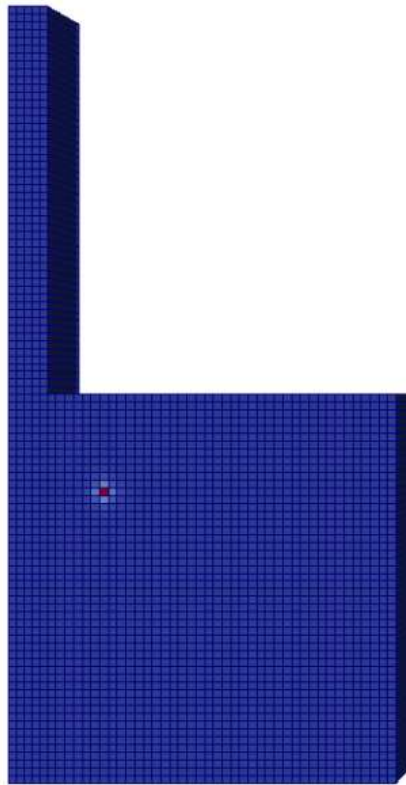
Figure 6.12: Test geometry and ignition source position for single-particle model implementation.

The outcomes of the initial experiment are depicted in Figure 6.13, where the symbol D signifies the utilization of the *singleKineticRateDevolatilization* model as the default devolatilization model, whereas the symbol M denotes the utilization of the *MultiKineticRateDevolatilization* model. The temperature of the particles is presented as red curves in the same figure. Throughout the simulation, the ignition temperature is maintained at $2000K$.

The coal particle starts to lose the volatile gases when the temperature reaches $600K$ in the default model, shown as the dashed lines. In the new model, the evolved gas is released at different temperatures. The particle temperature increases faster than the new model in the default model due to more active gas flows. The volatile in the default model is completely released at $0.1s$. While in the new models, the gas volatile is not

entirely released. The mass loss curves of the new model show a "step" shape and are further validated with a new simulation that has a smaller geometry.

Table 6.3: Simulation parameters for comparison of the *MultiKineticRateDevolatilization* model and the default model in OpenFOAM.

Parameter	Value
Fluid	Air
Solid	Coal particle
Particle size (μm)	250
Particle density (g/m^3)	1 007
Ambient pressure (Pa)	100 000
Temperature (fluid) (K)	400
Temperature (solid) (K)	300
Ignition temperature (K)	2 000
Cell size (m)	0.01
Simulation time (s)	5
Ignition period (s)	0-0.5
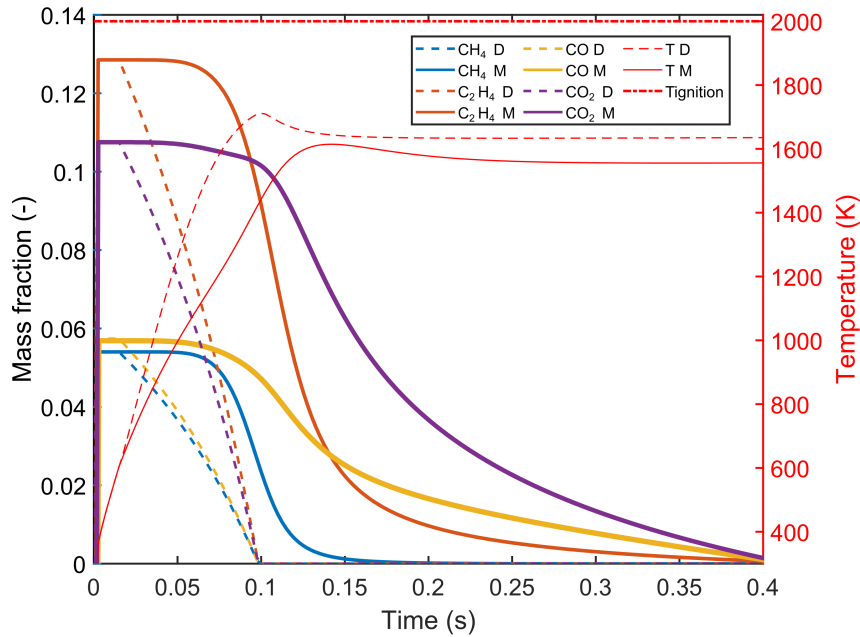
Figure 6.13: Comparative analysis of temperature and particle composition profile in a single-particle simulation using the *MultiKineticRateDevolatilization* model (M) and default model in OpenFOAM (D).

To investigate the impact of particle heat exchange, a one-cell simulation geometry was constructed and compared against the results obtained by Cloney [86]. A particle was positioned at the center of the geometry, as shown in Figure 6.14, and the comparison

was carried out to evaluate the influence of the particle devolatilization model on the heat transfer process.
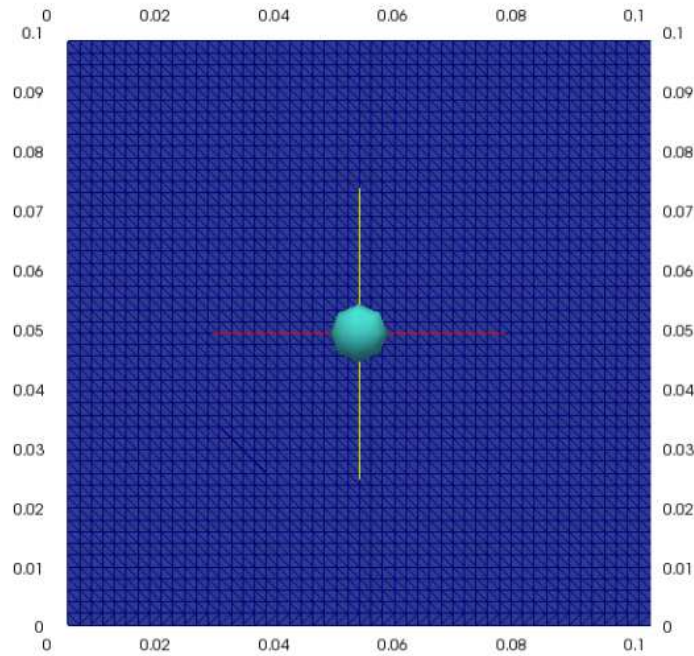
Figure 6.14: One cell simulation geometry and indication of particle position (Sphere represents the particle position but not the real particle size.).
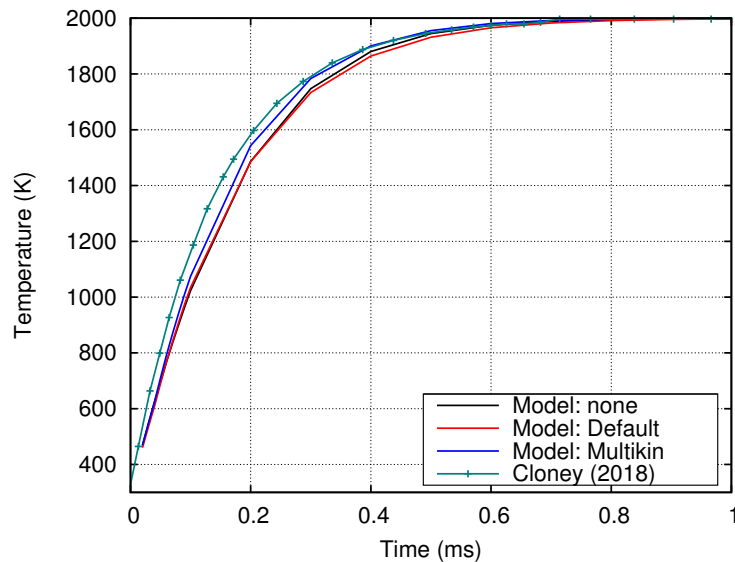
Figure 6.15: Temperature of a $10\mu m$ particle placed in a stationary gas at temperature of $2000K$. Three devolatilization models were used and compared with the results from Cloney [86].

The temperature profile of a $10\mu m$ particle immersed in $2000K$ air is

shown in Figure 6.15. In this regard, simulations were conducted without the devolatilization model, as well as using the default *singleKineticRateDevolatilization* and *MultiKineticRateDevolatilization* models. Notably, for all simulation cases, the time taken to reach a temperature of $2000K$ was approximately $0.8ms$.

It was found that the "multikin" model implemented in the simulation exhibited a higher temperature profile during the heating stage, which was more similar to the temperature profile obtained by Cloney [86]. The comparison results highlight the importance of considering the appropriate devolatilization model when evaluating the impact of particle heat exchange on the overall heat transfer process.

In order to explore the effect of devolatilization models on particle acceleration, a series of simulations were performed using the same geometry as in the previous chapter, but with an inlet velocity of $1m/s$. These simulations incorporated drag force and gravity, thereby enabling particle acceleration. Velocity profiles were compared between cases with and without the devolatilization model, and the findings are presented in Figure 6.16. Interestingly, it was found that the kinetic evolution of the evolved gas did not significantly affect the particle velocity profile, with the velocity profile remaining virtually unchanged regardless of whether the devolatilization model was present. Notably, it was observed that the evolved gas had an enhancing effect on particle acceleration, with the particles reaching gas velocity at approximately $0.6ms$. These results provide valuable insights into the influence of devolatilization models on particle acceleration, and suggest that considering evolved gas kinetics may enhance the acceleration process.
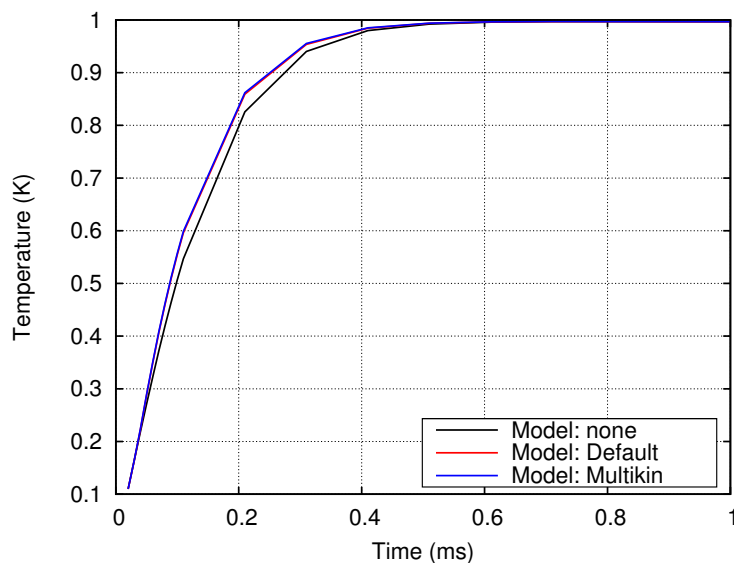
Figure 6.16: Analysis of temperature profile for a $10\mu m$ particle under constant air flow velocity ($1m/s$) using different devolatilization models.

6.6   Particle size analysis with new devolatilization model

6.6.1   One cell analysis

For the particle size analysis, the same geometry as used in the previous chapter was employed. Four different sizes of coal particles were placed in a stationary gas at a temperature of $2000K$. The temperature profile of the particles is depicted in Figure 6.17. Notably, as the size of the particle increased, the time taken by the particle to reach the gas temperature also increased. For instance, for particles with a diameter of $250\mu m$, it took approximately $0.25s$ for them to reach the gas temperature.
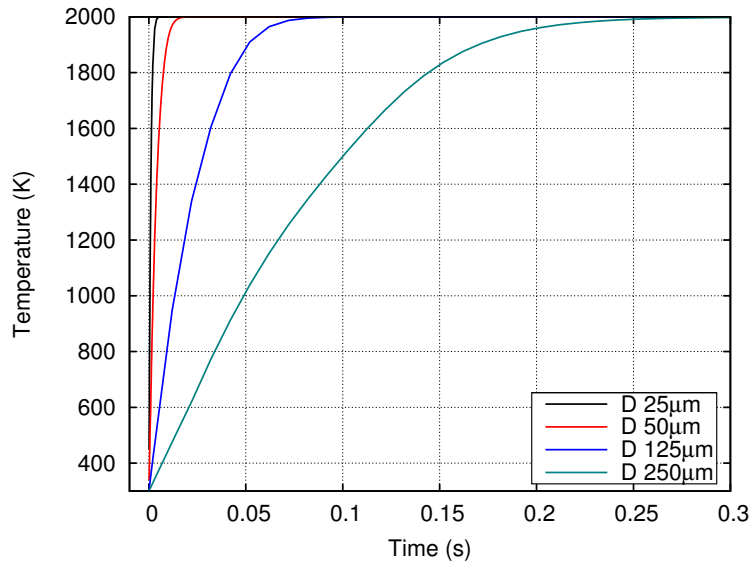
Figure 6.17: Temperature of single coal particle with $25\mu m$, $50\mu m$, $125\mu m$ and $250\mu m$ placed in a stationary gas at temperature of $2000K$. New devolatilization model *MultiKineticRateDevolatilization* is used.

Next, the evolved gas release was plotted in Figure 6.18, and it was observed that the difference in time was much smaller compared to the temperature. Specifically, the particle with a diameter of $25\mu m$ took approximately $0.6s$ to exhaust the total evolved gases, whereas the largest particle, $250\mu m$ in diameter, took approximately $0.7s$. It was also noted that the evolved gas was released rapidly until $0.3s$, after which the rates of release became smaller.

The detailed gas species evolution was plotted in Figure 6.19. The curves for different particle sizes were similar for each gas species. It was found that CH_4 and C_2H_4 were exhausted earlier than CO and CO_2.
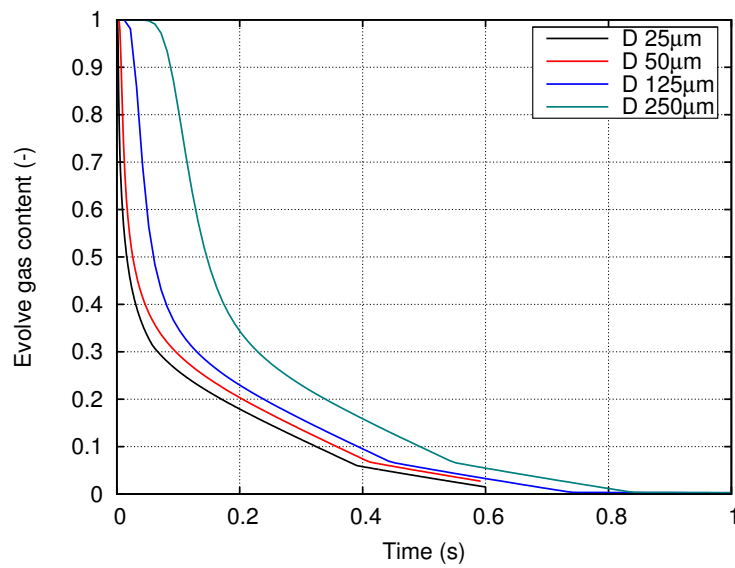
Figure 6.18: Evolve gas fraction of single coal particle with $25\mu m$, $50\mu m$, $125\mu m$ and $250\mu m$ placed in a stationary gas at temperature of $2000K$. New devolatilization model *MultiKineticRateDevolatilization* is used.
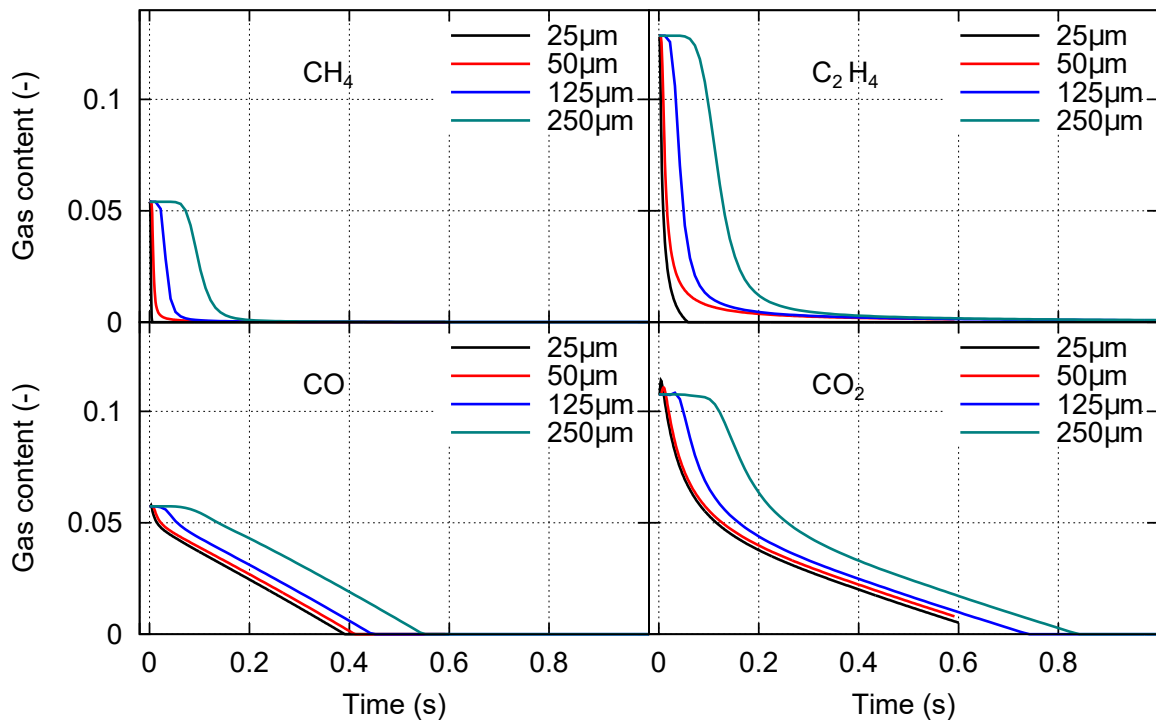
Figure 6.19: Detailed evolve gas specie fractions of single coal particle with $25\mu m$, $50\mu m$, $125\mu m$ and $250\mu m$ placed in a stationary gas at temperature of $2000K$. New devolatilization model *MultiKineticRateDevolatilization* is used.

6.6.2   2D explosion simulations

In this study, the same geometry as described in Chapter 6.3 is employed to conduct 2D simulations of a combustion system. However, in contrast to the previous study, we distribute the particles evenly throughout the domain to investigate the influence of particle size on the combustion process. To ensure the accuracy of the simulation, the particles are kept stationary for the first $0.01s$ to eliminate any expansion effects caused by the ignition sources in the simulation. This allows us to focus solely on the combustion process itself. To model the devolatilization process, we use two different models: the *constantRateDevolatilization* and *MultiKineticRateDevolatilization* models. The gas profiles at the height of the ignition source at $0.01s$ are then plotted in Figure 6.20-6.22, with the temperature plotted on the secondary axis.
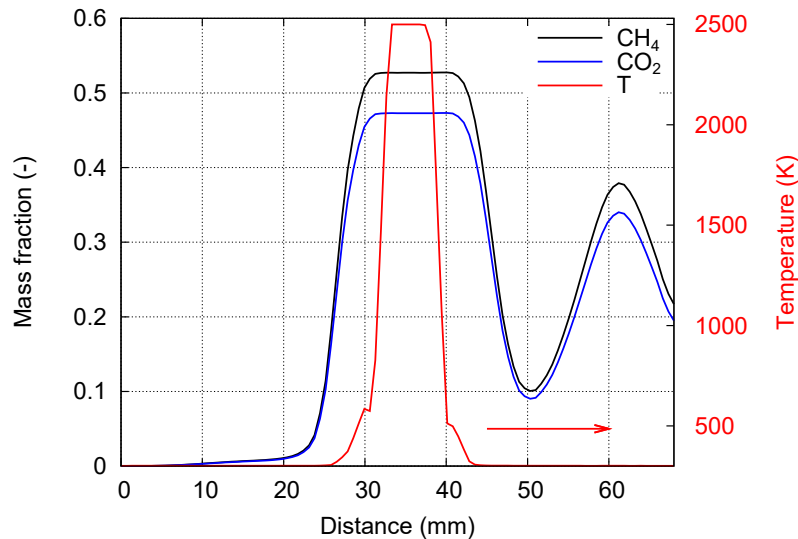
Figure 6.20: Profiles of gas species at the horizontal line at ignition height for a $25\mu m$ coal dust explosion flame at time $0.01s$ with stationary particles using the *constantRateDevolatilization* model.

From the figures, it is evident that the ignition source has a temperature of $2500K$, and it is clearly visible. The results obtained from this study provide valuable insights into the influence of particle size on the combustion process and demonstrate the importance of accurate modeling techniques in predicting combustion behavior.

Figure 6.20 used the *constantRateDevolatilization* model and the evolve gas specie is only CH_4. The mass fraction value reaches 0.5 near the ignition source and decreases over the explosion tube. On the right side, there is a fluctuation of the flow which results in a higher value of the detected gases. Similarly, the CH_4 mass fraction is plotted in Figure 6.21 of different coal particle sizes. From different particle sizes, the evolve gas mass fractions are almost the same with the default devolatilization model.
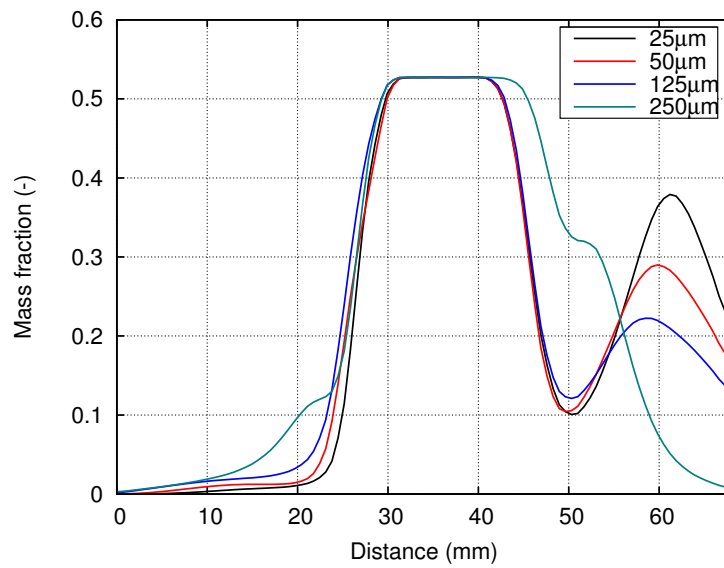
Figure 6.21: Comparison of CH_4 mass fraction of four different particle sizes at the height of the ignition source: $25\mu m$, $50\mu m$, $125\mu m$, and $250\mu m$ dust explosion. The devolatilization model used is *constantRateDevolatilization* .
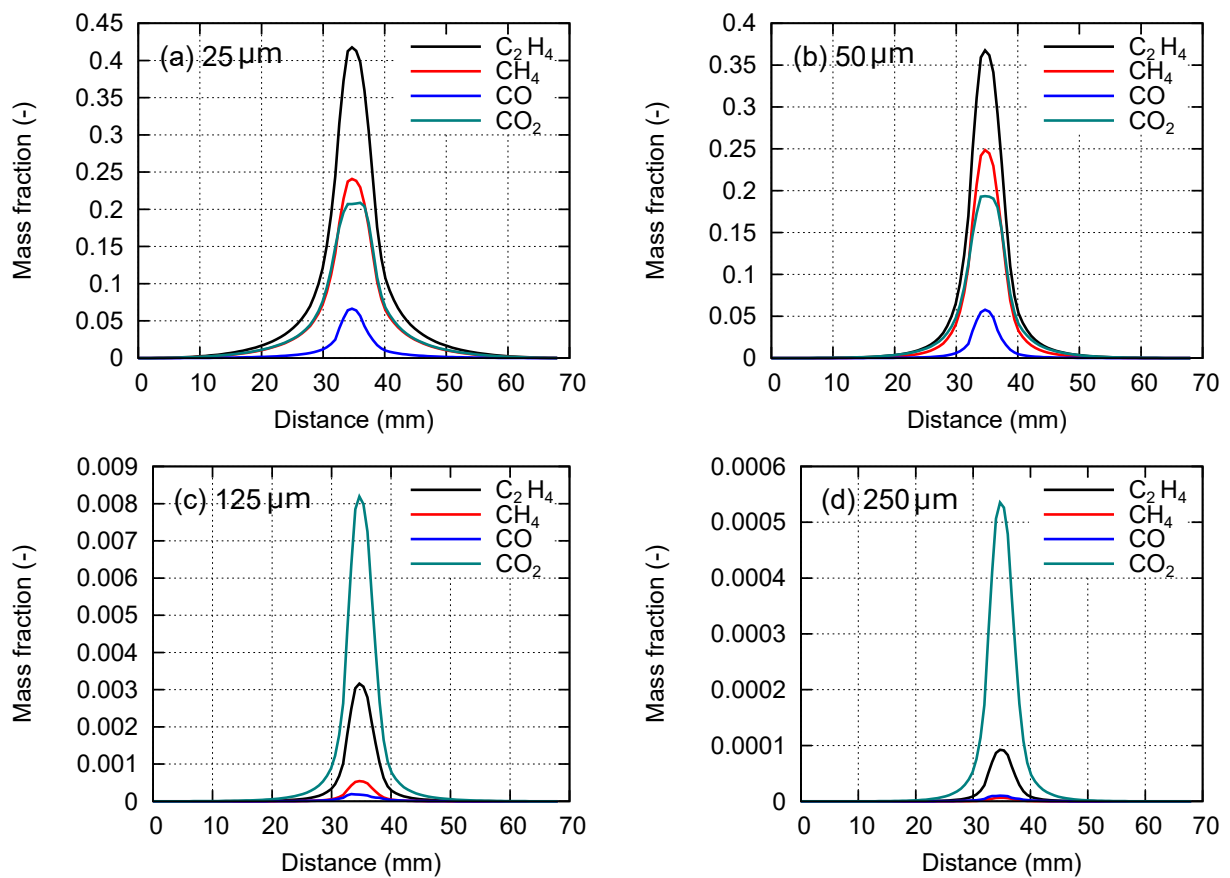
Figure 6.22: Gas species profiles for $25\mu m$, $50\mu m$, $125\mu m$, and $250\mu m$ coal dust explosion flame at time $0.01s$ at the horizontal line of the ignition source, where the particles are set as stationary. The devolatilization model used is *MultiKineticRateDevolatilization* .

Figure 6.22 used the multiKineticDevolatilization model and the evolve gas specie contains C_2H_4, CH_4, CO, and CO_2. The difference between each gas is obvious and there are less amount of combustible gases released compared to CO_2.
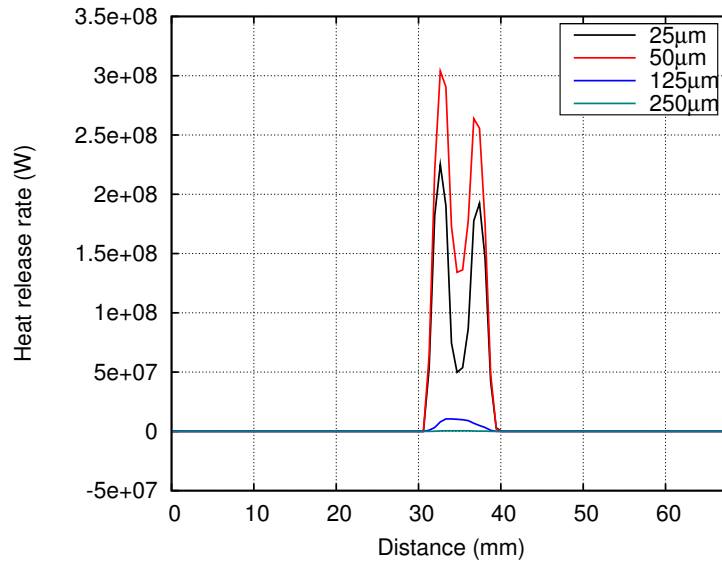
Figure 6.23: The heat release rate of dust explosion flame at 0.01 s for $25\mu m$, $50\mu m$, $125\mu m$, and $250\mu m$ coal at the horizontal line of the ignition source. The devolatilization model used is *MultiKineticRateDevolatilization* .
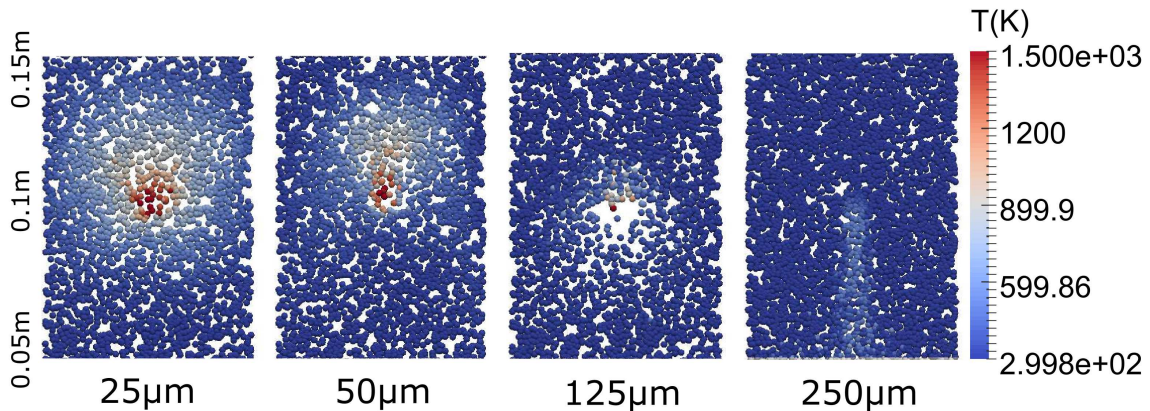
Figure 6.24: Comparison of parcel temperature at $0.01s$ of the dust explosion of four sizes of particles: $25\mu m$, $50\mu m$, $125\mu m$, and $250\mu m$.

The heat release rate from the chemical reactions is plotted in Figure 6.23 for four sizes of coal particles at $0.01s$. The horizontal line through the ignition source is observed. The reaction happens at the ignition source, where the temperature is $2500K$. Due to the different amounts of combustible gas released from the particles among the four sizes, the

heat release varies. It takes longer to start the reaction for $250\mu m$ particles. Therefore, the dust cloud with higher particle diameters is harder to ignite, and its minimum ignition energy is higher at the same dust concentration.
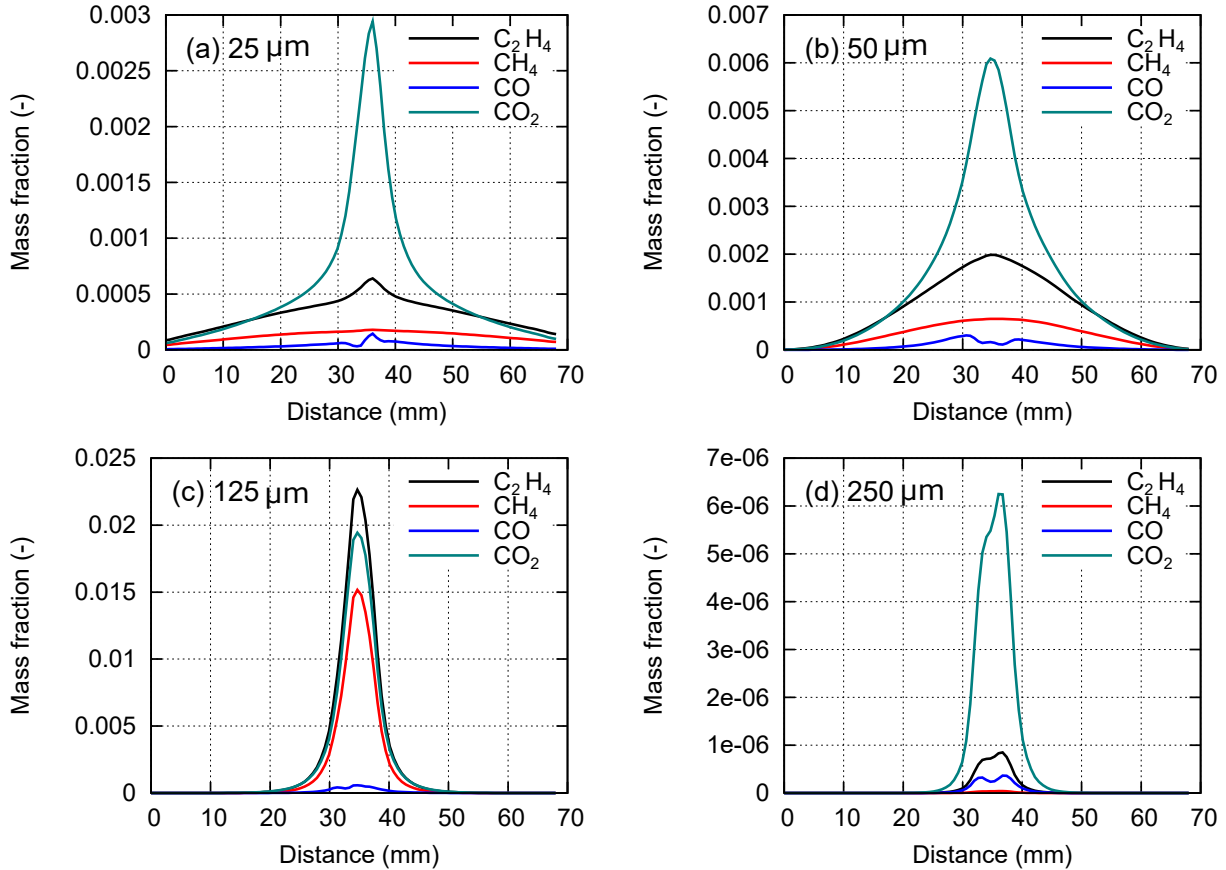
Figure 6.25: Gas species profiles for $25\mu m$, $50\mu m$, $125\mu m$, and $250\mu m$ coal dust explosion flame at time $0.01s$ at the horizontal line of ignition source, where the particles are not stationary. The devolatilization model used is *MultiKineticRateDevolatilization* .

A second test with activating particle gravity and drag force from the gas flow is also carried out. Due to the high ignition temperature, the particles fly outside when the gas expands. The parcel temperature around the ignition source is shown and compared in Figure 6.24 of different sizes of particles. The devolatilization model used is *MultiKineticRateDevolatilization* . Compared to Figure 6.21, the evolve gas mass fractions are about 1000 times lower (see Figure 6.25) because of the stimulation from the fluid transportation.

6.7 Summary

In this chapter, dust explosion studies were carried out. The explosion experiments of coal dust samples in the MIKE 3 apparatus were first carried out and compared with the simulations. The new devolatilization model developed from the previous chapter was implemented into OpenFOAM and tested.

The flame propagation of dust explosions with different particle sizes was studied in the MIKE 3 apparatus. The particle distribution in the instance of dust explosion was not consistent in each test. Therefore, the explosion flame shape development in the tube varies from case to case. However, the dust explosion flame in MIKE 3 develops horizontally and vertically until it reaches the wall and finally develops toward the tube openings. Flames are more likely to develop in areas with high dust concentrations. The dust distribution at the instance of the explosion was also studied. The positions of the dust cloud from 3 are used as further explosion studies. The results are compared with the simulation results using evenly distributed particle positions. Particles tend to be pushed away from the ignition source. The different unburnt particle concentrations lead to different flame speeds in the particle size groups. The simulation of the 3D simulation was also carried out. The flame is less vigorous since the turbulence at the initial boundary was excluded. However, the simulation predicts acceptable results in the flame temperature and the Lagrangian particles.

The new devolatilization model, *MultiKineticRateDevolatilization* , was further implemented in the OpenFOAM database. The increase of evolved gas number prompts the heat transfer between particle and gas phases. The prediction of gas evolvement in $25\mu m$, $50\mu m$, $125\mu m$, and $250\mu m$ particles was reasonable: the larger particles take longer time to decompose. In the 2D explosion simulations, the new model is able to describe the differences between the four gas evolvements, as well as the changes in particle sizes. The better prediction of the gas products improves the chemical reaction solutions in the dust explosion simulations.

Chapter 7

Conclusion and outlook

The overall objective of this thesis was to extend the current knowledge of particle deflagration regimes and their effect on the dust explosion simulation models. A computational fluid dynamics model was developed based on the open-source OpenFOAM toolkit. The model was constructed with the gas evolvement of the particle devolatilization and inner particle effect, for example, the porosity and the gas phase transport inside the particle. The Eulerian method was used, and the gas and solid phases were divided by the porosity of the particle. The single-particle model for the western coal particle was built up to explore the temperature gradient effect, which should be taken into consideration in the simulation. The following section presents the conclusions drawn from the current study, along with suggestions for future work.

The experimental equipment used in the study was MIKE 3, and its result was used to compare with the simulation work. In the dust dispersion studies, the particle size effect was explored in simulation and experimental methods. Seven particle sizes of coal dust were tested in the distribution tube with the dispersion nozzle. The propagation of dust front was tracked in the experiment, and no other measurement was added since the level of turbulence in the flow with the existence of particles is hard to be measured [134]. Future studies can focus on a larger experimental instrument, such as the 4-meter-long test rig constructed by Hüttenbrenner [135]. In addition, alternative dust-feeding systems can be tested and used in order to reduce the turbulence level before the explosion tests. The experimental results of the dust propagation velocity for different particle sizes are similar. Very slight differences are found between small and larger particles. A general trend of faster development of the coal cloud front was the conclusion of the dust dispersion experiments. The particle size effect and turbulence level are better observed in the simulation results. Two simulation geometries were tested: one is with a constant high-pressure air inlet, and the other is attached to a $50mL$ compressed air tank identical

to the experimental construction. The constant high-pressure air inlet results in a higher speed of particle propagation in the dust explosion tube. And the second geometry gives better predictions of dust propagation. However, the air velocity reaches $100m/s$ as it passes through the connecting pipe. As a result, the simulation requires a significant amount of computing resources and time to complete. Another replacement to simulate dust dispersion should be considered in future work. During the dispersion of the dust cloud, the high turbulence is concentrated at the lower part of the explosion tube, where vortices were identified. The high-speed nozzle is able to push the particles into the air efficiently but with high turbulence. The dust cloud is pushed to the tube wall initially and rebounds afterward. Due to the high turbulence and wall interactions, the dust cloud distribution inside the tube is not consistent and almost unpredictable. Nevertheless, the simulation results of three particle size groups ($25\mu m$, $125\mu m$, and $250\mu m$) showed distinct differences with the concentrations over the tube. The smaller particles which propagate faster have the highest concentration at the top of the tube at the time of spark ignition. Moreover, the highest concentration locations for larger particles are lower in the tube, which will result in the inaccurate test result of minimum ignition energy. Therefore, different ignition delay times should be adjusted according to the test sample sizes in order to achieve the most accurate test results.

The process of dust explosion is notably influenced by the size of the particles, with the flame propagation speed exhibiting an increase for smaller particles. This phenomenon can be attributed to the uneven distribution of particle concentrations across various size groups as well as the underlying chemical reactions. Furthermore, the smaller particles possess a larger surface-to-volume ratio, rendering them more prone to combustion [35, 136]. Both of these aspects were discussed in the study. Firstly, the uneven particle distribution from the dispersion nozzles was used as the initial condition of the dust explosion in the 2D simulations. The comparison of the explosion flame propagation showed a higher difference with $25\mu m$ and $125\mu m$ dust clouds. The dust explosion simulation in 3D geometry was also carried out. The results of explosion flame propagation, particle temperature, and movement agreed well with the experiments. However, the simulation took extensive work to achieve a combustion state, and only one was successful after more than 50 trials of different ignition sources. Various methods were employed to investigate ignition sources: larger ignition area ($2000K$), adding combustible gas methane/particles near the ignition source, different radiation models, and different schemes, removing the drag forces and gravity on particles. For example, the modifications were restrained to a relatively acceptable level by increasing the ignition box length from $5mm$ to $15mm$. The more problematic issue is from the particle-fluid coupling of the

Lagrangian method. Because the tube is too small ($300mm$ in height and $68mm$ in diameter), the particles quickly fly out of the simulation geometry. For larger geometries or test chambers with a different outlet, this is not a problem [137]. Furthermore, the high temperature of the ignition source heats the gas nearby and pushes the particles away, which makes it harder for the particles to decompose. Similar effects are also observed in [137]. The ignition source is usually treated in Lagrangian simulations as in our study, a high-temperature sphere source [138]. A comparison of simulation with such an ignition source and experiment with spark ignition would be interesting and can explain the deviations of the simplified ignition source.

The second aspect, chemical reactions of different sizes of particles, was studied in detail, and a new devolatilization model was developed. The default models simplify the models and have constant rates of reactions. Another consideration of the study is to explore if the temperature gradient inside of the particle results in a large influence on the evolvement of pyrolysis gases. Firstly, the TGA-FTIR analysis was used to obtain the pyrolysis characteristics of our sample. The inner pore effect is explored by a single-particle model by considering the pyrolysis stages. The boundary condition was carefully chosen to simulate the heat transfer between the particle and the hypothetical ignition source. The single-particle model used the Eulerian method. The porosity ξ was introduced to describe the pore expansion during the particle devolatilization. Different sets of physical properties were tested and compared in the simulations. A set of time-dependent variables was finally used. The simulation results showed that the temperature gradient inside of the coal particles whose diameter is smaller is $250\mu m$ can be ignored in the simulation of dust deflagration. A new devolatilization model using the four pyrolysis gases was developed. Further study can improve the experimental method to detect more pyrolysis gases from particle devolatilization. Furthermore, the existing model of devolatilization in OpenFOAM is limited. Other types of materials should also be tested in such a method to create a suitable devolatilization model.

The devolatilization model is finally tested in a one-cell geometry and 2D explosion simulation. The temperature prediction of the particle agrees well with the literature. Four pyrolysis gases were simulated and showed acceptable patterns. In the 2D dust explosion simulation model, four sizes of coal samples were used: $25\mu m$, $50\mu m$, $125\mu m$, and $250\mu m$. Compared to the default model, it takes longer to ignite the particle, and the largest particle, $250\mu m$, did not ignite. Nevertheless, the prediction of the evolved gases was promising. Unlike the default models, the new devolatilization model is sensitive to the particle size and predicts the gas evolvement according to the heating temperature and particle size. The larger particles have a smaller evolved gas fraction. It is because

of fewer particle/parcel numbers in the simulation and longer heating time. Difficulties, as mentioned above, are also found to simulate in 3D simulations. The suggestion is to use larger geometries to do further 3D research. Moreover, one more possibility is that the model could improve the simulation study on determining minimum ignition energy.

Bibliography

[1] T. Abbasi, S. Abbasi, Dust explosions–cases, causes, consequences, and control, Journal of hazardous materials 140 (1-2) (2007) 7–44.

[2] G. Li, H. X. Yang, C. M. Yuan, R. Eckhoff, A catastrophic aluminium-alloy dust explosion in china, Journal of loss prevention in the process industries 39 (2016) 121–130.

[3] M. Faraday, C. Lyell, Report on the explosion at the haswell collieries, and on the means of preventing similar accidents, Philosophical Magazine 26 (1845) 16–35.

[4] D. J. Price, H. H. Brown, H. R. Brown, H. E. Roethe, Dust explosions: theory and nature of, phenomena, causes and methods of prevention, National fire protection association, 1922.

[5] H. Kern, Explosible dust/air mixtures–investigations on flame propagation under non atmospheric conditions, Ph.D. thesis, Dissertation, Montanuniversität Leoben, Leoben (2013).

[6] Z. Yuan, N. Khakzad, F. Khan, P. Amyotte, Dust explosions: A threat to the process industries, Process Safety and Environmental Protection 98 (2015) 57–71.

[7] C. J. Hexamer, Dust explosions in breweries, Journal of the Franklin Institute 115 (2) (1883) 121–126.

[8] H. An, Computer-aided applications in process plant safety, Loughborough University, 2010.

[9] H. Guo, E. Scheepbouwer, T. Yiu, V. Gonzalez, Overview and analysis of digital technologies for construction safety management (2017).

[10] Z. Hongming, Flame propagation behavior and inerting suppression characteristics of starch dust deflagration in pipeline., Ph.D. thesis, Wuhan University of Technology (2018).

[11] S. Hosseinzadeh, M. Vanierschot, F. Norman, F. Verplaetsen, J. Berghmans, Flame propagation and flow field measurements in a hartmann dust explosion tube, Powder Technology 323 (2018) 346–356.

[12] P. R. Amyotte, R. K. Eckhoff, Dust explosion causation, prevention and mitigation: An overview, Journal of Chemical Health and Safety 17 (1) (2010) 15–28. doi:10.1016/j.jchas.2009.05.002.

[13] A. E1226-12a, Standard test method for explosibility of dust clouds, ASTM Int (2012) 1–13.

[14] E. 14034-2:2006+A1:2011, Determination of explosion characteristics of dust clouds-part 2: Determination of the maximum rate of explosion pressure rise (dp/dt)max of dust clouds, ASTM Int.

[15] A. E. 1515-14, Standard test method for minimum explosible concentration of combustible dusts, ASTM Int.

[16] A. E.2019-03, Standard test method for minimum ignition energy of a dust cloud in air, ASTM Int.

[17] A. E1491-06, Standard test method for minimum autoignition temperature of dust clouds, ASTM Int.

[18] D. A. Crowl, J. F. Louvar, Chemical process safety: Fundamentals with applications, 3rd Edition, Prentice Hall, 2011.

[19] C. AG, T. S. S. AG, K. AG, Mike 3, 20l siwek ball. (2022).
URL https://www.tuvsud.com/en-gb/country/switzerland/testing-equipment/20l-siwek-sphere-mike-3

[20] H. R. Brown, R. L. Hanson, Venting dust explosions, NFPA Quarterly 26 (1933) 328–341.

[21] H. P. Greenwald, R. V. Wheeler, Coal dust explosions: The effect of pressure on their development (1925).

[22] C. Kauffman, Agricultural dust explosions in grain handling facilities, Fuel-air Explosions, University of Waterloo Press, Waterloo, Ontario, Canada (1982) 305–347.

[23] A. E. Dahoe, Dust explosions: a study of flame propagation (2000).

[24] A. Dahoe, R. Cant, B. Scarlett, On the decay of turbulence in the 20-liter explosion sphere, Flow, turbulence and combustion 67 (3) (2001) 159–184.

[25] V. Di Sarli, P. Russo, R. Sanchirico, A. Di Benedetto, Cfd simulations of dust dispersion in the 20 l vessel: Effect of nominal dust concentration, Journal of Loss Prevention in the Process Industries 27 (2014) 8–12.

[26] Z. Dyduch, T. Skjold, An assessment of the laminar burning velocity in dust/air mixtures based on a model for dust explosions in closed 20-litre vessels, in: Eighth International Symposium on Hazards, Prevention and Mitigation of Industrial Explosions, 2010.

[27] Y. K. Pu, J. Jarosinski, C. S. Tai, C. W. Kauffman, M. Sichel, The investigation of the feature of dispersion induced turbulence and its effects on dust explosions in closed vessels, in: Symposium (International) on Combustion, Vol. 22, Elsevier, 1989, pp. 1777–1787.

[28] C. Murillo, N. Bardin-Monnier, C. Blanchard, D. Funfschilling, F. Munoz, N. Rios, D. Vizcaya, Cfd to improve the repeatability and accuracy of dust explosion tests in the 20-liters sphere, Chemical Engineering Transactions 48 (2016) 115–120.

[29] A. A. Pekalski, Theoretical and experimental study on explosion safety of hydrocarbons oxidation at elevated conditions: Relevance for safe design and operation of industrial processes (2004).

[30] T. Skjold, Selected aspects of turbulence and combustion in 20-litre explosion vessels: development of experimental apparatus and experimental investigation, Ph.D. thesis, The University of Bergen (2003).

[31] W. Pollhammer, C. Spijker, H. Kern, H. Raupenstrauch, Development of a dust dispersion system for investigation on reduced pressure conditions in the 20-liter siwek apparatus using openfoam, in: W. Gao (Ed.), Proceedings of the 11th International Symposium of Hazards, Prevention, and Mitigation of Industrial Explosions, Dalian University of Technology, Dalian, 2016, pp. 275–286.

[32] O. Kalejaiye, P. R. Amyotte, M. J. Pegg, K. L. Cashdollar, Effectiveness of dust dispersion in the 20-l siwek chamber, Journal of loss prevention in the process industries 23 (1) (2010) 46–59.

[33] J. E. Going, K. Chatrathi, K. L. Cashdollar, Flammability limit measurements for dusts in 20-l and 1-m3 vessels, Journal of Loss Prevention in the Process Industries 13 (3-5) (2000) 209–219.

[34] F. A. Williams, Combustion theory, CRC Press, 2018.

[35] R. K. Eckhoff, Dust explosions in the process industries: identification, assessment and control of dust hazards, elsevier, 2003.

[36] M. Horton, F. Goodson, L. Smoot, Characteristics of flat, laminar coal-dust flames, Combustion and Flame 28 (1977) 187–195.

[37] Y. Huang, G. A. Risha, V. Yang, R. A. Yetter, Combustion of bimodal nano/micron-sized aluminum particle dust in air, Proceedings of the Combustion Institute 31 (2) (2007) 2001–2009.

[38] C. Proust, A few fundamental aspects about ignition and flame propagation in dust clouds, Journal of Loss Prevention in the Process Industries 19 (2-3) (2006) 104–120.

[39] J. Sun, R. Dobashi, T. Hirano, Structure of flames propagating through aluminum particles cloud and combustion process of particles, Journal of loss prevention in the process industries 19 (6) (2006) 769–773.

[40] A. Y. Chowdhury, H. G. Johnston, B. Marks, M. S. Mannan, E. L. Petersen, Effect of shock strength on dust entrainment behind a moving shock wave, Journal of Loss Prevention in the Process Industries 36 (2015) 203–213.

[41] R. Klemens, P. Zydak, M. Kaluzny, D. Litwin, P. Wolanski, Dynamics of dust dispersion from the layer behind the propagating shock wave, Journal of Loss Prevention in the Process Industries 19 (2-3) (2006) 200–209.

[42] R. W. Houim, S. L. O. Ugarte, E. S. Oran, Mechanism of dust scouring behind shock waves, in: W. Gao (Ed.), Proceedings of the 11th International Symposium of Hazards, Prevention, and Mitigation of Industrial Explosions, Dalian University of Technology, Dalian, 2016, pp. 188–202.

[43] R. W. Houim, E. S. Oran, Structure and flame speed of dilute and dense layered coal-dust explosions, Journal of Loss Prevention in the Process Industries 36 (2015) 214–222.

[44] R. W. Houim, E. S. Oran, Numerical simulation of dilute and dense layered coal-dust explosions, Proceedings of the Combustion Institute 35 (2) (2015) 2083–2090.

[45] T. Kanno, K. Asano, A. Matsuo, Numerical simulation of layered coal-dust explosions based on euler-lagrange approach, in: W. Gao (Ed.), Proceedings of the 11th International Symposium of Hazards, Prevention, and Mitigation of Industrial Explosions, Dalian University of Technology, Dalian, 2016, pp. 410–421.

[46] P. Zydak, R. Klemens, Modelling of dust lifting process behind propagating shock wave, Journal of Loss Prevention in the Process Industries 20 (4-6) (2007) 417–426.

[47] Y.-C. Li, A. Harbaugh, C. Alexander, C. Kauffman, M. Sichel, Deflagration to detonation transition fueled by dust layers, Shock Waves 5 (4) (1995) 249–258.

[48] P. Julien, S. G. J. Vickery, J. M. Bergthorson, D. L. Frost, Intrinsic instabilities in dust flames, in: W. Gao (Ed.), Proceedings of the 11th International Symposium of Hazards, Prevention, and Mitigation of Industrial Explosions, Dalian University of Technology, Dalian, 2016, pp. 338–348.

[49] J. Droujko, P. Julien, M. Soo, S. Goroshin, J. Bergthorson, D. Frost, N. Glumac, The role of radiative preheating on flame propagation in aluminum dust clouds, in: Proceedings of the 11th International Symposium on Hazards, Prevention, and Mitigation of Industrial Explosions, 2016, pp. 435–448.

[50] D. Castellanos, A. Lewandowski, A. Diaz, A. F. Mejia, V. Carreto, C. Mashuga, A. S. Rangwala, Z. Cheng, M. S. Mannan, Influence of particle size and crystalline level on the efficiency of dust explosion inhibitors, Industrial & Engineering Chemistry Research 53 (28) (2014) 11527–11537.

[51] W. Gao, T. Mogi, J. Sun, J. Yu, R. Dobashi, Effects of particle size distributions on flame propagation mechanism during octadecanol dust explosions, Powder technology 249 (2013) 168–174.

[52] S. R. Rockwell, A. S. Rangwala, Modeling of dust air flames, Fire safety journal 59 (2013) 22–29.

[53] O.-S. Han, M. Yashima, T. Matsuda, H. Matsui, A. Miyake, T. Ogawa, A study of flame propagation mechanisms in lycopodium dust clouds based on dust particles' behavior, Journal of Loss Prevention in the Process Industries 14 (3) (2001) 153–160. doi:10.1016/S0950-4230(00)00049-8.

[54] W. Gao, T. Mogi, J. Yu, X. Yan, J. Sun, R. Dobashi, Flame propagation mechanisms in dust explosions, Journal of loss prevention in the process industries 36 (2015) 186–194.

[55] P. Daoutidis, W. Alex Marvin, Srinivas Rangarajan, A. I. T., Practical methods for measuring the tortuosity of porous materials from binary or gray-tone tomographic reconstructions, AIChE Journal 59(8) (2012) 3–18.

[56] M. Hertzberg, K. L. Cashdollar, I. A. Zlochower, Flammability limit measurements for dusts and gases: ignition energy requirements and pressure dependences, in: Symposium (international) on combustion, Vol. 21, Elsevier, 1988, pp. 303–313.

[57] R. Pilao, E. Ramalho, C. Pinho, Influence of initial pressure on the explosibility of cork dust/air mixtures, Journal of Loss Prevention in the Process Industries 17 (1) (2004) 87–96.

[58] W. Wiemann, Influence of temperature and pressure on the explosion characteristics of dust/air and dust/air/inert gas mixtures, in: Industrial dust explosions, ASTM International, 1987.

[59] R. K. Eckhoff, Scaling of dust explosion violence from laboratory scale to full industrial scale–a challenging case history from the past, Journal of Loss Prevention in the Process Industries 36 (2015) 271–280.

[60] A. Klippel, M. Scheid, U. Krause, Investigations into the influence of dustiness on dust explosions, Journal of Loss Prevention in the Process Industries 26 (6) (2013) 1616–1626.

[61] A. Klippel, M. Schmidt, O. Muecke, U. Krause, Dust concentration measurements during filling of a silo and cfd modeling of filling processes regarding exceeding the lower explosion limit, Journal of loss prevention in the process industries 29 (2014) 122–137.

[62] S. Rani, B. Aziz, J. Gimbun, Analysis of dust distribution in silo during axial filling using computational fluid dynamics: Assessment on dust explosion likelihood, Process safety and environmental protection 96 (2015) 14–21.

[63] T. Allen, Particle size measurement, Springer, 2013.

[64] Y. Wakatsuki, T. Ueda, Y. Nakamura, T. Murase, Particle size effects in metal dust combustion, Combustion and Flame 135 (1-2) (2003) 155–161. doi:10.1016/S0010-2180(03)00153-9.

[65] S. Alavi, D. L. Thompson, Molecular dynamics simulations of the melting of aluminum nanoparticles, The Journal of Physical Chemistry A 110 (4) (2006) 1518–1523.

[66] J. Yu, X. Zhang, Q. Zhang, L. Wang, K. Ji, L. Peng, W. Gao, Combustion behaviors and flame microstructures of micro-and nano-titanium dust explosions, Fuel 181 (2016) 785–792.

[67] R. Dobashi, Risk of dust explosions of combustible nanomaterials 170 (1) (2009) 012029.

[68] M. Mittal, Explosion characteristics of micron-and nano-size magnesium powders, Journal of Loss Prevention in the Process Industries 27 (2014) 55–64.

[69] S. P. Boilard, P. R. Amyotte, F. I. Khan, A. G. Dastidar, R. K. Eckhoff, Explosibility of micron-and nano-size titanium powders, Journal of Loss Prevention in the Process Industries 26 (6) (2013) 1646–1654.

[70] C. K. Man, M. L. Harris, Participation of large particles in coal dust explosions, Journal of Loss Prevention in the Process Industries 27 (2014) 49–54.

[71] P. Wypych, D. Cook, P. Cooper, Controlling dust emissions and explosion hazards in powder handling plants, Chemical Engineering and Processing: Process Intensification 44 (2) (2005) 323–326.

[72] R. K. Eckhoff, Understanding dust explosions. the role of powder science and technology, Journal of Loss Prevention in the Process Industries 22 (1) (2009) 105–116.

[73] Y. Yuzuriha, W. Gao, T. Mogi, R. Dobashi, Effects of particle size distributions on flame propagation behavior through dust clouds of pmma, Journal of Loss Prevention in the Process Industries 49 (2017) 852–858.

[74] X. Zhang, J. Yu, W. Gao, D. Zhang, J. Sun, S. Guo, R. Dobashi, Effects of particle size distributions on pmma dust flame propagation behaviors, Powder technology 317 (2017) 197–208.

[75] OpenCFD, The open source computational fluid dynamics (cfd) toolbox (2020).

[76] J. Anderson, Computational Fluid Dynamics, Computational Fluid Dynamics: The Basics with Applications, McGraw-Hill Education, 1995.

136

[77] S. B. Pope, Turbulent flows, Cambridge University Press 1 (2000) 197–217.
URL https://doi.org/10.1017/CBO9780511840531

[78] R. L. Spalart, J. K. Allmaras, A generalized k-epsilon model for turbulent flows near walls, Tech. rep., NASA (1992).

[79] S. Zhong, A. Teodorczyk, X. Deng, J. Dang, Modeling and simulation of coal dust explosions, in: Journal de Physique IV (Proceedings), Vol. 12, EDP sciences, 2002, pp. 141–147.

[80] C. G. Veras, J.Saastamoinen, J. C. JR., M. Aho, Overlapping of the Devolatilization and Char Combustion Stages in the Burning of Coal Particles, Combustion and Flame 579 (1999) 567–579.

[81] C. Spijker, H. Raupenstrauch, Numerical investigation on inner particle effects in lycopodium/air dust deflagrations, Journal of Loss Prevention in the Process Industries 49 (2017) 870–879.

[82] P. C. Carman, Fluid flow through granular beds, Transactions of the Institution of Chemical Engineers 15 (1937) 150–166.

[83] W. Pollhammer, C. Spijker, H. Kern, H. Raupenstrauch, Numerical investigation on minimum ignition energy and flame propagation in dust/air-mixtures by using lagrangian model in openfoam, in: W. Gao (Ed.), Proceedings of the 11th International Symposium of Hazards, Prevention, and Mitigation of Industrial Explosions, Dalian University of Technology, Dalian, 2016, pp. 516–529.

[84] C. Spijker, H. Kern, H. Raupenstrauch, Held Kerstin, Modeling dust explosions, in: AIChE Annual Meeting, 2013.

[85] S. Tomasch, Numerical investigation of the interaction between dust explosions and inert particulate additives using an euler-lagrangian approach in openfoam, Master's dissertation, Montanuniversität, Austria (2016).

[86] C. T. Cloney, R. C. Ripley, M. J. Pegg, P. R. Amyotte, Laminar burning velocity and structure of coal dust flames using a unity lewis number cfd model, Combustion and Flame 190 (2018) 87–102.

[87] C. Spijker, H. Kern, H. Raupenstrauch, A model for dust deflagrations, considering inner particle transport effects, in: 17th International Conference on Numerical Combustion, 2019.

[88] H. Katja, K. Hannes, D. Claudia, R. Harald, Investigations on the influence of the specific surface on the ignition and flame behavior of combustible dust/air-mixtures, in: Brochure of 11th International Symposium on Hazards, Prevention, and Mitigation of Industrial Explosions, 2016.

[89] T. Skjold, Flame propagation in dust clouds. numerical simulation and experimental investigation (2014).

[90] T. Skjold, Simulating the effect of release of pressure and dust lifting on coal dust explosions, Flame propagation in dust clouds. Numerical simulation and experimental investigation (2007).

[91] J. Zhang, P. Xu, L. Sun, W. Zhang, J. Jin, Factors influencing and a statistical method for describing dust explosion parameters: A review, Journal of Loss Prevention in the Process Industries 56 (May) (2018) 386–401. doi:10.1016/j.jlp.2018.09.005.

[92] Y. Pan, C. Spijker, H. Raupenstrauch, Cfd modeling of particle dispersion behavior in the mike 3 apparatus, Alexandria Engineering Journal 61 (12) (2022) 9305–9313. doi:10.1016/j.aej.2022.03.039.

[93] C. Cesana, R. Siwek, Manual MIKE 3 apparatus, Kuehner AG, Switzerland (2010).

[94] T. Schindler, W. Beckmann, Development of an improved hartmann tube for studying dust explosions, Journal of Loss Prevention in the Process Industries 4 (3) (1991) 179–187. doi:10.1016/0950-4230(91)87002-E.

[95] C. Murillo, O. Dufaud, N. Bardin-Monnier, O. López, F. Munoz, L. Perrin, Dust explosions: Cfd modeling as a tool to characterize the relevant parameters of the dust dispersion, Chemical Engineering Science 104 (2013) 103–116.

[96] S. A. Morsi, A. J. Alexander, An investigation of particle trajectories in two-phase flow systems, Journal of Fluid Mechanics 55 (2) (1972) 193–208. doi:10.1017/S0022112072001806.

[97] Y. Pan, C. Spijker, H. Raupenstrauch, Investigations on the effect of particle size on dust dispersion in mike 3 apparatus, in: Proceedings of 13th International Symposium on Hazards, Prevention, and Mitigation of Industrial Explosions (13th ISHPMIE), 2020.

[98] C. Murillo, O. Dufaud, N. Bardin-Monnier, O. López, F. Munoz, L. Perrin, Dust explosions: Cfd modeling as a tool to characterize the relevant parameters of the dust dispersion, Chemical Engineering Science 104 (2013) 103–116.

[99] Y. Pan, C. Spijker, H. Raupenstrauch, Investigations on the effect of particle size on dust dispersion in mike 3 apparatus, in: Proceedings of 13th International Symposium on Hazards, Prevention, and Mitigation of Industrial Explosions (13th ISHPMIE), 2020.

[100] P. R. Amyotte, K. J. Mintz, M. Pegg, Y. Sun, Examination of the explosion characteristics of methane/coal dust/air mixtures (Jan 1989).

[101] D. K. Seo, S. S. Park, J. Hwang, T.-U. Yu, Study of the pyrolysis of biomass using thermo-gravimetric analysis (tga) and concentration measurements of the evolved species, Journal of Analytical and Applied Pyrolysis 89 (1) (2010) 66–73.

[102] C. Di Blasi, Kinetic and Heat Transfer Control in the Slow and Flash Pyrolysis of Solids, Industrial and Engineering Chemistry Research 35 (1) (1996) 37–46. doi: 10.1021/ie950243d.

[103] J. L. White, R. L. Braun, Thermal decomposition of coal, Kirk-Othmer Encyclopedia of Chemical Technology (2001). doi:10.1002/0471238961. 0313010112031815.a01.pub2.

[104] Y. Pan, C. Spijker, H. Raupenstrauch, TGA-FTIR for kinetic and evolved gas analysis of the coal particles in dust deflagration, in: Proceedings of 13th International Symposium on Hazards, Prevention, and Mitigation of Industrial Explosions (ISHPMIE 2022), Braunschweig, Germany, 2022, pp. 95–111. doi: 10.7795/810.20221124.

[105] S. Li, N. Whitely, W. Xu, W.-P. Pan, Characterization of coal by thermal analysis methods (2005).

[106] M. Cai, R. Smart, Quantitative analysis of n-methyl-2-pyrrolidinone in coal extracts by tga-ftir, Energy & fuels 7 (1) (1993) 52–56.

[107] Q. Cheng, B. Via, J. Wang, J. Zondlo, Primary study of woody biomass and coal for energy production investigated by tga-ftir analysis, BioResources 9 (2) (2014) 2899–2906.

[108] P. L. King, T. W. Vennemann, J. R. Holloway, R. L. Hervig, J. B. Lowenstern, J. F. Forneris, Analytical techniques for volatiles: A case study using intermediate (andesitic) glasses, American Mineralogist 87 (8-9) (2002) 1077–1089. `doi:10.2138/am-2002-8-904`.

[109] F. Kittinger, Simultanthermoanalyse mit ftir gasanalyse, (2019).

[110] H. Zheng, W. Wang, R. Xu, R. Zan, J. Schenk, Z. Xue, Effect of the particle size of iron ore on the pyrolysis kinetic behaviour of coal-iron ore briquettes, Energies 11 (10) (2018) 1–16. `doi:10.3390/en11102595`.

[111] M. Hertzberg, K. Cashdollar, Review of coal pulverizer fire and explosion incidents, Report COAL-82, Energy Research Foundation, Inc. (1987).

[112] M. Dong, C. Zheng, S. Miao, Y. Zhang, Q. Du, Y. Wang, F. K. Tittel, Development and measurements of a mid-infrared multi-gas sensor system for CO, CO2 and CH4 detection, Sensors (Switzerland) 17 (10) (2017). `doi:10.3390/s17102221`.

[113] W. Ranz, Marshall, Evaporation from drops, Chemical Engineering Progress 48 (1952) 141–146.

[114] K. Wittig, P. Nikrityuk, A. Richter, Drag coefficient and Nusselt number for porous particles under laminar flow conditions, International Journal of Heat and Mass Transfer 112 (2017) 1005–1016. `doi:10.1016/j.ijheatmasstransfer.2017.05.035`.

[115] A. Abou-Taouk, I. R. Sigfrid, R. Whiddon, L. E. Eriksson, A four-step global reaction mechanism for CFD simulations of flexi-fuel burner for gas turbines, Proceedings of the International Symposium on Turbulence, Heat and Mass Transfer 2012-Septe (2012) 616–627. `doi:10.1615/ICHMT.2012.ProcSevIntSympTurbHeatTransfPal.660`.

[116] J. Tomeczek, H. Palugniok, Specific heat capacity and enthalpy of coal pyrolysis at elevated temperatures, Fuel 75 (9) (1996) 1089–1093. `doi:10.1016/0016-2361(96)00067-1`.

[117] G. D. Badzioch S, Field MA, Investigation of temperature variation of thermal conductivity and thermal diffusivity of coal, Fuel 43 (4) (1964) 267–272.

[118] H. G. Weller, G. Tabor, H. Jasak, C. Fureby, A tensorial approach to computational continuum mechanics using object-oriented techniques, Computers in Physics 12 (6) (1998) 620. doi:10.1063/1.168744.

[119] Gschaider, Groovy boundary conditions for openfoam (2009).

[120] E. N. Fuller, P. D. Schettler, J. C. Giddings, New method for prediction of binary gas-phase diffusion coefficients, Industrial & Engineering Chemistry 58 (5) (1966) 18–27.

[121] V. Wärmeatlas, B. für den Wärmeübergang, Verein deutscher ingenieure–7. erweiterte auflage, düsseldorf (1994).

[122] Z. Liu, S. Hong, S. Zhang, S. Lin, L. Qiu, S. Xia, R. Zhang, J. Qian, Experimental investigations on explosion behaviors of large-particle and formation rules of gas residues, Journal of Loss Prevention in the Process Industries 46 (2017) 37–44. doi:10.1016/j.jlp.2017.01.016.

[123] Y. Pan, C. Spijker, H. Raupenstrauch, Numerical investigations on dust explosion process in mike 3 apparatus, in: Proceedings of 10th International Seminar on Fire and Explosion Hazards (ISFEH10), Oslo, Norway, 2022, pp. 56–64.

[124] Y. Pan, C. Spijker, H. Raupenstrauch, Investigation on flame propagation and particle decomposition behavior of dust explosion in mike 3 apparatus, in: Proceedings of 14th International Symposium on Hazards, Prevention, and Mitigation of Industrial Explosions (ISHPMIE 2022), Braunschweig, Germany, 2022, pp. 86–94.

[125] M. M. BAUM, P. J. STREET, Predicting the combustion behaviour of coal particles, Combustion Science and Technology 3 (5) (1971) 231–243. doi:10.1080/00102207108952290.

[126] J. Chomiak, Combustion a study in theory, fact and application (1990).

[127] A. Vdovin, A. Gonzalez, Radiation heat transfer in openfoam (2009).

[128] R. Tonoue, M. Katsura, M. Hamamoto, H. Bessho, S. Nakashima, A method to obtain the absorption coefficient spectrum of single grain coal in the aliphatic c–h stretching region using infrared transflection microspectroscopy, Applied spectroscopy 68 (7) (2014) 733–739.

[129] W. Pollhammer, C. Spijker, H. Kern, H. Raupenstrauch, Numerical investigation on heat transport while the ignition process of a dust / air mixture (October) (2015) 2–6.

[130] P. Cheng, Two-dimensional radiating gas flow by a moment method, AIAA journal 2 (9) (1964) 1662–1664.

[131] R. Siegel, J. R. Howell, Thermal radiation heat transfer, hemisphere pub, Corp., Washing ton DC (1992).

[132] Potentially explosive atmospheres, explosion prevention and protection, determination ofminimum ignition energy ofdust/air mixtures, Standard, European Standard, Brussels (2003).

[133] K. Hannes, W. Gerald J., R. Harald, Flame propagation in lycopodium/air mixtures below atmospheric pressure, Journal of Loss Prevention in the Process Industries 36 (2015) 281–286.

[134] T. Skjold, Selected aspects of turbulence and combustion in 20-Litre explosion vessels: Development of Experimental Apparatus and Experimental Investigation, Ph.D. thesis, University of Bergen (2003).

[135] K. Hüttenbrenner, H. Kern, F. Toth, J. Glechner, H. Raupenstrauch, Construction of a 4 m long test rig for experimental investigations on flame propagation in combustible dust / air mixtures, in: Proceedings of 13th International Symposium on Hazards, Prevention, and Mitigation of Industrial Explosions (13th ISHPMIE), 2020.

[136] M. Mittal, Explosion characteristics of micron- and nano-size magnesium powders, Journal of Loss Prevention in the Process Industries 27 (1) (2014) 55–64. `doi: 10.1016/j.jlp.2013.11.001`.

[137] W. R. Pollhammer, Masterarbeit: Numerische Untersuchung der Mindestzündenergie , sowie der Flammenfortpflanzung in Staub / Luft – Gemischen mittels eines Euler – Lagrange – Modells in OpenFOAM, Ph.D. thesis, Montanuniversitaet Leoben (2014).

[138] D. Ogungbemide, M. P. Clouthier, C. Cloney, Numerical modelling of the effects of vessel length-to-diameter ratio (L / D) on pressure piling (2020).

Appendix A

Boundary conditions

A.1 groovyBC

```
1  boundaryField
2  {
3      movingWall
4      {
5          type groovyBC;
6          gradientExpression "0";
7          valueExpression "1000";   //Tests 5-1.
8          fractionExpression "1";   //Dirichlet (1), Neumann (0).
9          value uniform 273;
10     }
```

Listing A.1: Groovy BC: Neumann 1000 K

```
1  boundaryField
2  {
3      movingWall
4      {
5          type groovyBC;
6          gradientExpression "10"; // Tests 5-2: 10; Tests 5-3: 100.
7          valueExpression "0";
8          fractionExpression "0";   //Dirichlet (1), Neumann (0).
9          value uniform 273;
10     }
```

Listing A.2: Groovy BC: gradient

```
1  boundaryField
2  {
```

```
3      movingWall
4      {
5         type groovyBC;
6         gradientExpression "-(Temp-Tinf)*coeff"
7         valueExpression "0";
8         fractionExpression "0";
9         variables "coeff=100; Temp=T; Tinf=1000";
10        value uniform 273;
11     }
```

Listing A.3: Groovy BC: function

```
1  boundaryField
2  {
3      aus
4      {
5      type                groovyBC;
6      variables  (
7        "T_inf=1000;Diameter=Dcoal;Lamda=lamdaSolid;Temp=T;EPS=eps;"
8        "Kf=0.026197599;ReyBC=100*2*Diameter/1.35176E-05;Pr=0.744;"
9        "NuBC=(4.31-12.71*EPS+9.81*pow(EPS,2))*(1+0.8*pow(ReyBC,0.6)*Pr);"
10       "alphaBC=NuBC*Kf/Diameter;"
11     );
12     gradientExpression  "-alphaBC*(Temp-T_inf)/Lamda*EPS";
13     value               uniform 300;
14     fractionExpression  "0";
15     }
```

Listing A.4: Shock tests BC: fluid temperature

```
1  boundaryField
2  {
3      aus
4      {
5      type                groovyBC;
6      variables  (
7        "T_inf=1000;Diameter=Dcoal;Lamda=lamdaSolid;Temp=T_Solid;EPS=eps;"
8        "Kf=0.026197599;ReyBC=100*2*Diameter/1.35176E-05;Pr=0.744;"
9        "NuBC=(4.31-12.71*EPS+9.81*pow(EPS,2))*(1+0.8*pow(ReyBC,0.6)*Pr);"
10       "alphaBC=NuBC*Kf/Diameter;"
11     );
12     gradientExpression  "-alphaBC*(Temp-T_inf)/Lamda*(1-EPS)";
13     value               uniform 300;
14     fractionExpression  "0";
```

```
15      }
```

Listing A.5: Shock tests BC: solid temperature

Appendix B

New model

B.1 MultiKineticRateDevolatilization.C

```
{
        bool done = true;
        auto &_vAlSima = const_cast<List<scalar> &>(volatileAlSima_);
        auto &_vAlSimb = const_cast<List<scalar> &>(volatileAlSimb_);
    forAll(volatileData_, i)
    {
        const label id = volatileToGasMap_[i];
        const scalar massVolatile0 = mass0*YVolatile0_[i];
        const scalar massVolatile = mass*YGasEff[id];
        scalar &alSima = _vAlSima[i];
        scalar &alSimb = _vAlSimb[i];

        // Combustion allowed once all volatile components evolved
        done = done && (massVolatile <= residualCoeff_*massVolatile0);

        // Model coefficients
        const scalar Vmax = volatileData_[i].Vmax();
        const scalar alpham1 = volatileData_[i].alpham1();
        const scalar alpham2 = volatileData_[i].alpham2();
        const scalar Ea1 = volatileData_[i].Ea1();
        const scalar Ea2 = volatileData_[i].Ea2();
        const scalar Tb1 = volatileData_[i].Tb1();
        const scalar Tb2 = volatileData_[i].Tb2();
        const scalar Ord1 = volatileData_[i].Ord1();
        const scalar Ord2 = volatileData_[i].Ord2();

        alSimb = alpham1;
```

```
28
29        const scalar rrSima = Ea1*exp(-Tb1/T)*pow(alpham1-alSima,Ord1);
30        const scalar rrSimb = Ea2*exp(-Tb2/T)*pow(1-alSimb,Ord2);
31        alSima = alSima + rrSima*dt;
32        alSimb = alSimb + rrSimb*dt;
33        const scalar rrSim = rrSima + rrSimb;
34
35        // Mass transferred from particle to carrier gas phase
36        dMassDV[id] = min(dt*rrSim*massVolatile, massVolatile);
37    }
```

Listing B.1: Implemented devolatilization model

```
1     MultiKineticRateDevolatilisationCoeffs
2     {
3         volatileData
4         (
5           //gas   alpham1  Ea1 Ea2 Tb1 Tb2 Ord1  Ord2
6            (CO    0.3871  1.1E5 1E3 1.1E4 1.1E4 2 2)
7            (CO2   0.7564  5500  4000  9400  10000 2 3)
8            (CH4   1       6E6 0 1.65E4  1 2 1)
9            (C2H4  1         1.65E5  0 1.3E4 1 2 1)
10        );
11        residualCoeff    0.001;
12    }
```

Listing B.2: Volatile data for MultiKineticRateDevolatilization model

List of Figures

List of Tables

Publications

Parts of this dissertation are already published in the following literature.

- Y. Pan, C. Spijker, and H. Raupenstrauch, Investigations on the effect of particle size on dust dispersion in MIKE 3 apparatus, pp. 654-662, in: Proceedings of 13th International Symposium on Hazards, Prevention, and Mitigation of Industrial Explosions (ISHPMIE), Braunschweig, Germany,27-31 July 2020.

- Y. Pan, C. Spijker, and H. Raupenstrauch, CFD modeling of particle dispersion behavior in the MIKE 3 apparatus, Alexandria engineering journal 61(12)(2022):9305-9313.

- Y. Pan, C. Spijker, and H. Raupenstrauch, Numerical investigations on dust explosion process in MIKE 3 apparatus, pp. 56–64, in: Proceedings of 10th International Seminar on Fire and Explosion Hazards (ISFEH10), Oslo, Norway, 22-27 May 2022.

- Y. Pan, C. Spijker, and H. Raupenstrauch, TGA-FTIR for kinetic and evolved gas analysis of the coal particles in dust deflagration, pp. 95-111, in: Proceedings of 13th International Symposium on Hazards, Prevention, and Mitigation of Industrial Explosions (ISHPMIE 2022), Braunschweig, Germany, 11-15 July 2022.

- Y. Pan, C. Spijker, and H. Raupenstrauch, Investigation on flame propagation and particle decomposition behavior of dust explosion in MIKE 3 apparatus, pp. 86-94, in: Proceedings of 14th International Symposium on Hazards, Prevention, and Mitigation of Industrial Explosions (ISHPMIE 2022), Braunschweig, Germany,11-15 July 2022.

- Y. Pan, C. Spijker, and H. Raupenstrauch, TGA-FTIR for kinetic and evolved gas analysis of the coal particles in dust deflagration, Applied Thermal Engineering, 2022 (under review).